EXPERIMENTAL CHARACTERIZATION AND PROCESSING OF ADDITIVELY MANUFACTURED Ti-6Al-4V

by
Matthew Oliver Vaughn

A dissertation submitted to Johns Hopkins University in conformity with the requirements for the degree of Doctor of Philosophy

Baltimore, Maryland
October 2021

Abstract

Unencumbered by the limitations of traditional subtractive manufacturing, additive manufacturing (AM) has opened a whole new world of possibilities in complex part geometries that can be produced quickly. Design tools, such as topology optimization (TO), can fully utilize this newfound design freedom, but they require process accurate material properties that are often anisotropic and inhomogeneous. The motivation and goal of this study was the characterization and measurement of mechanical properties of laser powder bed fusion (LPBF) Ti-6Al-4V to inform TO methods for the design of lightweight structures.

A LPBF build consisting of cylinders in multiple build orientations was designed and executed to produce a total of nearly 100 tension, compression, and shear mechanical test specimens. The experiments from these samples were used to form a robust description of the stiffness and yield surface associated with the printed material. There was no notable anisotropy measured with elastic moduli in the build direction 113±6 GPa as compared to in the build plane 116±7 GPa. A tension-compression asymmetry in the yield strength was measured to have a disparity of 892±15 MPa to 996±32 MPa, and this behavior was captured in an asymmetric yield criterion.

The simple to machine compact forced simple-shear specimen geometry was investigated to provide measures of shear elastic and yielding properties. Through an investigation of wrought Ti-6Al-4V conducted with DIC and finite element simulations, it was determined that the shear geometry has an inhomogeneous yielding behavior that causes the stress-strain response to diverge from linear well before reaching the macroscopic yield strength. This led to an undervaluation of the strength when a traditional 0.2% strain offset was employed, it was determined that a strain offset of 2.8% was needed to accurately determine the macroscopic yield point. Using this new

metric for measuring yield, the AM shear yield strengths were evaluated to be 560$\pm$30 MPa, which agreed well with the yield surface that contained the tension and compression results.

Metal AM processes, such as LPBF, are prone to microstructures that contain defects and non-equilibrium phases that can be deleterious and are typically mitigated via post-processing. Hot isostatic pressing is the industry standard, but this requires specialized chambers and can be costly. Alternatively, thermo-hydrogen refinement of microstructure (THRM) has recently been introduced as a technique that uses hydrogen as a temporary alloying element to enable a novel phase transformation that offers recrystallization and homogenization of as-built Ti alloys into an ultra-fine microstructure. A study of the temperature used in the THRM process was conducted and showed significant gains in ductility over the as-built condition. The THRM temperatures investigated all exhibited tensile properties comparable to those achieved using HIP. Heating over the β transus temperature, resulted in a significant growth of the prior β grains resulted. This increase in grain size, coupled with the formation of a continuous layer of α phase along the boundaries, was found to present a preferable path for crack growth, leading to a reduction in ductility at higher temperatures (15% for 850 C and 11% for 1200 C).

Taken as a whole the work was successful in generating a description of the full elastic and yielding behavior to inform TO models to enable the design of lightweight lattice structures. Additionally the THRM process was demonstrated to be an effective and cost efficient replacement for traditional post-processing of LPBF Ti-6Al-4V.

Advisor: Professor Kevin J. Hemker

Readers: Professor Kevin J. Hemker, Professor James Guest, Dr. Brandon McWilliams, Dr. Matthew Dunstan

Acknowledgements

I cannot express just how crucial the support of my colleagues, friends, and family was in the completion of this dissertation. Between what seemed like an eternity dealing with complications from my knee injury, a global pandemic throwing a wrench into the last year of my research, and the inevitable difficulties common to every PhD researcher’s progression, it is not an exaggeration to say I would not have been able to do this without you all. Firstly, I would like to extend my gratitude to my advisor, Professor Kevin Hemker, for giving me the opportunity to join the group in 2016 and supporting me through all the ups and downs in this project. Throughout the past five years he has provided excellent guidance and support not just in the scientific aspect of research, but also in professional development and communication.

I want to thank all the professors in the Departments of Mechanical Engineering and Materials Science and Engineering for expanding my knowledge of the two disciplines and always being accessible even beyond the classroom. I am grateful to my thesis committee, Professor James Guest and Dr. Brandon McWilliams for all their valuable input to this work over the years. I would like to express my gratitude to Professor Guest and the rest of his group, especially Justin Unger, for their constant collaboration. Even beyond the useful guidance I received regarding mechanics and their topology optimization methods, interacting with them was always a pleasure. I want to thank Dr. Brandon McWilliams and Dr. Andrew Gaynor for providing me the opportunity to access the resources at the Army Research Laboratory, gaining hands on experience with the printing process. I would like to extend additional gratitude to Dr. Matthew Dunstan at ARL for incorporating me into his promising heat treatments research and expanding my knowledge of titanium metallurgy.

Over the past five years, I have had the immense privilege of working with amazing fellow members of the Hemker research group, both past and present. From the ever-gracious postdoctoral fellows (Professor Kelvin Xie, Professor Gi-dong Sim, Dr. Ankur Chauhan) to the many graduate students (Dr. Paul Rottmann, Dr. Brady Butler, Dr. David Eastman, Dr. Gianna Valentino, Dr. Luoning Ma, Dr. Betsy Congdon, Jalil Alidoost, Arunima Banerjee, Ojaswi Agarwal, Sam Present, Kate Brizzolara, Catherine Barrie, Mike Patullo, Sharon Park) I am so grateful for your assistance and support over the years. To all the senior students, especially Gianna, David, and Luoning, I am extremely appreciative of your guidance and perspective in navigating PhD life in the lab. Each of my fellow lab mates were invaluable in their own way, providing feedback on research and how I presented it. Whether it was talking (definitely only about research) in the lab, Hemker Happy Hours, or commiserating when things just weren't quite working out, I am grateful to the support system that we have cultivated within the group.

It was a pleasure to have the opportunity to interact with and learn from so many other researchers in my time at Hopkins especially the members of the Guest, Ramesh, Nguyen, and Ghosh groups. Beyond research and the classroom, I'm glad to have had the opportunity to participate in the Mechanical Engineering Graduate Association and socialize with such a diverse group of intelligent individuals. I am especially grateful to those that have grown to call good friends. All the nights of hotpot, barbeques, and cards against humanity (Gianna, Debjoy Mallick, Amy Dagro, Tracy Ling, Harsh, Anu Kaushik, Andrew Spielvogel, Jess Keene); various sports leagues, taco Tuesday and visits to Ottobar (Debjoy, George Weber, Mattias Almansi, Mohammed Mohammed, Max Pinz, Deniz Ozturk); great friends to relax with outside of the lab meant so much.

Even with the distance and limited opportunities to see them, I cannot forget all my lifelong friends back in Arizona who continued to support me from afar. It is no exaggeration to say I consider you all my large extended family from my first friend I made when moving to the state in fourth grade (Kayleigh Durigg) to those I made in undergrad (Truc Nguyen and Shelby Heinrich). Every year I would look forward to the fall and a chance to fly home to attend an ASU football game with my fellow Sun Devil diehards (Dan and Emily Votroubek, Brandon and Lisa Butterfield, Miggy Eusebio). I'm so happy I was able to celebrate your weddings with you (Mat and Sam Lewis, the Butterfields). I look forward to eventually being able to celebrate with those who the pandemic got in the way (Shane and Peyton Gill, the Votroubeks) and those who are newly engaged (Alec Laws and Emily Prévost). It was an absolute blast taking a break to wander Europe with you for a couple weeks (Alec, Emily, Ryan Uchimura, Joe Becker). We are definitely well past due a trip to go hiking and rock climbing (Ian McFate, Alec, Emily P.). While being forced to only interact through a screen for the past two years, I cannot wait to see everyone and resume real life shenanigans (Matt Tomasson, Kyle Gallas, Logan Villa, Troy Mullaney, Jake Stoll, Brandon Low).

Finally, I dedicate my thesis to my complicated large family, I would not be who I am or where I am without their love and support whether they be related by blood, law, or just de facto. To my parents David and Monica, I am thankful for the support and the confidence you always had in my ability to succeed. To my mother, Anne, as much as your out of the blue hour-long phone calls to tell me a seemingly never-ending story may not be my definition of fun, I appreciate the thought, nonetheless. My sisters Cristy, Michelle, Arrow, and Elizabeth have always been my biggest cheerleaders, whether it be them screaming the loudest on the sidelines at my lacrosse games or celebrating my academic success. I of course can't leave out my niece and nephew, Lalena and

Jayce, even though they're always too embarrassed to talk to me over video chat. My brother Dan, my sister-in-law Crystal, and my nephew and niece, Zach and Emily, I am so thankful for everything you've done for me and am glad I was able to spend so much quality time with you while living back on the same coast. My brother-in-law, Giovanni, thank you for getting my first lab position way back in my freshmen year that was the first step to get to where I am now. I would be remiss if I did not give appreciationg to the entire Esteves and Urquiza families, you have always made me feel part of your families. Last but certainly not least, my girlfriend Morgan, I can't thank you enough for all your support and putting up with me through all my struggles. You and our sassy dog, Nugget, have helped me keep my head on straight when everything seemed like too much to handle.

CONTENTS

List of Tables

List of Figures

CHAPTER 1: INTRODUCTION AND BACKGROUND

1.1. Motivation

Additive manufacturing (AM) technologies have been in development since the 1970's, with the introduction of the first polymer stereolithography printer in the late 1980's and metal laser sintering following soon after in the early 1990's [1, 2]. These technologies became commercially viable in the last decade and have since drawn immense interest from industry and scientific research communities [3, 4]. Unencumbered by the limitations of traditional subtractive manufacturing, such as mills, lathes, or CNC, AM has opened a whole new world of possibilities in complex part geometries. The layer-by-layer approach taken by AM technologies enable the production of parts with complex features and organic shapes that would be costly, if possible, to manufacture through subtractive means. Subtractive methods can only produce features that their cutting tools can reach, making complex geometries such as lattices or internal voids nearly impossible to create. Casting can produce reasonably complex geometries; however, development and production of molds can be a lengthy and expensive process. Meanwhile, AM can build many intricate geometries quickly with just a 3D computer model.

It is still relatively expensive to use metal AM technologies to produce serviceable parts - though these costs are being reduced all the time with advancements in quality and availability of the technologies. Metal AM is generally best used for smaller complex high value parts: one of the most notable mass-produced metal AM parts in recent years is GE's LEAP engine fuel injector. Originally manufactured by brazing 20 individual components, it is now a single part produced in one machine over a few hours and is more reliable in application [5]. The ability to change printed geometries between individual parts along with the enhanced design capabilities is rapidly making additive the future of manufacturing bioimplants [6]. Examples of metal parts manufactured using additive manufacturing are shown in Figure 1.1.

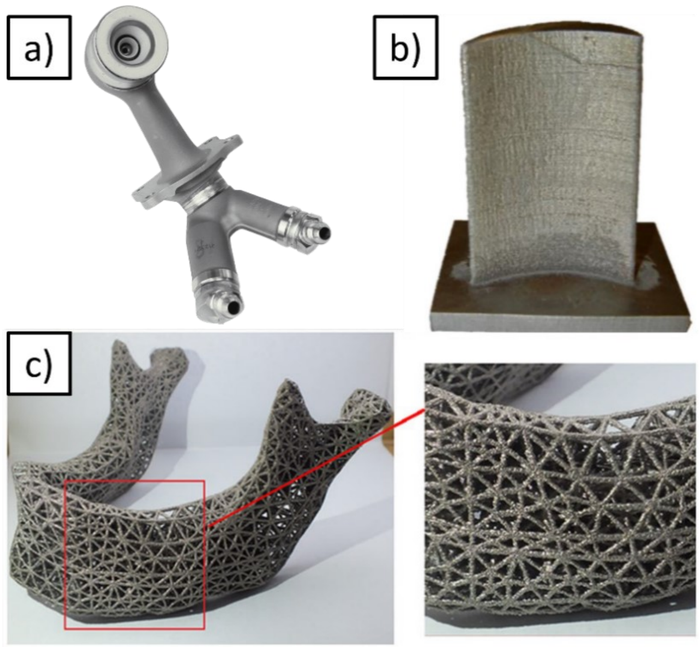

Figure 1.1: Examples of additively manufactured metal parts: (a) GE LEAP engine fuel nozzle produced using SLM [5] (b) Ti-6Al-4V turbine blade repaired using LMD [7] (c) Ti-6Al-4V 3D mesh mandibular prosthesis scaffold fabricated using EBM [6].

1.1.1. Designing for Additive Manufacturing

The enhanced geometric capabilities of AM that enable the production of parts with lattices or internal channels has allowed for a fuller utilization of computer aided design tools, such as topology optimization (TO) [8]. TO is a design tool that solves a material distribution problem from applied loading conditions within a design domain, optimizing for prescribed metrics such as stiffness or weight reduction [9, 10]. An example beam light-weighting design problem is demonstrated in Figure 1.2. In conventional design it is safe to remove material from the center of the beam as it is understood that it does not carry as much of the load. Through an iterative process the topology can be optimized to retain material only where necessary to support critical load paths resulting in geometries that far surpass performance that can be generated from human intuition.

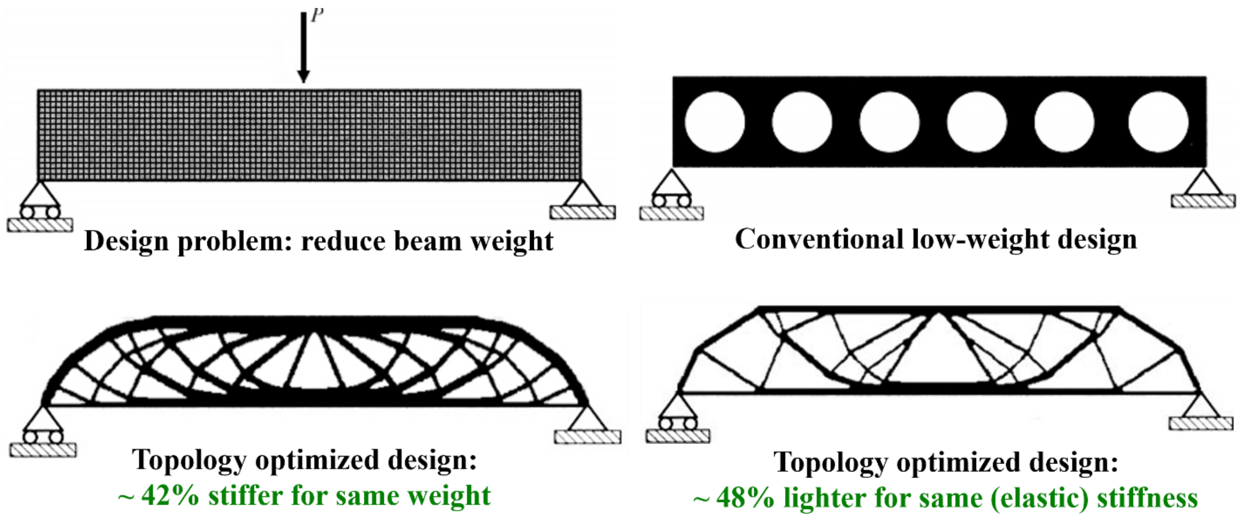

Figure 1.2: Example beam design problem demonstrated capabilities of topology optimization to produce geometries that more efficiently utilize material than conventional designs.

If not constrained for the limitations of the fabrication process these optimizations codes often suggest organic shapes that are difficult or impossible to create with traditional manufacturing methods. In addition to lightweight and stiff components, the combination of TO and AM can be leveraged to produce compliant mechanisms, energy absorption, and other novel mechanical responses seen in metamaterials [11, 12]. These highly desirable capabilities are not free from considerations that need to be accounted for. As will be discussed in the following sections, the properties of AM materials are processing dependent and differ greatly from conventionally produced materials, leading to a need to adapt conventional design practices for AM applications [13, 14].

While additive methods do present vast opportunities in producible geometries, there are considerations that need to be made in applying design tools: support structures, porosity, anisotropy, print variabilities, and the effects of post-processing [15]. For these design methods to accurately predict performance they must be provided an accurate description of the material properties and geometric capabilities of the AM technology utilized. Adaption of TO models to allow for overhanging features without requiring additional support material that would have to be removed in post-machining have been demonstrated by Gaynor and Guest [16]. Methods of accounting for uncertainties in resultant properties to enable robust designs have been developed as well [17]. As the design methods improve, experimental data will be required to inform these models for each specific material, printing method, machine, and process condition. Since there are a multitude of variables within each of these aspects, there is a need for efficient data collection. This dissertation describes efforts to characterize additively manufactured materials in a manner that can be utilized in improvement of TO designs.

1.2. Background

1.2.1. Metal Additive Manufacturing Technologies

There are a wide variety of metal AM technologies, with as many acronyms as there are companies, as demonstrated in Figure 1.3. They are generally categorized by how the material is applied and the energy source used to locally melt or sinter the material. One primary type is Directed Energy Deposition (DED), where the material is applied at a point either in powder or wire form and moves in tandem with the energy source. Another primary category is Powder Bed Fusion (PBF) where a layer of powder of a particular material is laid down and the energy source rasters across the layers to form a part. Both can use powder material with laser and electron beam energy sources. DED can also use wire feedstock, arc melting, and produce functionally graded alloys through multiple feedstock sources [18]. DED, originally adapted from automated welding technology, can be operated like a CNC where material can be added anywhere on a part in 3D space that the tool head is able to access. With the ability to work in tandem with subtractive methods DED is well suited for repairing existing components. DED is also capable of depositing large volumes of material, with larger gage wire-fed machines, for production of large components. This contrasts with PBF that builds up in parallel layers of powder which has better spatial resolution than DED, especially in the laser-based machines. PBF is used more for initial production of small to medium scale parts especially where dimensional accuracy and surface quality is critical [19]. This dissertation will focus on the laser powder bed fusion (LPBF) process, though processing kinetics are similar in the metal AM processes as most incorporate rapid directional solidification.

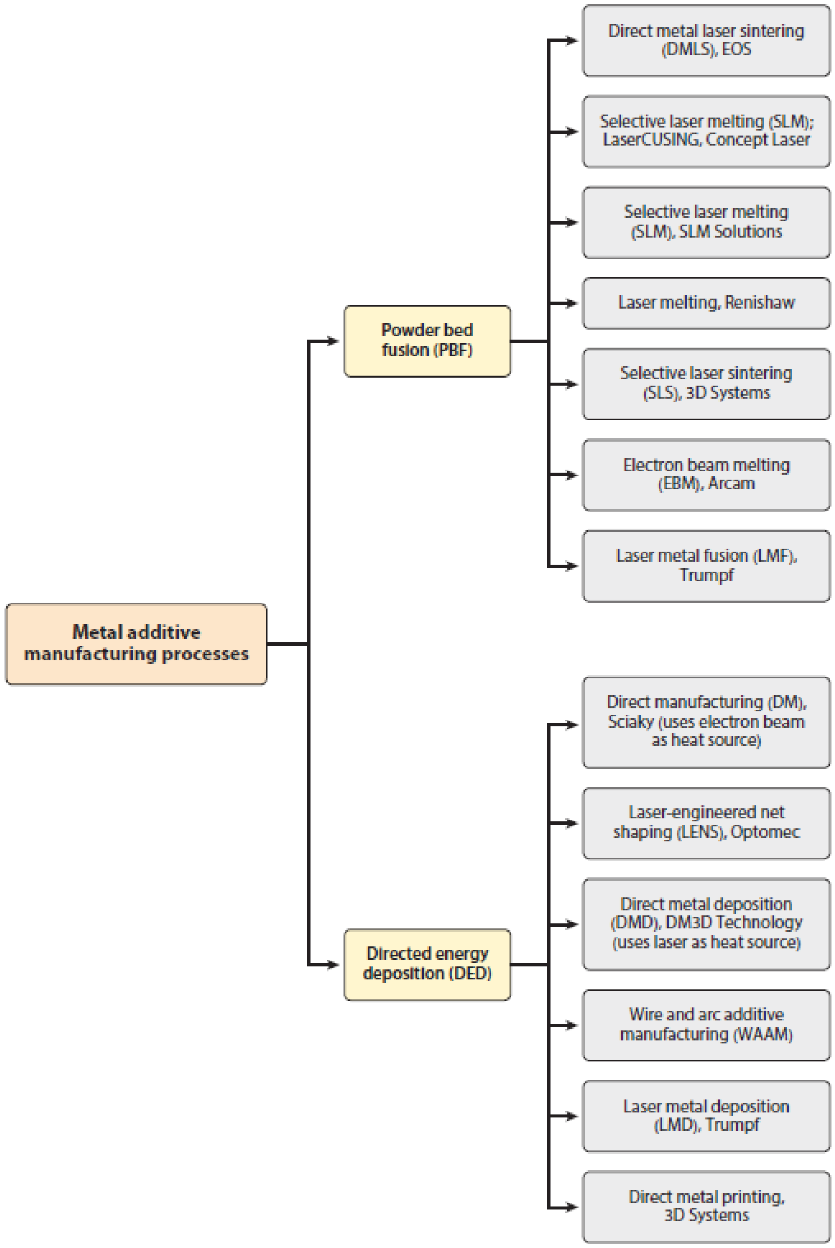

Figure 1.3: Examples of commercial metal additive manufacturing technologies and how they are categorized. Trade marking of process names has led to a plethora of names for similar processes [20].

Laser Powder Bed Fusion (LPBF) consists of a build plate that is covered with a thin layer of powder either by a scraper or roller, and a laser that rasters across the layer in prescribed patterns. The laser melts the powder, which rapidly solidifies after the laser passes [21]. The laser rapidly outlines and fills in areas prescribed to be solid. Once a layer is completed the build plate is then lowered by one layer height and the process repeats until the entire part is produced, this process is illustrated schematically in Figure 1.4. Laser based methods operate within an inert gas environment to prevent oxidation; electron beam systems necessitate a vacuum to enable transmission of the beam.

Electron beam melting (EBM) also involves successive layers of powder but utilizes larger powder sizes (45-100 μm) as compared to laser techniques (15-45 μm). EBM has an enhanced ability to control build temperatures and quench rates thanks to better energy absorption, higher power output capabilities, the vacuum atmosphere, and faster raster velocities than a laser system due to not relying on mechanical steering mirrors. This is useful in controlling the thermal history and therefore the final structure, though EBM produces an inferior surface quality, and there is additional cost associated with the more expensive energy source and the vacuum system needed to operate. Both powder bed techniques are capable of being implemented with heating of the build plate and chamber to assist in controlling the temperature of the build. As the powder does not conduct heat effectively, the primary path for heat conduction away from the part is through the underlying support material and into the build plate. The effectiveness of this is heavily dependent on part geometry and the effective thermal conductive path, which can be an issue for overhanging features [22].

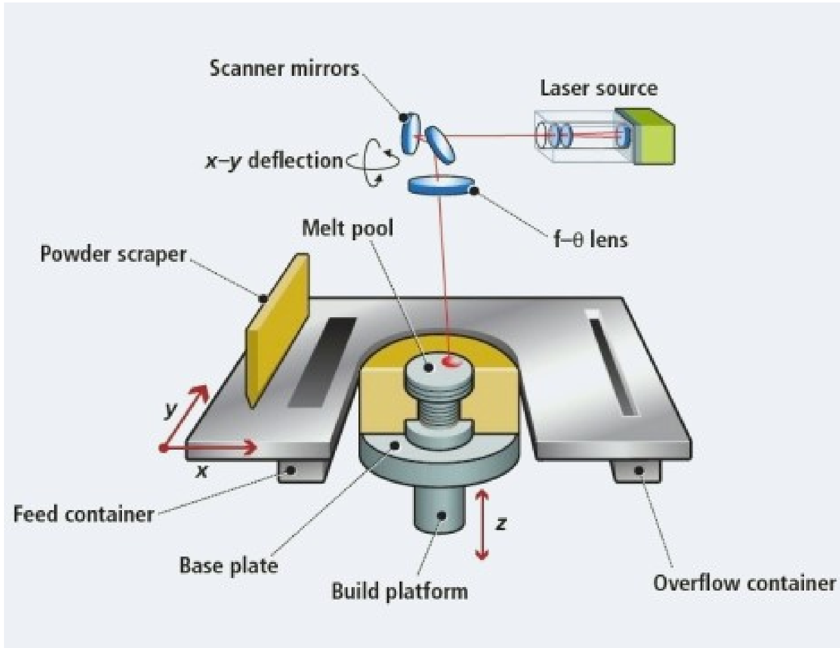

Figure 1.4: Diagram of laser powder bed fusion process [23].

1.2.2. The Physics of LPBF Printing and Defect Formation

Melting and solidification during the printing process is a complex interaction of physical phenomenon as illustrated in Figure 1.5(a). While processing and resultant properties are in general alloy dependent, all additive processes are prone to anisotropic inhomogeneous microstructures, and attendant properties, that result due to high thermal gradients from localized heat input, directional solidification, and variations in thermal histories within a build [24-26]. Localized cyclic heating leads to the development of high residual stresses from the contraction of molten material as it solidifies. The high thermal gradients in the solid material also contribute to residual stress from localized expansion and contraction, and thermal exposure leads to reduced yield strength, causing plastic compressive strains due to surrounding constraints. When the heat source is removed, the top layers cool and the thermal strain contracts, producing a final residual tensile stress on the top as illustrated in Figure 1.5(b). This stress can cause geometries to be out of tolerance, negatively affect performance, and in extreme cases cause a part to pull away from the build plate [27, 28].

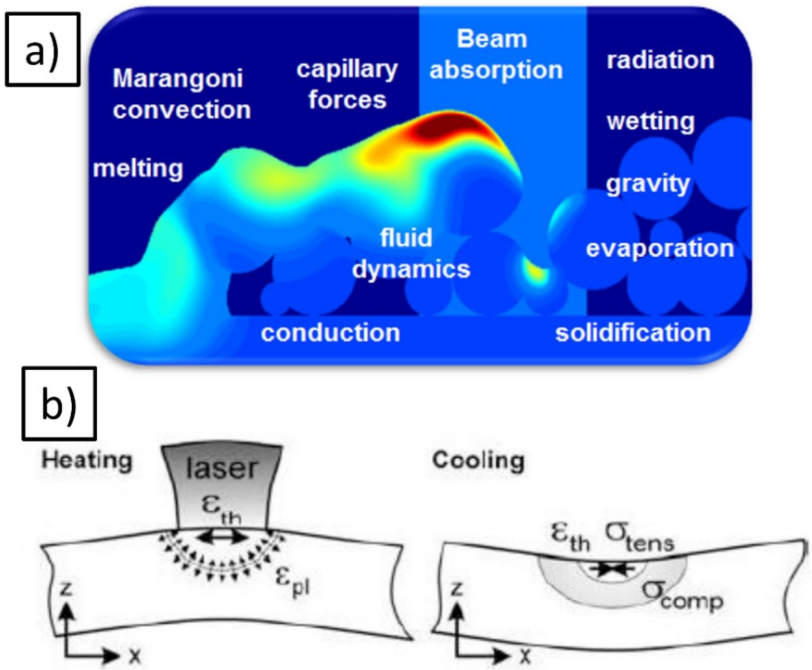

Figure 1.5: (a) Diagram of melting dynamics in PBF processes with relevant physical effects [29]. (b) Development of residual stress from thermal gradient mechanism in the printing process [28].

1.2.2.1. Laser Print Parameters

PBF techniques have been shown to be prone to the formation of porosity in the form of lack of fusion (LOF) from inadequate melting of the feedstock between layers or rasters , or keyholing from excessive heating causing a turbulent melt pool that traps gases, see Figure 1.6 [30]. This porosity, along with printed surface roughness, can be especially detrimental to fatigue and fracture properties [31]. Printing challenges can be mitigated through the optimization of print parameters for the materials used and the part geometries being produced [32-34].

Print parameters are often compared through a baseline metric of absorbed energy density (J/m^3):

$$E = \frac{\alpha P}{vht} \tag{1.1}$$

where P is power (J/s), v is scan speed (m/s), h is the hatch spacing (m), t is layer thickness (m), and α is the absorptivity. This value gives an understanding of the energy available for the phase transformations in the process but does not give a complete picture of the kinetics taking place [35]. A much more robust method for understanding the kinetics of the print process is to consider how much power is input versus how quickly the laser passes over a location, as illustrated in Figure 1.6(a). Zone I correlates to fully dense material, Zone II to keyholing, Zone III to LOF, and OH to an overheating case that causes build failure [30]. The limitations of the energy density metric can be seen in Figure 1.6(a) with a constant energy density that transitions between Zone III to Zone I. Efforts have been made through simulations of the print process to expedite optimization studies and give insight to the mechanisms active during the print that cause defect formation and evolution of microstructures [36-38].

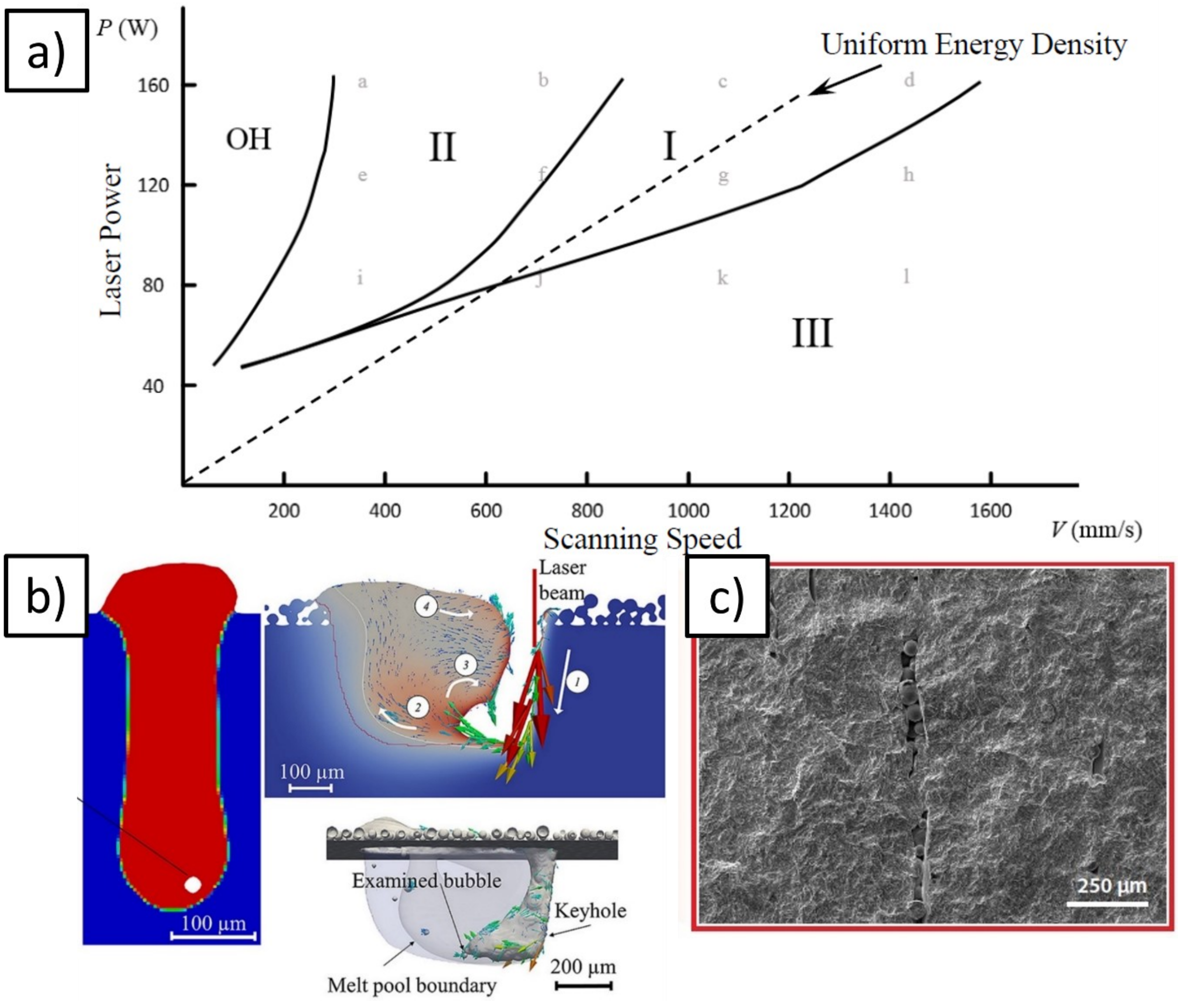

Figure 1.6: (a) Processing parameters of laser power and scan speed with measured experimental density values for LPBF Ti-6Al-4V with generalized regions correlating to I: fully dense material, II: keyhole formation with high power and slow speed, III: lack of fusion between layers with inadequate melting power. Adapted from [32]. (b) Simulation of melt pool dynamics showing keyhole formation [30]. (c) Example of unmelted powder and lack of fusion defect between layers [20]

In addition to the laser power, the raster scan strategy for filling in the layers of a part has been studied extensively with examples illustrated in Figure 1.7 [39, 40]. Local variations in time between rasters, both in the same and subsequent layers, can lead to large differences in local thermal histories that can result in inhomogeneities in microstructure and defect content [41, 42]. The direction of rasters influences the gradient of solidification and formation of microstructures. In the extreme case where the same raster direction is repeated in subsequent layers, this can lead to a tilting of the columnar grain structure [37]. Predictive models and in-situ processing monitoring have been implemented to better understand thermal histories and their correlation to microstructural texture and defects [43-45].

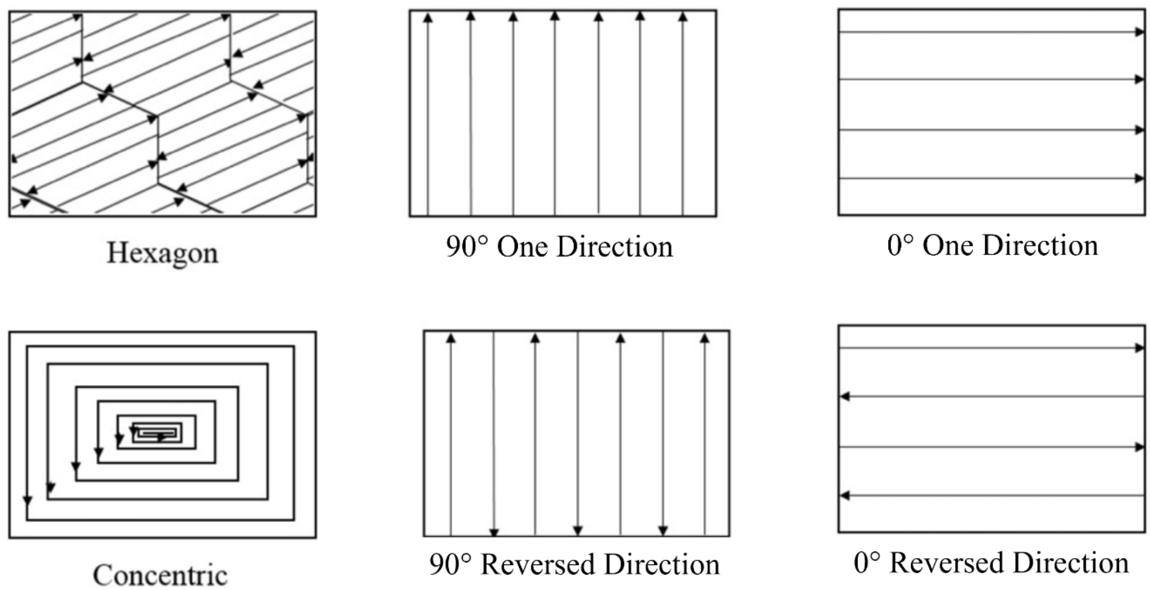

Figure 1.7: Typical infill scan strategies implemented in PBF printing: scans in the same and reversed directions both with the option to alternate orientations like 0° and 90°. Hexagon scans back in forth in hexagons that subdivide a layer while concentric starts on the outside of the geometry and spirals inwards. Adapted from [42].

1.2.2.2. Post-print Treatments

In application, parts often undergo post-print heat treatments to mitigate remaining deleterious features like residual stress, porosity, and undesirable microstructures. These heat treatments commonly include an initial heating step (while still on the build plate) to relieve residual stresses and a subsequent hot isostatic pressing (HIP). Originally developed for use in powder metallurgy, HIP consists of heating parts to an elevated temperature while subjecting them to a high positive pressure with inert gas. The high temperatures reduce the flow stress of the material while the applied pressure facilitates pore closure through a combination of plastic yielding, creep, and diffusional densification [46-48]. Figure 1.8(a) demonstrates the capability of HIP to close a 2 mm diameter internal pore of unmelted powder. It is also known that HIP is not effective in pores open to the surface as HIP is reliant upon enclosed pores for the applied pressure to enable closure. Additionally the HIP process may lead to a slight degradation in geometric accuracy as can be seen in the surface deviations in Figure 1.8(b) [49].

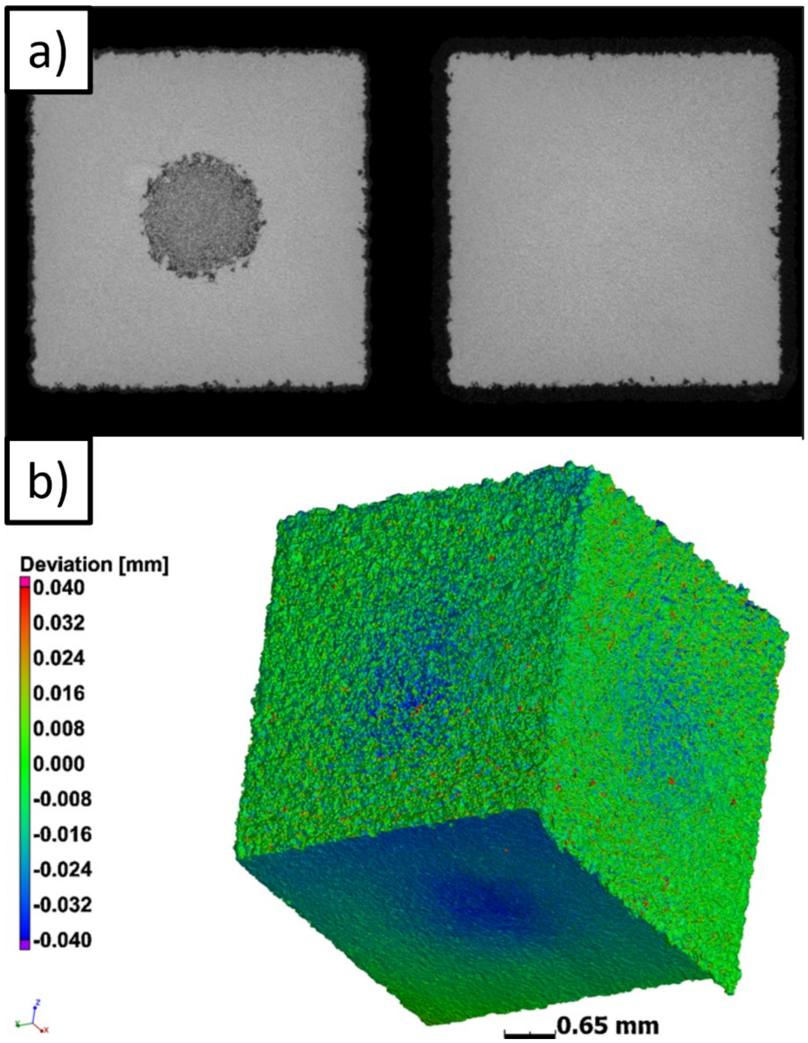

Figure 1.8: (a) 5 mm cube with 2 mm diameter cavity of unmelted powder before and after HIP, pores open to the surface retained after HIP can be seen. (B) Shrinkage of cube after HIP. Adapted from [49].

Depending on the application, parts may undergo additional machining or surface treatments. Subtractive machining is often implemented to ensure critical dimension tolerances or prevent fatigue failure in components affected by surface roughness and thermal warping. Other surface treatments, such as shot or laser shock peening, can improve fatigue performance by improving surface quality and inducing a compressive stress state on the surface [50]. Interestingly, as-printed surface roughness and underlying porosity that is generally undesired in engineering applications has actually been shown to dramatically improve bone integration with surgical implants [51].

1.2.3. Additive Manufacturing of Ti-6Al-4V

The titanium alloy Ti-6Al-4V is commonly used in AM applications due to its light weight, high strength, good weldability, corrosion resistance, biocompatibility, and cost savings associated with the efficient use of material in AM [52, 53]. The alloy does have poor thermal conductivity, which is known to cause complications when machining parts and also has implications on the printing process because it induces high thermal gradients. Ti-6Al-4V accounts for over 50% of all titanium usage, mostly in the medical and aerospace industries, making it a well understood system in conventional forged and cast forms. Ti-6Al-4V is a two-phase alloy consisting primarily of an HCP α phase and a small amount of BCC β. Microstructures are most commonly lamellar, though equiaxed and bimodal structures are possible. The mechanical properties are strongly dependent on the microstructures formed with these two phases, understanding how these phases form through the printing process is critical for predicting performance in application.

1.2.3.1. Solidification of Phases

In LPBF, the laser passes over an area creating a molten pool that quickly solidifies into the BCC β phase, preferentially with <001> texture along the maximum thermal gradient. Assuming a sufficiently rotated scan strategy, the average thermal gradient in solidification is nominally in the build direction. This process has been simulated in multiple works as well as observed in printed materials [36, 37]. The melting of subsequent layers often causes growth of very long columnar β grains that exhibit a fiber texture along the build direction as shown in Figure 1.9(a).

The transition between columnar and equiaxed β grain solidification is dependent on the temperature gradient and solidification speed, the same as it is in castings [54]. Equiaxed grains form with a lower thermal gradient in the melt pool and faster solidification speed, and a 1 kW laser (more powerful than commercial systems) has been demonstrated to enable production of equiaxed β grains in AM by reducing the gradient [55]. Relatedly the material melted on the exterior surface of a part will often exhibit finer grains as the unmelted powder provides preferential inhomogeneous nucleation sites instead of extending preexisting columnar grains, see Figure 1.9(b) [56].

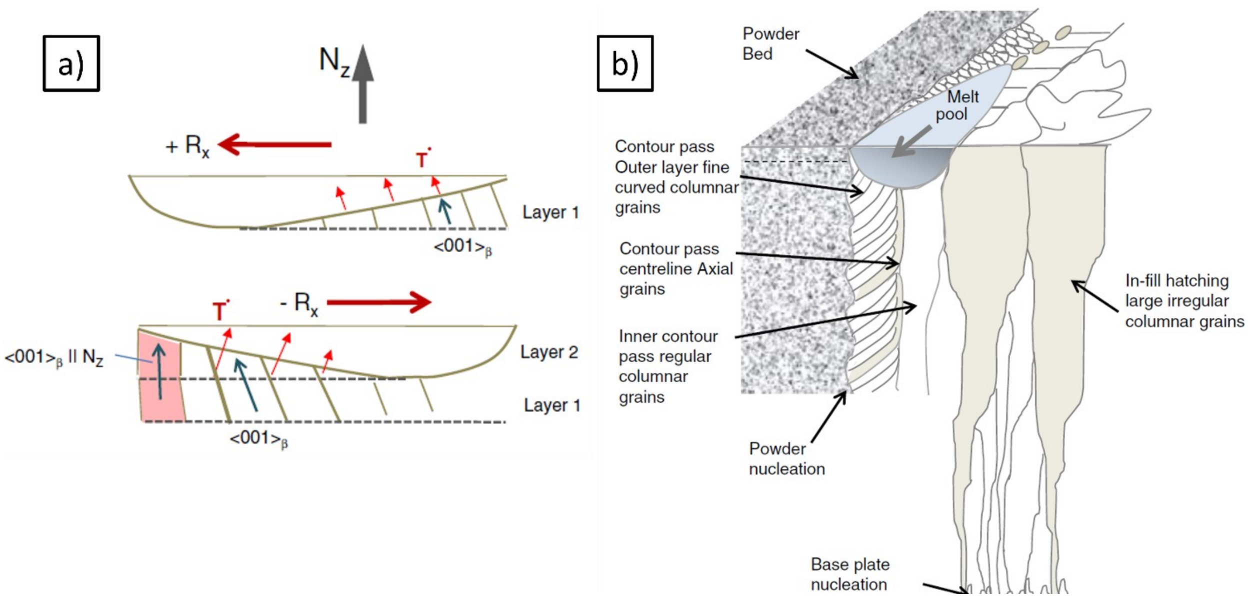

Figure 1.9: (a) Solidification behavior of β grains as 2 subsequent layers are melted in opposite raster directions results in an average <001> direction along the maximum thermal gradient. (b) Solidification of columnar grains in the interior of part with finer grains nucleated from powder on skin from the initial outline of the part in powder bed process [56].

When the material cools to approximately 980 °C, α laths begin to nucleate. This occurs preferentially at the boundaries of the prior β grains, and then as lathes within the β grains, ultimately leaving only a small amount of β in the final microstructure. The orientation of the α laths in Ti-6Al-4V form according to a specific Burgers relation, with the (0001) basal plane of α coplanar to a (110) plane of β and one of the $[11\bar{2}0]_\alpha$ <a> crystallographic direction parallel to a

$[111]_\beta$ direction and the α/β phase boundary [57]. The formation of 12 possible α variants that have this relation within the prior β grain diminishes the anisotropic nature of the texture, as evidenced by the fact that modulus measurements are close to isotropic in the literature [58]. The strength and fracture behavior of the $\alpha+\beta$ microstructure is more strongly influenced by the columnar structure of the prior β grains when the loading direction is oriented along or perpendicular to the grain boundaries. This effect is more pronounced with thick regions of α at the prior β grain boundaries, as loading perpendicular to that boundary produces a weak Mode I state across the continuous layer illustrated in Figure 1.10 [59, 60].

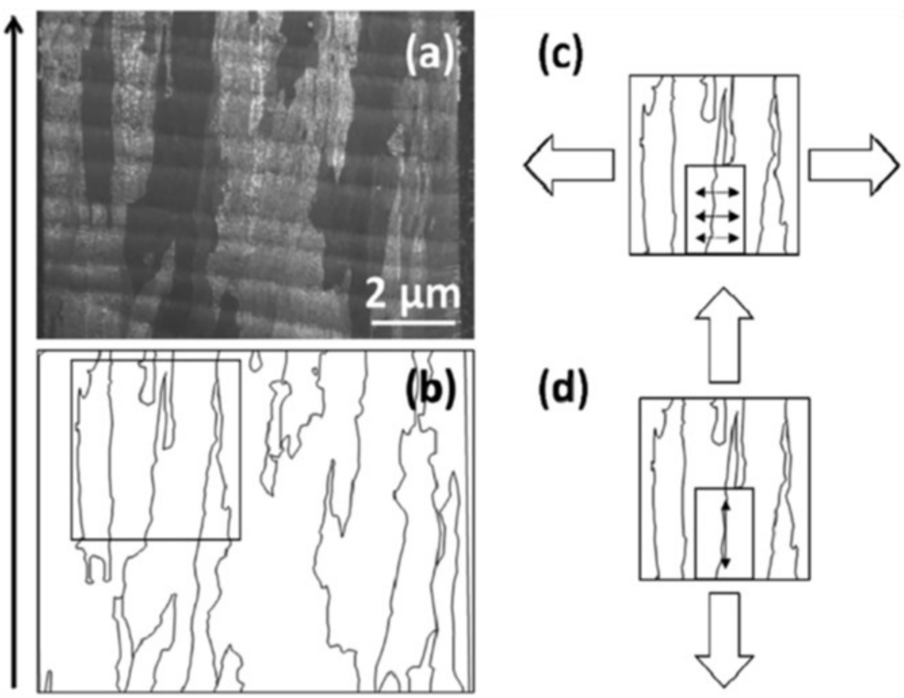

Figure 1.10: (a) Micrograph of as-built columnar prior β grains with (b) outlined grain boundaries (c) loaded perpendicular (Mode I) and (d) parallel to the grain boundary [59].

1.2.3.2. Cooling Rate Sensitivity in Phase Transitions

The Ti-6Al-4V pseudo-binary phase diagram and the time-temperature-transformation diagram of cooling from the β region is shown in Figure 1.11. At slow to intermediate cooling rates (< 20 °C/s), the α laths preferentially form in colonies of parallel laths of the same orientation. A slower cooling rate will lead to a thicker α layer at the prior β grain boundary as well as larger α colonies and laths. As the cooling rate increases, the laths are not able to grow sufficiently fast causing new laths and colonies to nucleate perpendicular to existing laths, thus refining the microstructure. At high enough rates this will result in a lack of colonies and the formation of a structure often referred to as a basket-weave or Widmanstätten. This has implications on the yielding behavior of the material as dislocations are more readily transmitted through colonies with a low energy barrier from the small change in Burgers vector across the lath boundaries, which is increased when they do not share orientations [61].

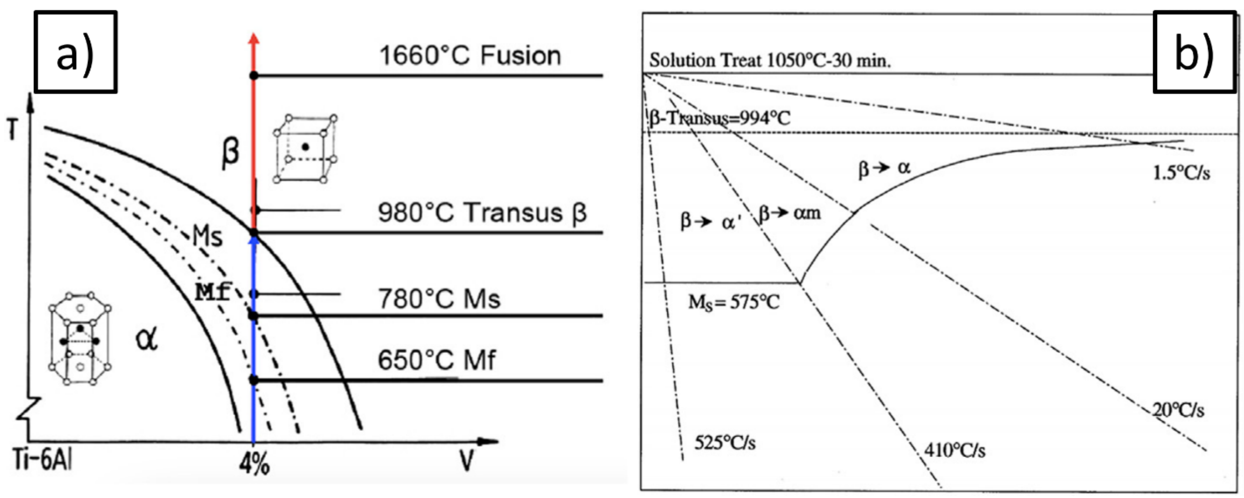

Figure 1.11: (a) Pseudo binary phase diagram of Ti-6Al and V. (b) Time-temperature-transformation diagram of phases in Ti-6Al-4V where martensite α' forms at high quench rates and HCP α forms at lower rates [62].

A sufficiently fast cooling rate (>410 °C/s) will cause the formation of a martensitic hexagonal phase α'. This phase is formed at high quench rates because the formation of α requires diffusional segregation of α and β stabilizers, Al and V respectively, that requires time and temperature. By contrast the martensitic phase forms through a diffusionless process involving the shearing of the β BCC lattice into an elongated hexagonal lattice [57]. Martensite is strong but very brittle and often found in as-printed material unless the build temperature is controlled or if subsequent print layers cause sufficient reheating for in-situ decomposition to α as illustrated in Figure 1.12 [63]. This in-situ heat treatment of underlying layers contributing to inhomogeneities in microstructure and resultant properties must be considered in the print and post-processing of parts.

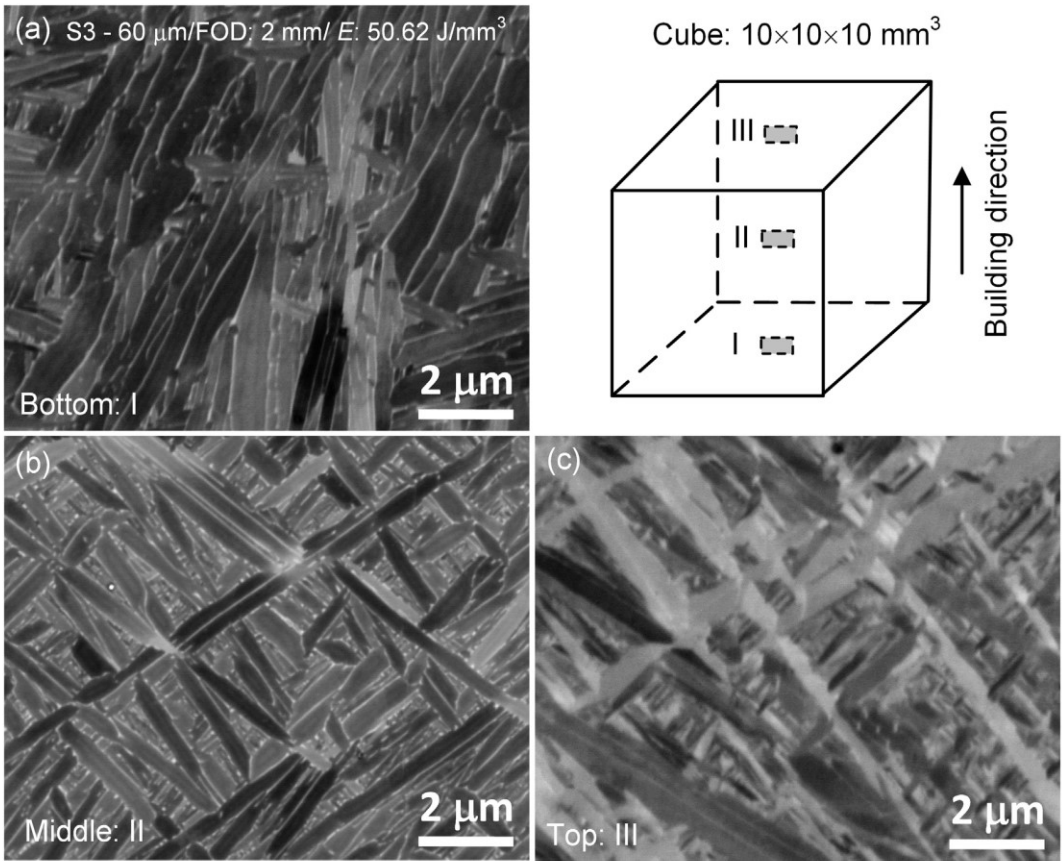

Figure 1.12: Microstructure (BSE) variations along build direction in SLM Ti-6Al-4V with 60 μm layer thickness. (a) Region I, bottom: fine lamellar structure with presence of parallel lathes consistent with colony formation; (b) Region II, middle: ultra-fine basket-weave Widmanstätten structure; (c) Region III, last deposited layers: needle-like martensitic structure [63].

LPBF processes like direct metal laser sintering (DMLS) are especially prone to the formation of martensite due to the reduced build temperature control as compared to EBM, as evident in the strong but brittle as-built DMLS properties shown in Figure 1.13. A final aging heat treatment is common to all forms of Ti-6Al-4V to facilitate precipitation strengthening through the formation of Ti_3Al, which has a solvus temperature of 550 °C [64]. With post-processing (DMLS, HIP + HT in Figure 1.13) porosity is reduced and the martensite can decompose into α and allow for growth of lamellae producing a reduction in strength but an increase in ductility approaching properties comparable to cast or wrought materials. While HIP is an effective treatment for improving properties, it requires costly specialized equipment leading to an opportunity to replace it with a more accessible and cost-effective post-process.

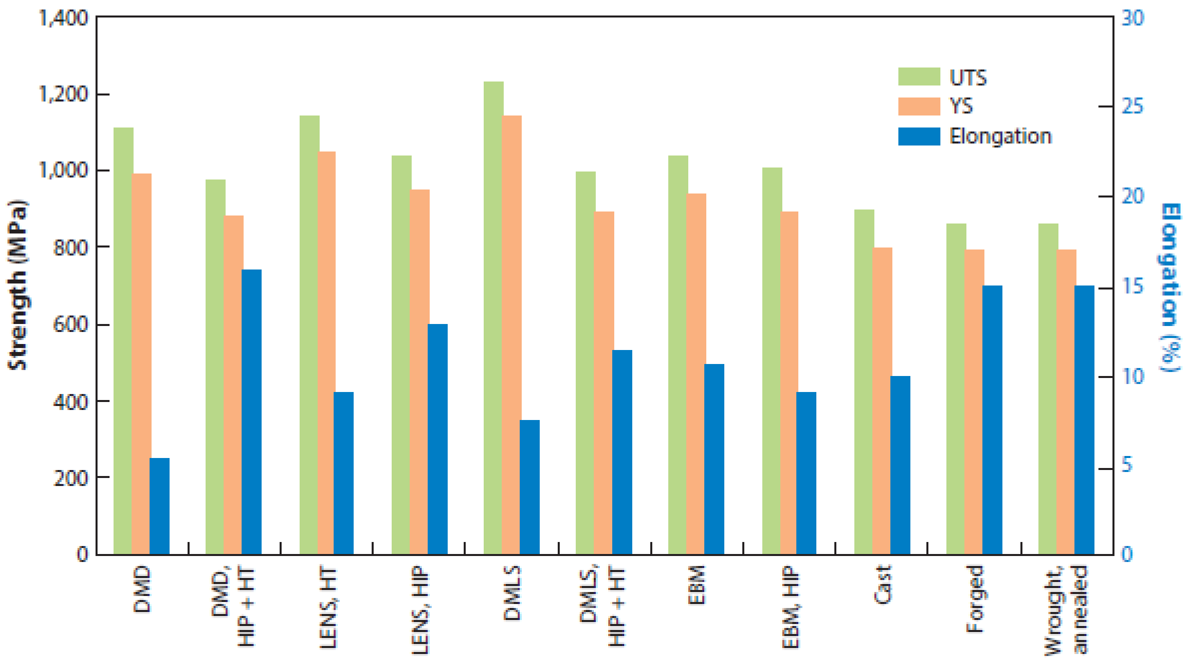

Figure 1.13: Strengths and elongations associated with various AM processed Ti-6Al-4V, adapted from [20]. Direct Metal Deposition (DMD), Laser Engineered Net Shaping (LENS), Direct Metal Laser Sintering (DMLS), Electron Beam Melting (EBM)

1.3. Thesis Overview

The work detailed in this dissertation was conducted under a collaborative research agreement with the Army Research Laboratory (ARL) funded through the National Center for Manufacturing Sciences (NCMS) Advanced Manufacturing, Materials, and Processes (AMMP) program. This work represents a collaboration between experimentalists and topology optimization designers in the Johns Hopkins Center for Additive Manufacturing and Architected Materials (JAM^2) and ARL scientists. The overall goal of the project being to "enable uptake of additively manufactured materials optimized for end-use applications to achieve significant mass reductions in Army systems". The research objective of this dissertation was to understand the fundamental of the additive process for Ti-6Al-4V and provide insight into the microstructural and mechanical response needed to adapt topology optimization methods. The chapters that follow detail experimental efforts to measure mechanical properties and characterize microstructures of LPBF Ti-6Al-4V under a variety of build and post-processed conditions.

Chapter 1, this chapter, outlines the motivation for the work described in this dissertation, and summarizes known mechanisms associated with additive manufacturing of Ti-6Al-4V. Chapter 2 outlines an investigation into anisotropic elasticity and the yield surface of LPBF Ti-6Al-4V through tensile, compressive, and shear mechanical testing. Chapter 3 further investigates the feasibility of using a novel shear mechanical test specimen for measurement of quasi-static shear properties with both finite element simulations and experimentation based on digital image correlation analysis. Chapter 4 describes a study of a novel titanium heat treatment, evaluated as an alternative to hot isostatic pressing. The effect of processing temperature on strength and fracture behavior are investigated through examination of tensile data and post-mortem microstructural characterization. Lastly, Chapter 5 summarizes key findings from this dissertation and provides an outlook for future work.

1.4. References for Chapter 1

1. Seifi, M., et al., *Overview of Materials Qualification Needs for Metal Additive Manufacturing.* Jom, 2016. **68**(3): p. 747-764.
2. Kruth, J.P., M.C. Leu, and T. Nakagawa, *Progress in Additive Manufacturing and Rapid Prototyping.* CIRP Annals, 1998. **47**(2): p. 525-540.
3. Frazier, W.E., *Metal Additive Manufacturing: A Review.* Journal of Materials Engineering and Performance, 2014. **23**(6): p. 1917-1928.
4. Froes, F.H. and B. Dutta, *The Additive Manufacturing (AM) of Titanium Alloys.* Advanced Materials Research, 2014. **1019**: p. 19-25.
5. *The LEAP Engine*. Available from: https://www.cfmaeroengines.com/engines/leap/.
6. Yan, R., et al., *Electron beam melting in the fabrication of three-dimensional mesh titanium mandibular prosthesis scaffold.* Sci Rep, 2018. **8**(1): p. 750.
7. Wilson, J.M., et al., *Remanufacturing of turbine blades by laser direct deposition with its energy and environmental impact analysis.* Journal of Cleaner Production, 2014. **80**: p. 170-178.
8. Brackett, D., I. Ashcroft, and R. Hague. *Topology optimization for additive manufacturing*. in *Proceedings of the solid freeform fabrication symposium, Austin, TX*. 2011.
9. Bendsoe, M.P. and O. Sigmund, *Topology optimization: theory, methods, and applications*. 2013: Springer Science & Business Media.
10. Bendsøe, M.P. and N. Kikuchi, *Generating optimal topologies in structural design using a homogenization method.* Computer Methods in Applied Mechanics and Engineering, 1988. **71**(2): p. 197-224.
11. Schwerdtfeger, J., et al., *Design of auxetic structures via mathematical optimization.* Adv Mater, 2011. **23**(22-23): p. 2650-4.
12. Pantelakis, S., et al., *Innovative concept of compliant mechanisms made by additive manufacturing.* MATEC Web of Conferences, 2019. **304**: p. 07002.
13. Diegel, O., A. Nordin, and D. Motte, *A Practical Guide To Design For Additive Manufacturing*. Springer Series in Advanced Manufacturing, ed. D.T. Pham. 2019, Singapore: Springer.
14. Schmelzle, J., et al., *(Re)Designing for Part Consolidation: Understanding the Challenges of Metal Additive Manufacturing.* Journal of Mechanical Design, 2015. **137**(11).
15. Liu, J., et al., *Current and future trends in topology optimization for additive manufacturing.* Structural and Multidisciplinary Optimization, 2018. **57**(6): p. 2457-2483.
16. Gaynor, A.T. and J.K. Guest, *Topology optimization considering overhang constraints: Eliminating sacrificial support material in additive manufacturing through design.* Structural and Multidisciplinary Optimization, 2016. **54**(5): p. 1157-1172.
17. Torres, A.P., et al., *Robust topology optimization under loading uncertainties via stochastic reduced order models.* International Journal for Numerical Methods in Engineering, 2021.
18. Yan, L., Y. Chen, and F. Liou, *Additive manufacturing of functionally graded metallic materials using laser metal deposition.* Additive Manufacturing, 2020. **31**: p. 100901.

19. Gruber, S., et al., *Comparison of dimensional accuracy and tolerances of powder bed based and nozzle based additive manufacturing processes.* Journal of Laser Applications, 2020. **32**(3): p. 032016.
20. Lewandowski, J.J. and M. Seifi, *Metal Additive Manufacturing: A Review of Mechanical Properties.* Annual Review of Materials Research, 2016. **46**(1): p. 151-186.
21. Yasa, E., J.P. Kruth, and J. Deckers, *Manufacturing by combining Selective Laser Melting and Selective Laser Erosion/laser re-melting.* CIRP Annals, 2011. **60**(1): p. 263-266.
22. Malekipour, E., A. Tovar, and H. El-Mounayri, *Heat Conduction and Geometry Topology Optimization of Support Structure in Laser-Based Additive Manufacturing.* 2018: p. 17-27.
23. Schmidt, M., et al., *Laser based additive manufacturing in industry and academia.* CIRP Annals, 2017. **66**(2): p. 561-583.
24. Gorsse, S., et al., *Additive manufacturing of metals: a brief review of the characteristic microstructures and properties of steels, Ti-6Al-4V and high-entropy alloys.* Science and Technology of Advanced Materials, 2017. **18**(1): p. 584-610.
25. Liu, P.W., et al., *Investigation on evolution mechanisms of site-specific grain structures during metal additive manufacturing.* Journal of Materials Processing Technology, 2018. **257**: p. 191-202.
26. Groeber, M.A., et al., *A Preview of the U.S. Air Force Research Laboratory Additive Manufacturing Modeling Challenge Series.* Jom, 2018. **70**(4): p. 441-444.
27. Patterson, A.E., S.L. Messimer, and P.A. Farrington, *Overhanging Features and the SLM/DMLS Residual Stresses Problem: Review and Future Research Need.* Technologies, 2017. **5**(2): p. 15.
28. Mercelis, P. and J.P. Kruth, *Residual stresses in selective laser sintering and selective laser melting.* Rapid Prototyping Journal, 2006. **12**(5): p. 254-265.
29. Rai, A., H. Helmer, and C. Körner, *Simulation of grain structure evolution during powder bed based additive manufacturing.* Additive Manufacturing, 2017. **13**: p. 124-134.
30. Le, K.Q., C. Tang, and C.H. Wong, *On the study of keyhole-mode melting in selective laser melting process.* International Journal of Thermal Sciences, 2019. **145**: p. 105992.
31. Seifi, M., et al., *Defect distribution and microstructure heterogeneity effects on fracture resistance and fatigue behavior of EBM Ti–6Al–4V.* International Journal of Fatigue, 2017. **94**: p. 263-287.
32. Shipley, H., et al., *Optimisation of process parameters to address fundamental challenges during selective laser melting of Ti-6Al-4V: A review.* International Journal of Machine Tools & Manufacture, 2018. **128**: p. 1-20.
33. H, G., et al., *Defect Morphology in Ti-6Al-4V Parts Fabricated by Selective Laser Melting and Electron Beam Melting*, in *24rd Annual International Solid Freeform Fabrication Symposium—an Additive Manufacturing Conference*. 2013: Austin, TX. p. 440-453.
34. Song, B., et al., *Effects of processing parameters on microstructure and mechanical property of selective laser melted Ti6Al4V.* Materials & Design, 2012. **35**: p. 120-125.
35. Yusuf, S.M. and N. Gao, *Influence of energy density on metallurgy and properties in metal additive manufacturing.* Materials Science and Technology, 2017. **33**(11): p. 1269-1289.

36. Yang, J.J., et al., *Prediction of microstructure in selective laser melted Ti-6Al-4V alloy by cellular automaton.* Journal of Alloys and Compounds, 2018. **748**: p. 281-290.
37. Yin, J., et al., *Thermal behavior and grain growth orientation during selective laser melting of Ti-6Al-4V alloy.* Journal of Materials Processing Technology, 2018. **260**: p. 57-65.
38. Zhang, Z., et al., *3-Dimensional heat transfer modeling for laser powder-bed fusion additive manufacturing with volumetric heat sources based on varied thermal conductivity and absorptivity.* Optics & Laser Technology, 2019. **109**: p. 297-312.
39. Carter, L.N., et al., *The influence of the laser scan strategy on grain structure and cracking behaviour in SLM powder-bed fabricated nickel superalloy.* Journal of Alloys and Compounds, 2014. **615**: p. 338-347.
40. Zhang, S., et al., *Effects of scan line spacing on pore characteristics and mechanical properties of porous Ti6Al4V implants fabricated by selective laser melting.* Materials & Design, 2014. **63**: p. 185-193.
41. Schwalbach, E.J., et al., *A discrete source model of powder bed fusion additive manufacturing thermal history.* Additive Manufacturing, 2019. **25**: p. 485-498.
42. Kudzal, A., et al., *Effect of scan pattern on the microstructure and mechanical properties of Powder Bed Fusion additive manufactured 17-4 stainless steel.* Materials & Design, 2017. **133**: p. 205-215.
43. Donegan, S.P., E.J. Schwalbach, and M.A. Groeber, *Zoning additive manufacturing process histories using unsupervised machine learning.* Materials Characterization, 2020. **161**: p. 110123.
44. Tapia, G. and A. Elwany, *A Review on Process Monitoring and Control in Metal-Based Additive Manufacturing.* Journal of Manufacturing Science and Engineering, 2014. **136**(6).
45. Everton, S.K., et al., *Review of in-situ process monitoring and in-situ metrology for metal additive manufacturing.* Materials & Design, 2016. **95**: p. 431-445.
46. Helle, A.S., K.E. Easterling, and M.F. Ashby, *Hot-isostatic pressing diagrams: New developments.* Acta Metallurgica, 1985. **33**(12): p. 2163-2174.
47. Atkinson, H.V. and S. Davies, *Fundamental aspects of hot isostatic pressing: An overview.* Metallurgical and Materials Transactions A, 2000. **31**(12): p. 2981-3000.
48. Rabin, B.H., G.R. Smolik, and G.E. Korth, *Characterization of entrapped gases in rapidly solidified powders.* Materials Science and Engineering: A, 1990. **124**(1): p. 1-7.
49. du Plessis, A. and E. Macdonald, *Hot isostatic pressing in metal additive manufacturing: X-ray tomography reveals details of pore closure.* Additive Manufacturing, 2020. **34**: p. 101191.
50. Hackel, L., et al., *Laser peening: A tool for additive manufacturing post-processing.* Additive Manufacturing, 2018. **24**: p. 67-75.
51. Lee, B.-S., et al., *Enhanced osseointegration of Ti6Al4V ELI screws built-up by electron beam additive manufacturing: An experimental study in rabbits.* Applied Surface Science, 2020. **508**: p. 145160.
52. Uhlmann, E., et al., *Additive Manufacturing of Titanium Alloy for Aircraft Components.* Procedia CIRP, 2015. **35**: p. 55-60.
53. Yadroitsev, I., P. Krakhmalev, and I. Yadroitsava, *Selective laser melting of Ti6Al4V alloy for biomedical applications: Temperature monitoring and microstructural evolution.* Journal of Alloys and Compounds, 2014. **583**: p. 404-409.

54. Kobryn, P.A. and S.L. Semiatin, *Microstructure and texture evolution during solidification processing of Ti–6Al–4V.* Journal of Materials Processing Technology, 2003. **135**(2-3): p. 330-339.
55. Marshall, G.J., et al., *Understanding the Microstructure Formation of Ti-6Al-4V During Direct Laser Deposition via In-Situ Thermal Monitoring.* Jom, 2016. **68**(3): p. 778-790.
56. Antonysamy, A.A., J. Meyer, and P.B. Prangnell, *Effect of build geometry on the beta-grain structure and texture in additive manufacture of Ti-6Al-4V by selective electron beam melting.* Materials Characterization, 2013. **84**: p. 153-168.
57. Lutjering, G.W., J.C., *Titanium*. 2nd Ed ed. 2007: Springer.
58. Schur, R., et al., *Mechanical anisotropy and its evolution with powder reuse in Electron Beam Melting AM of Ti6Al4V.* Materials & Design, 2021. **200**: p. 109450.
59. Carroll, B.E., T.A. Palmer, and A.M. Beese, *Anisotropic tensile behavior of Ti–6Al–4V components fabricated with directed energy deposition additive manufacturing.* Acta Materialia, 2015. **87**: p. 309-320.
60. Simonelli, M., Y.Y. Tse, and C. Tuck, *Effect of the build orientation on the mechanical properties and fracture modes of SLM Ti-6A1-4V.* Materials Science and Engineering a-Structural Materials Properties Microstructure and Processing, 2014. **616**: p. 1-11.
61. Zhao, P.Y., et al., *Slip transmission assisted by Shockley partials across alpha/beta interfaces in Ti-alloys.* Acta Materialia, 2019. **171**: p. 291-305.
62. Liu, S. and Y.C. Shin, *Additive manufacturing of Ti6Al4V alloy: A review.* Materials & Design, 2019. **164**: p. 107552.
63. Xu, W., et al., *Additive manufacturing of strong and ductile Ti–6Al–4V by selective laser melting via in situ martensite decomposition.* Acta Materialia, 2015. **85**: p. 74-84.
64. Welsch, G., et al., *Deformation characteristics of age hardened Ti-6Al-4V.* Metallurgical Transactions A, 1977. **8**(1): p. 169-177.

CHAPTER 2: CHARACTERIZING THE MECHANICAL RESPONSE OF LASER POWDER BED FUSION Ti-6Al-4V

2.1. Introduction

With the greatly enhanced geometric freedom enabled by additive manufacturing (AM) of metals comes increased complexity of processing and the associated material properties. The fast directional solidification rates inherent to laser powder bed fusion (LPBF) has been shown to generate microstructures and properties that are anisotropic and inhomogeneous [1]. With the wide range of processing parameters that produce microstructures ranging from columnar to equiaxed [2, 3], the introduction of new alloys being tailored specifically for LPBF [4], and the various post-processes that are often used, there is a critical need for testing that efficiently evaluates the resultant elastic, plastic, and failure properties.

Having a database of accurate properties and related processing states are needed to underpin computer design tools like topology optimization and to generate designs that can fully utilize the complexities of accessible geometries and materials [5]. For example, these tools can take advantage of the directional compliance of the printed material to generate unique mechanical responses from geometries like compliant mechanisms [6]. Populating a compliance tensor for a generalized orthotropic material requires the measurement of Young's moduli (E_x, E_y, E_z) in the build direction and two in plane directions along with the poisson's ratio ($\nu_{xy}, \nu_{zx}, \nu_{yz}$) and shear moduli ($G_{xy}, G_{zx}, G_{yz}$) . These nine independent elastic properties can be evaluated from the results of six experiments: three uniaxial tension and three shear.

$$\begin{bmatrix} \varepsilon_{xx} \\ \varepsilon_{yy} \\ \varepsilon_{zz} \\ \varepsilon_{yz} \\ \varepsilon_{zx} \\ \varepsilon_{xy} \end{bmatrix} = \begin{bmatrix} \frac{1}{E_{xx}} & -\frac{\nu_{yx}}{E_{yy}} & -\frac{\nu_{zx}}{E_{zz}} & 0 & 0 & 0 \\ -\frac{\nu_{xy}}{E_{xx}} & \frac{1}{E_{yy}} & -\frac{\nu_{zy}}{E_{zz}} & 0 & 0 & 0 \\ -\frac{\nu_{xz}}{E_{xx}} & -\frac{\nu_{yz}}{E_{yy}} & \frac{1}{E_{zz}} & 0 & 0 & 0 \\ 0 & 0 & 0 & \frac{1}{2G_{yz}} & 0 & 0 \\ 0 & 0 & 0 & 0 & \frac{1}{2G_{zx}} & 0 \\ 0 & 0 & 0 & 0 & 0 & \frac{1}{2G_{xy}} \end{bmatrix} \begin{bmatrix} \sigma_{xx} \\ \sigma_{yy} \\ \sigma_{zz} \\ \sigma_{yz} \\ \sigma_{zx} \\ \sigma_{xy} \end{bmatrix} \tag{2.1}$$

When evaluating a material for use in a structural application, understanding under which loads it will yield is crucial to ensure performance. In macroscopic yield prediction, the Von Mises maximum distortion criterion is commonly utilized with ductile metals. This is due to its simple formulation from a single tensile yield strength, though it is limited in accuracy by its isotropic assumption. This criterion was expanded by Hill to include weighting coefficients for the directional stress components to accommodate anisotropic yielding [7], later to be combined with Drucker and Prager's addition of a hydrostatic term by Liu et al to generate an anisotropic yield criterion that can account for asymmetry in tension and compression strengths [8, 9] as described by:

$$\begin{aligned} &\Big\{F\big(\sigma_{\mathrm{yy}} - \sigma_{\mathrm{zz}}\big)^2 + G(\sigma_{\mathrm{zz}} - \sigma_{\mathrm{xx}})^2 + H\big(\sigma_{\mathrm{xx}} - \sigma_{\mathrm{yy}}\big)^2 + 2L\sigma_{\mathrm{yz}}^2 + 2M\sigma_{\mathrm{zx}}^2 \\ &\quad + 2N\sigma_{\mathrm{xy}}^2\Big\}^{\frac{1}{2}} + I\sigma_{\mathrm{xx}} + J\sigma_{\mathrm{yy}} + K\sigma_{\mathrm{zz}} = 1 \end{aligned} \tag{2.2}$$

where:

$$F = \frac{1}{2}\left\{\left(\frac{\sigma_{\mathrm{yy}}^T + \sigma_{\mathrm{yy}}^C}{2\sigma_{\mathrm{yy}}^T\sigma_{\mathrm{yy}}^C}\right)^2 + \left(\frac{\sigma_{\mathrm{zz}}^T + \sigma_{\mathrm{zz}}^C}{2\sigma_{\mathrm{zz}}^T\sigma_{\mathrm{zz}}^C}\right)^2 - \left(\frac{\sigma_{\mathrm{xx}}^T + \sigma_{\mathrm{xx}}^C}{2\sigma_{\mathrm{xx}}^T\sigma_{\mathrm{xx}}^C}\right)^2\right\} \tag{2.3}$$

$$G = \frac{1}{2}\left\{\left(\frac{\sigma_{\mathrm{zz}}^{T} + \sigma_{\mathrm{zz}}^{C}}{2\sigma_{\mathrm{zz}}^{T}\sigma_{\mathrm{zz}}^{C}}\right)^{2} + \left(\frac{\sigma_{\mathrm{xx}}^{T} + \sigma_{\mathrm{xx}}^{C}}{2\sigma_{\mathrm{xx}}^{T}\sigma_{\mathrm{xx}}^{C}}\right)^{2} - \left(\frac{\sigma_{\mathrm{yy}}^{T} + \sigma_{\mathrm{yy}}^{C}}{2\sigma_{\mathrm{yy}}^{T}\sigma_{\mathrm{yy}}^{C}}\right)^{2}\right\} \tag{2.4}$$

$$H = \frac{1}{2}\left\{\left(\frac{\sigma_{\mathrm{xx}}^{T} + \sigma_{\mathrm{xx}}^{C}}{2\sigma_{\mathrm{xx}}^{T}\sigma_{\mathrm{xx}}^{C}}\right)^{2} + \left(\frac{\sigma_{\mathrm{yy}}^{T} + \sigma_{\mathrm{yy}}^{C}}{2\sigma_{\mathrm{yy}}^{T}\sigma_{\mathrm{yy}}^{C}}\right)^{2} - \left(\frac{\sigma_{\mathrm{zz}}^{T} + \sigma_{\mathrm{zz}}^{C}}{2\sigma_{\mathrm{zz}}^{T}\sigma_{\mathrm{zz}}^{C}}\right)^{2}\right\} \tag{2.5}$$

$$I = -\frac{\sigma_{\mathrm{xx}}^{T} - \sigma_{\mathrm{xx}}^{C}}{2\sigma_{\mathrm{xx}}^{T}\sigma_{\mathrm{xx}}^{C}} \tag{2.6}$$

$$J = -\frac{\sigma_{\mathrm{yy}}^{T} - \sigma_{\mathrm{yy}}^{C}}{2\sigma_{\mathrm{yy}}^{T}\sigma_{\mathrm{yy}}^{C}} \tag{2.7}$$

$$K = -\frac{\sigma_{\mathrm{zz}}^{T} - \sigma_{\mathrm{zz}}^{C}}{2\sigma_{\mathrm{zz}}^{T}\sigma_{\mathrm{zz}}^{C}} \tag{2.8}$$

$$L = \frac{1}{2\left(\tau_{\mathrm{yz}}^{S}\right)^{2}} \tag{2.9}$$

$$M = \frac{1}{2(\tau_{\mathrm{zx}}^{S})^{2}} \tag{2.10}$$

$$N = \frac{1}{2\left(\tau_{\mathrm{xy}}^{S}\right)^{2}} \tag{2.11}$$

This formulation requires the tensile and compressive yield strengths in each principal direction $\left(\sigma_{xx}^{T}, \sigma_{yy}^{T}, \sigma_{zz}^{T}, \sigma_{xx}^{C}, \sigma_{yy}^{C}, \sigma_{zz}^{C}\right)$ as well as the shear strengths between them $\left(\tau_{xy}, \tau_{zx}, \tau_{yz}\right)$, a total of nine independent values to calculate the coefficients of (2.2). Each pertain to a component of anisotropy: F-H deviatoric, I-K hydrostatic, and L-N shear. The hydrostatic terms I-K give rise to the asymmetric nature of the yield criterion. The requisite material properties can be determined by nine experiments: three uniaxial tension, three uniaxial compression, and three shear. Tension and compression specimens are easily manufactured from cylindrical rods, though shear historically has not been as straightforward to investigate.

Compact forced-simple-shear specimens (CFSS) put forth by Vecchio and Grey can be tested in a standard quasistatic load frame as well as high strain rate experiments like Kolsky bars [10]. This geometry was designed to be easily machinable from cylinders and produce close to a pure shear state without requiring specialized setups like a biaxial load frame [11, 12]. Biaxial experiments have been used to investigate anisotropic plasticity as well as fracture with LPBF metals with high accuracy [13-15]. The CFSS geometry can be utilized with DIC to produce local measures of shear properties, while being easy to machine, more cost efficient, and readily accessible to test in a standard mechanical testing laboratory setting.

Figure 2.1: Compression, tension, and CFSS shear samples used in testing compliance and yielding behavior.

2.2. Materials and Methods

2.2.1. Sample Fabrication

All samples used in this study were machined from 12.7 mm diameter cylinders printed in 0°, 45°, and 90° orientations with respect to the build direction as shown in Figure 2.2. A 3DSystems ProX320 machine was used to fabricate samples using the following laser parameters: power of 300 W, raster speed of 1225 mm/s, hatch spacing and layer height of 90 μm. These parameters have been demonstrated to produce fully dense as-built material (>99.9% dense) [16-18]. All parts were stress relieved at a temperature of 600 °C for 4 hours before removal from the build plate. Samples then underwent HIP at 955 °C for an hour while under 206 MPa positive pressure with Ar gas. The temperature was chosen to be high enough to allow for closure of pores without exceeding the β transus temperature. A final aging treatment consisted of holding the parts at 525 °C for 8 hours to allow for the formation of Ti_3Al α_2 precipitates. This combination of laser parameters and post-processing steps was selected to replicate standard processing conditions used in industrial applications that have been shown to produce optimally fully dense parts with wrought-like microstructures and mechanical properties [19, 20]. The intention being to collect a "best case" baseline set of properties to develop the fundamental understanding of LPBF Ti-6Al-4V, evaluating the elastic properties and yield criterion described in (2.1) and (2.2).

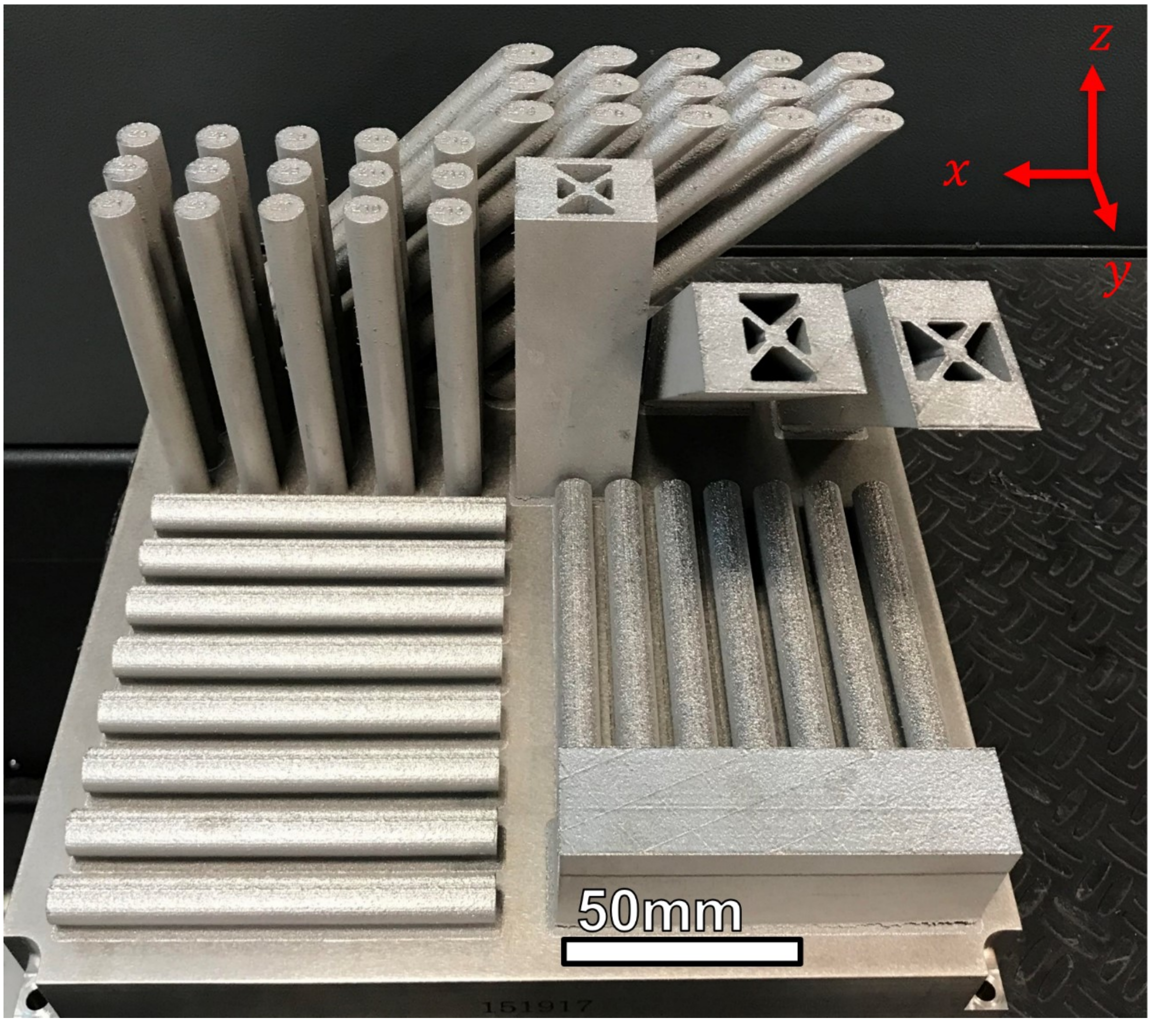

Figure 2.2: As-built cylinders of LPBF Ti-6Al-4V before being removed from build plate and machined into compression, tension and CFSS mechanical test specimens. “X-element” samples included in build to be used in experiments to mimic nodes within lattice structures. Build completed on 3DSystems ProX320 using laser parameters: power of 300 W, raster speed of 1225 mm/s, hatch spacing and layer height of 90 μm.

Heat-treated cylinders were then machined into tension and compression samples in accordance with ASTM E8 and E9 standards for monotonic tension and compression experiments, 33 of each type were made to provide statistic distributions for the three printed orientations. To measure bulk properties without surface effects and generate uniform mechanical test specimens, the machining was conducted to remove as-built surface roughness. Monotonic tensile tests were carried out on an Instron 1125 screw driven load frame with a 100 kN load cell. Tension samples with a gage diameter of 3 mm and length of 9 mm were held with cylindrical wedge grips and were loaded to failure. Monotonic compression tests were loaded in an Instron 1332 servo-hydraulic load frame with a 250 kN load cell. Samples with 11 mm diameter and 38 mm in height were compressed just beyond the point of yielding between hardened steel plattens with mineral oil lubricating the contact surfaces to minimize friction. CFSS specimens were machined to investigate shear response; the undeformed shear area was 2.336 mm by 2.336 mm. CFSS samples were tested in an MTS servo-hydraulic load frame with a 22 kN load cell, the samples compressed between similarly lubricated plattens.

Figure 2.3: (a) Instron 1125 screw driven load frame used for tension samples, (b) Instron 1332 servo-hydraulic load frame used for compression samples, (c) MTS servo-hydraulic load frame used for shear samples, and (d) Admet eXpert 5000 used for reversed tension-compression samples.

Six additional flat samples were electrical discharge machined with modified geometries from ASTM E606 specification for reversed loading ultralow cycle fatigue tests. These reversable samples had a rectangular gage of 1 mm by 1.12 mm. They enabled combined loading experiments to confirm bulk findings while using a consistent geometry and testing equipment to remove any effects from dimensional or equipment variations. An ADMET eXpert 5602 screw driven load frame with a 2.2 kN load cell and flat bar compression grips were used to reversibly load samples between tension and compression. Before testing, all mechanical specimens were speckled in preparation for DIC, which was used to calculate resultant strains. Samples were loaded at a strain rate of 3 x 10^{-4} s^{-1} while images were captured every second. Bulk compression and tension samples were speckled using a standard white spray paint base and misting of black paint for the speckles. These tests were imaged by two cameras for 3D DIC, which were calibrated beforehand by capturing at least 20 images of a calibration grid provided VIC3D (Correlated Solutions). Combined tension-compression and shear samples had speckle patterns applied using a mixture of black polyester powder (printer toner) and white acrylic paint via airbrush.

2.2.2. Preparation for Microstructural Characterization

Metallographic specimens to be characterized were sectioned with EDM and hot pressed into conductive graphite resin prior to mechanical grinding and polishing to a final 0.5 μm colloidal silica step. As-polished samples were examined with X-ray diffraction (XRD) using a Phillips X-ray Diffractometer which employs a Cu-Kα source emitting a wavelength of 1.54 Å for initial macro-texture measurements. Micro-texture was investigated by electron backscatter diffraction (EBSD) in a Tescan Mira SEM with an Oxford EBSD detector with 20 kV accelerating voltage. Additional polished samples were etched using Kroll's reagent for 10 seconds to reveal the underlying microstructure via optical microscopy. The etchant achieves this by selectively etching and highlighting the small amount retained β phase that resides at the boundaries of the α phase. Material in the form of 3 mm diameter cylinders were machined and subjected to micro computed tomography using a RX Solutions EasyTom X-Ray MicroCT system with a tungsten source using a voltage of 80 kV and current of 166 μA. The scan reconstructions were made using RX Solutions software with a minimum voxel size of 2.8 μm.

2.3. Experimental Results

2.3.1. Microstructural Characterization

Optical micrographs revealing the structure of α (light phase) and β (dark phase) are shown in Figure 2.4. These images were captured perpendicular to the build direction (side view), and the lathes appear to have undergone a large amount of growth from the fine structure that is typical of as-built Ti-6Al-4V materials [21]. The largest of the highly acicular lathes reach lengths of 70 μm, approaching the printed layer height and hatch spacing of 90 μm. The boundaries of the prior β grains (that solidify before the formation of α lathes) are not recognizable in the optical micrographs. The quasi-static yield and failure behavior are not strongly affected by the prior β grains but are instead dominated by the effective dislocation mean-free-path, which depends on lathe size. Larger α lathes tends to lower strength and increase ductility [2].

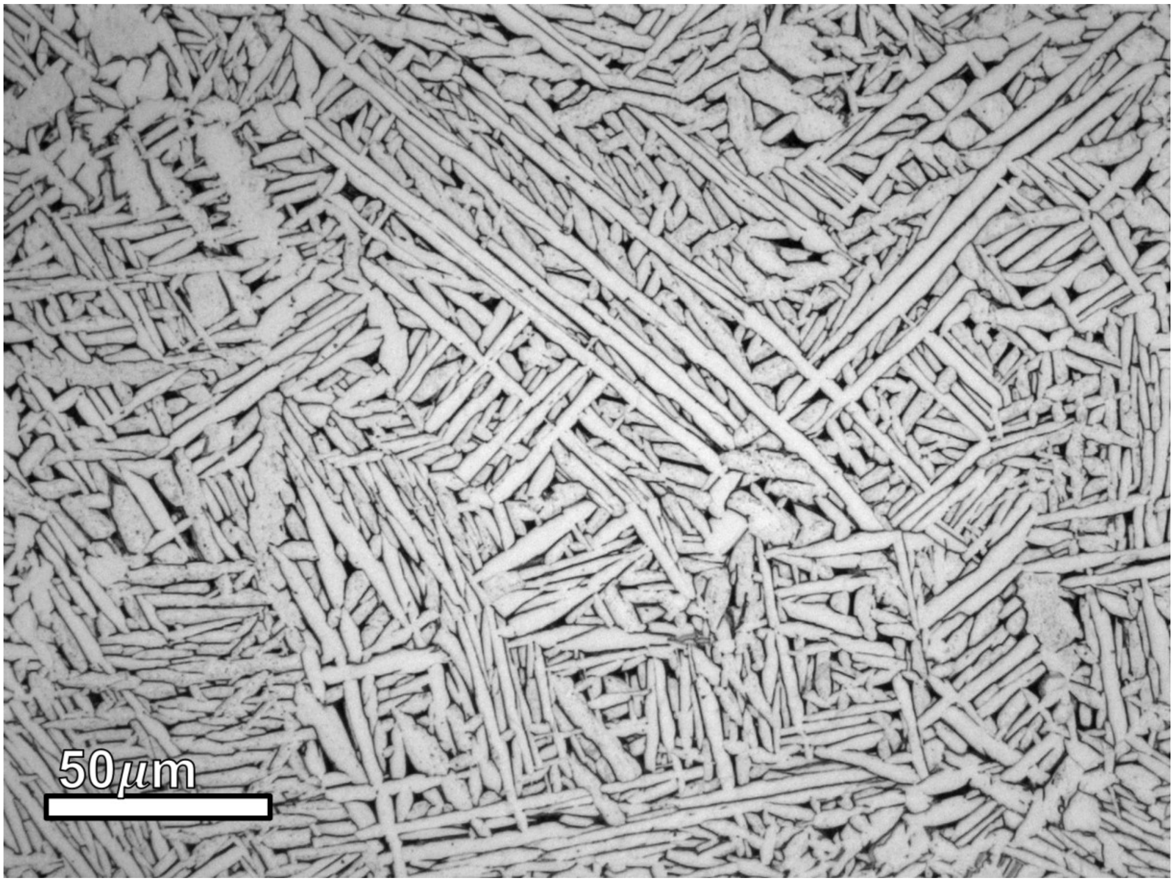

Figure 2.4: Optical micrographs of etched (α+β) lamellar structure.

XRD spectra from samples with surfaces perpendicular to the build direction are shown in Figure 2.5. The samples of 3 mm thickness were cut by EDM with their top surfaces at build heights of 4.5 mm and 9 mm from the base plate. The large peaks correlate to the α HCP phase and the small peaks correlate to the β BCC phase, indicating that there is small amount of β in the microstructure, as typically observed in micrographs for a two-phase alloy. The relative α phase peak heights are comparable to those of powder diffraction results, indicating that there is not a strong macrotexture within the material.

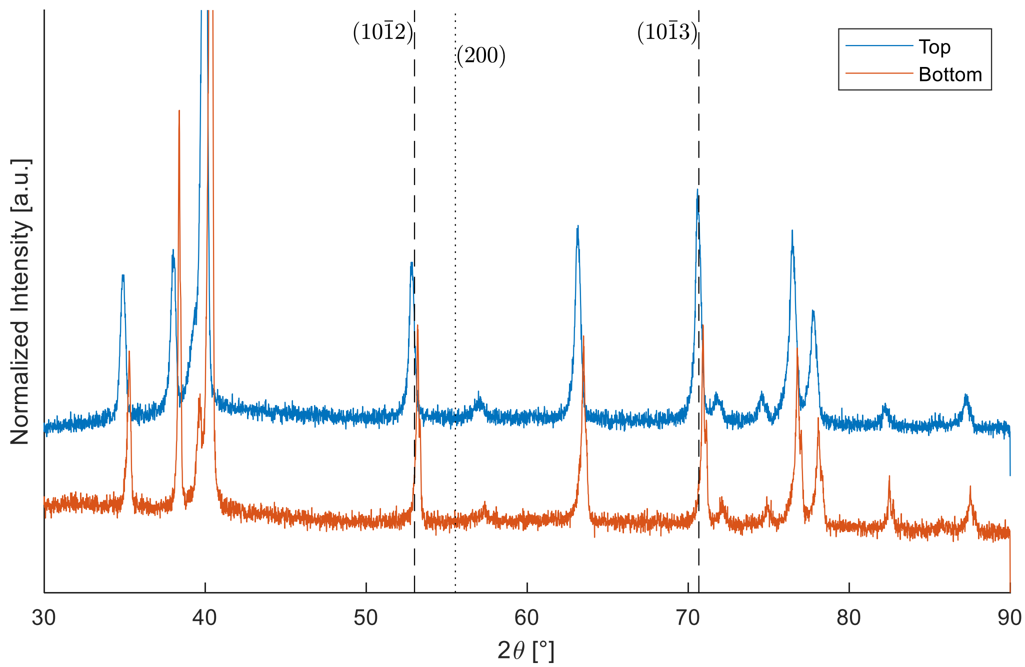

Figure 2.5: (a) XRD spectra from scans with surface normal in build direction on (b) two samples cut from 0° orientation printed bar with build heights of 4.5 mm and 9 mm. Dashed and dotted lines indicate peak positions from powder diffraction of select α-HCP and β-BCC planes, respectively.

As discussed in the introduction section, the β phase energetically favors solidifying with the [001] axis in the direction of the maximum thermal gradient, which is nominally in the build direction during the LPBF process. Unfortunately, the peaks of β are too faint make determinations of texture. The α phase forms lathes within the prior β grains with its orientations expressing one of twelve variants of the Burger's relation $(0001)_\alpha \parallel \{101\}_\beta$, $\langle 11\bar{2}0\rangle_\alpha \parallel \langle 1\bar{1}\bar{1}\rangle_\beta$. Unfortunately, this large number of variants leads to a reduction in α texture from any texture that may have been present in the β phase and prohibits measurement of β texture.

Examples of powder diffraction peak positions are displayed in Figure 2.5 by the vertical lines on the spectra to highlight the shifts in the collected peaks. The shifts for all peaks are quantified in Table 2.1. The α HCP peaks are close enough to be recognizably paired with the powder peaks with shifts of only 0.2°. In the case of the (200) peak for the β BCC phase, the small experimental peak has a much larger shift of 2° to the right. These peak shifts result in an average lattice strain of -0.52 % in α and -3.01 % in β for the 4.5 mm build height sample, and 0.04 % in α and -2.51 % in β for the 9mm height sample. This variation in lattice strains suggest that there is still a small amount of residual stress remaining in the material.

Table 2.1: Calculated peak positions, interplane spacing, and resultant lattice strains from the XRD spectra in Figure 2.5.

		Powder Diffraction		Bottom Sample			Top Sample		
	Plane	2θ [°]	d [A]	2θ [°]	Δd [Å]	ε [%]	2θ [°]	Δd [Å]	ε [%]
Alpha	$(10\bar{1}0)$	35.1	2.56	35.3	-0.015	-0.57	34.9	0.014	0.55
	(0002)	38.4	2.34	38.4	0.002	0.07	38.0	0.023	0.97
	$(10\bar{1}1)$	40.2	2.24	40.4	-0.011	-0.48	40.0	0.011	0.49
	$(10\bar{1}2)$	53.0	1.73	53.2	-0.006	-0.37	52.8	0.005	0.31
	$(11\bar{2}0)$	63.0	1.48	63.5	-0.012	-0.81	63.2	-0.004	-0.28
	$(10\bar{1}3)$	70.7	1.33	70.9	-0.005	-0.34	70.6	0.001	0.07
	$(20\bar{2}0)$	74.2	1.28	74.9	-0.011	-0.87	74.5	-0.006	-0.43
	$(11\bar{2}2)$	76.2	1.25	76.8	-0.008	-0.65	76.5	-0.004	-0.31
	$(20\bar{2}1)$	77.4	1.23	78.1	-0.010	-0.80	77.8	-0.006	-0.48
	(0004)	82.3	1.17	82.5	-0.003	-0.21	82.2	0.001	0.07
	$(20\bar{2}2)$	86.8	1.12	87.5	-0.008	-0.70	87.3	-0.006	-0.50
Beta	(110)	38.5	2.34	39.7	-0.069	-2.94	39.7	-0.066	-2.83
	(200)	55.5	1.65	57.4	-0.048	-2.92	57.1	-0.041	-2.46
	(211)	69.6	1.35	72.1	-0.041	-3.07	71.8	-0.037	-2.70
	(220)	82.4	1.17	85.7	-0.037	-3.12	84.7	-0.024	-2.05

Inverse pole figure maps from EBSD scans, conducted on samples with surface normals parallel to the build and in plane directions, are shown in Figure 2.6(a and b), respectively. In addition to providing a more detailed view of the size and shape of the α lamellar structure, this also shows that there are not recognizable colonies of parallel lathes that share the same variant and Burger's relation in the microstructure. Continuous colonies provide a more favorable path for dislocation motion, as their Burger's vector does not have to undergo as large a change to be transmitted across the lathe boundaries [22]. Figure 2.6(c) shows the small amount (~4%) of retained β phase that lies on the boundaries. This retained β was also noted in the XRD results and will affect the transmission of dislocations. Though the boundaries of the prior β grains are not clearly identifiable from the morphology of the α lathes, since the lathes share the same original β orientation that determines their orientation, they can be used to reconstruct the prior β grains. There are automated approaches to generate maps of the prior β orientations with open source software like the MTEX Matlab plugin [23]. Though this was not implemented in this work an example of a prior β grain boundary is visually outlined in Figure 2.6(a) from the grouping of repeated variant orientations.

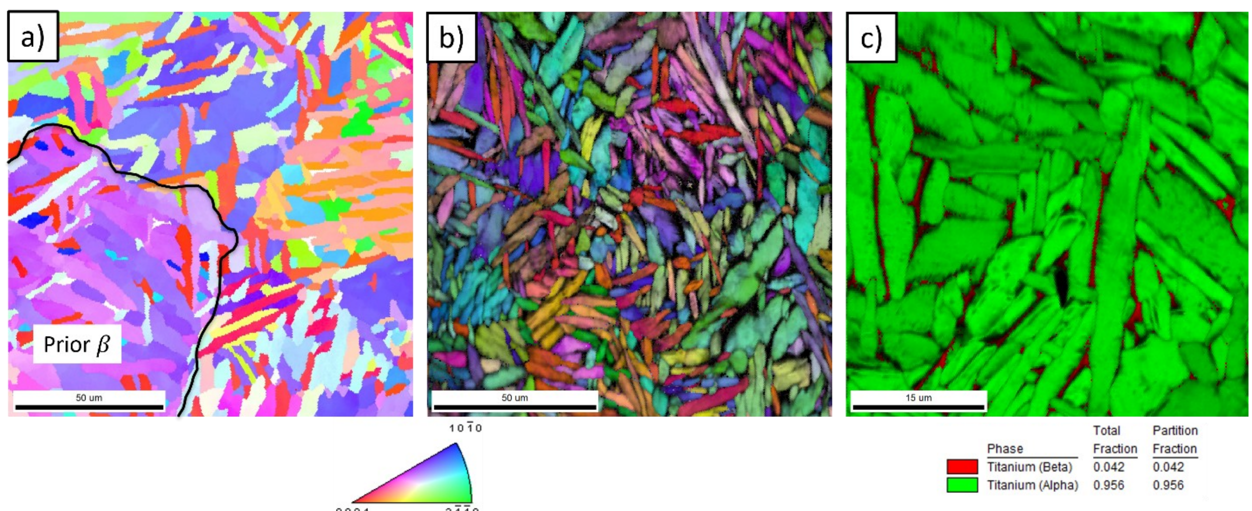

Figure 2.6: EBSD results: α phase IPF orientation maps in (a) build direction and (b) in plane direction. (c) Phase map revealing small amount of retained β at the α lathe boundaries.

An example of μCT results with a pixel size of 2.8 μm from a fractured tensile sample are shown in Figure 2.7. No porosity was evident in the undeformed material; the minimum detection limit of 10 μm (at least 3 pixels across to be confident in identification). Lack of fusion defects from insufficient powder coverage or melting are on the size order of layer heights (>90 μm), and smaller trapped gas pores (~20 μm), often referred to as keyhole voids, would both be large enough to be detected [24, 25]. This confirms that the selected print and post-processing parameters produced a fully dense material without print defects as was the intention. Voids associated with ductile fracture are visible in Figure 2.7(b), where the solid material is transparent and the air above the surface as well as the voids are opaque black.

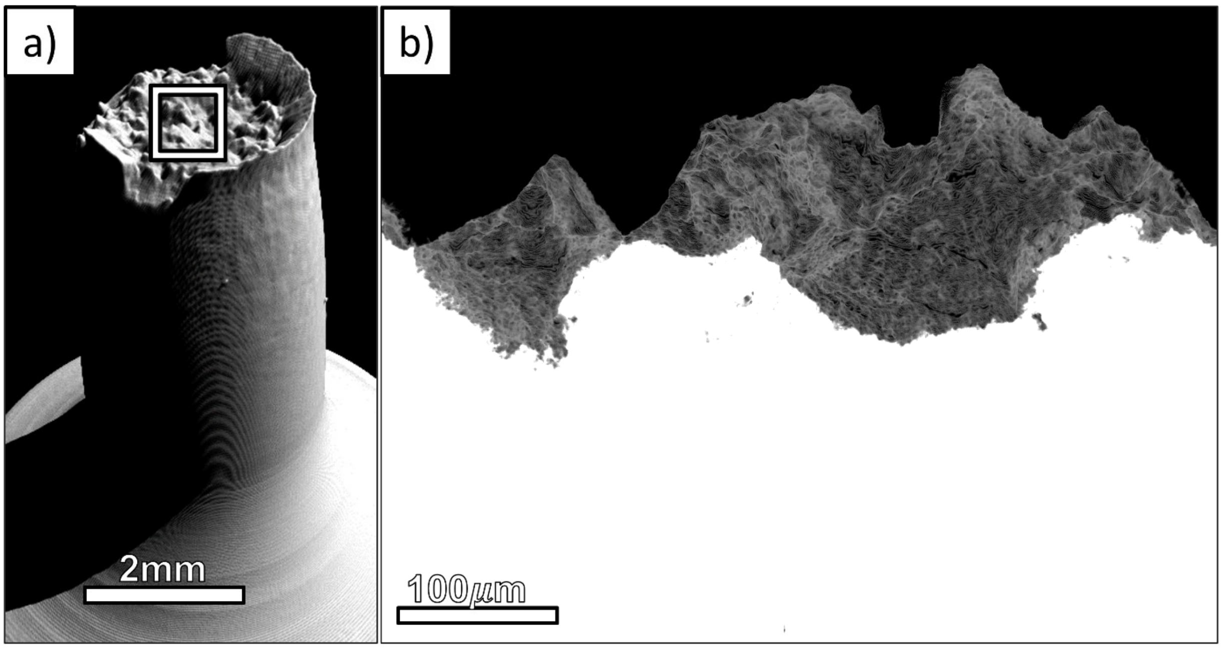

Figure 2.7: Reconstructed CT scans of (a) fractured tensile sample gage section with box highlighting the location of (b) a close-up of the fracture surface with solid material transparent and the voids opaque that shows some void growth associated with fracture. Black is air/voids, solid material is white. Pixel size of 2.8 μm.

2.3.2. Mechanical Testing

The stress-strain curves that resulted from the monotonic tension, compression, and shear test are depicted in Figure 2.8, Figure 2.9, and Figure 2.10, respectively. Average elastic, plastic and failure properties calculated from tests are displayed with their standard deviations in Table 2.2 for each orientation: parallel to, perpendicular to, and 45° from the build direction. The samples printed perpendicular to the build direction (parallel to the build plate) are grouped together as only a substantial number of cylinders from one of the two in plane orientations were usable due to complications in removing them from the build plate. Yield strengths were calculated by extrapolating from 0.2% plastic strain offset to the intersection with the flow curves using the measured moduli. There is no indication of directional anisotropy within the tension, compression, or shear datasets, but there was clear evidence of a tension-compression asymmetry in yielding. The measured compressive yield strengths were on average 10% higher than those in tension. The material exhibited a very high elongation to failure in tension, with the least ductile samples reaching at least 20% strain. The measured tensile strengths and elongation to failure meet the requirements as set by the ASTM B348 standard for Grade 5 Ti-6Al-4V. Measured shear strengths were 45% that of the tensile; for ductile metals this is commonly 57% (the Von Mises equivalent ratio between a pure tension and a pure shear stress state).

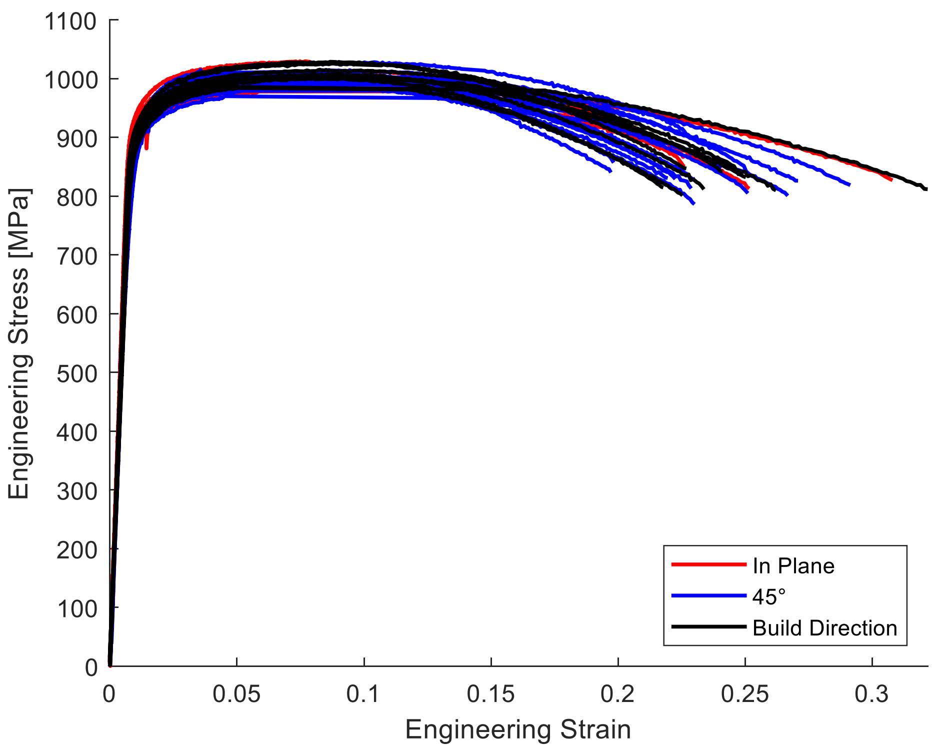

Figure 2.8: Monotonic tension stress-strain curves for 11 samples parallel to, 7 samples perpendicular to, and 15 samples 45° from the build direction.

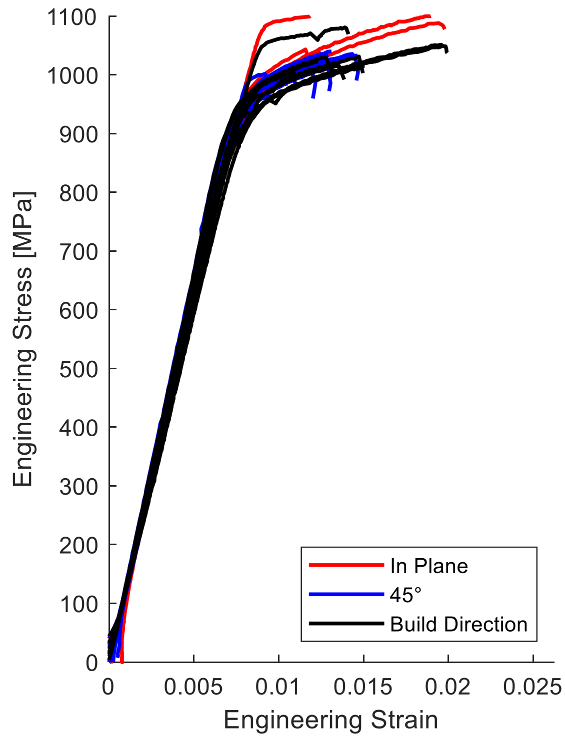

Figure 2.9: Monotonic compression stress-strain curves for 11 samples parallel to, 8 samples perpendicular to, and 15 samples 45° from the build direction.

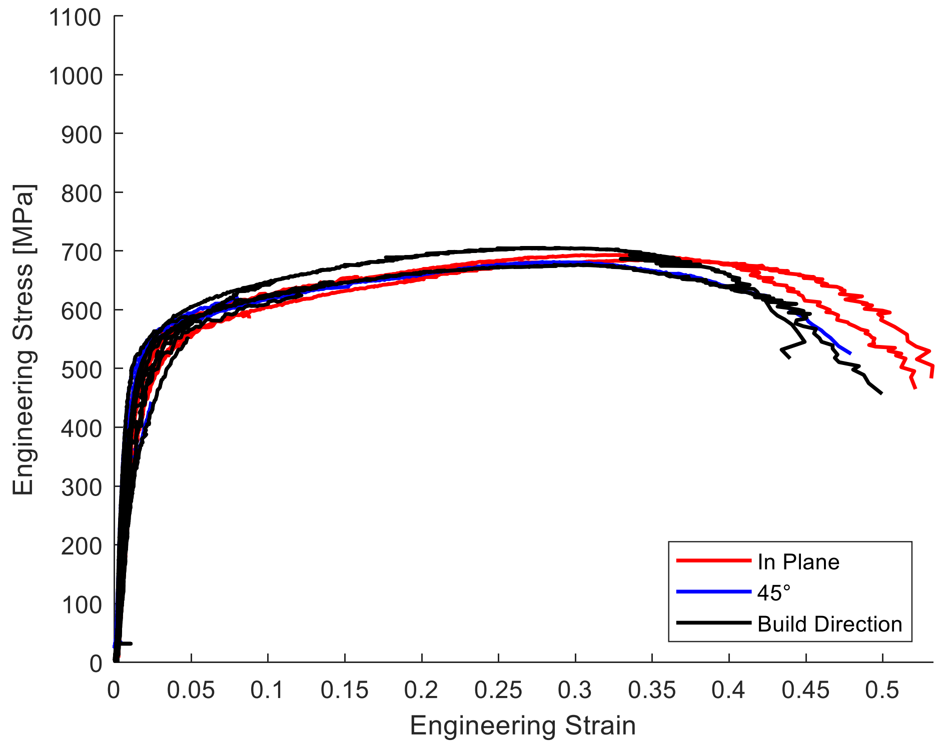

Figure 2.10: Monotonic shear stress-strain curves for 10 samples parallel to, 9 samples perpendicular to, and 8 samples 45° from the build direction.

Table 2.2: Calculated mechanical properties from monotonic tension, compression, and shear tests shown in Figure 2.8-Figure 2.10. Reference data from similarly processed material included.

Orientation	E [GPa]	G [GPa]	ν	σ^T [MPa]	σ^C [MPa]	τ [MPa]	elong %
⊥BD	116 ± 7	42 ± 8	0.31 ± 0.01	903 ± 16	1011 ± 36	410 ± 36	25 ± 3
45°	110 ± 3	49 ± 14	0.32 ± 0.01	883 ± 16	984 ± 29	404 ± 89	25 ± 3
BD	113 ± 6	43 ± 16	0.31 ± 0.02	890 ± 10	987 ± 30	414 ± 33	23 ± 3
Ref [17]	115 ± 1	-	-	885 ± 3	-	-	19 ± 0.5

The apparent yield asymmetry was investigated further using reversed loading tension-compression experiments as illustrated in Figure 2.11. All reversed loading tests were conducted in the build plane (⊥BD) orientation. Each test was loaded through at least 2 cycles of tension and compression to varying levels of strain before reversing and ultimately loaded in tension to failure. For each test only the initial yield, whether that be compressive or tensile, is reported. The subsequent yield upon reversing for each case is less sharply defined as it deviates from linearity well before reaching the full strength. This may be due to the Bauschinger effect that describes strain hardening in one loading direction causing a softening in the reverse. As it hardens in one direction, the produced dislocations are of an opposite sign as those produced when the loading is reversed, causing dislocation annihilation that hinders the accumulation of dislocations that enable hardening [26]. This effect increases with the amount of pre-strain and has been observed previously with LPBF Ti-6Al-4V [27]. Initial yield strengths also exhibit a tension-compression asymmetry like the bulk tests, though the compressive yield strengths are slightly lower – only 5% higher than the tensile strengths in the reversed tests. The calculated Young's moduli in these tests are slightly higher than those from the bulk tension tests but within the standard deviation.

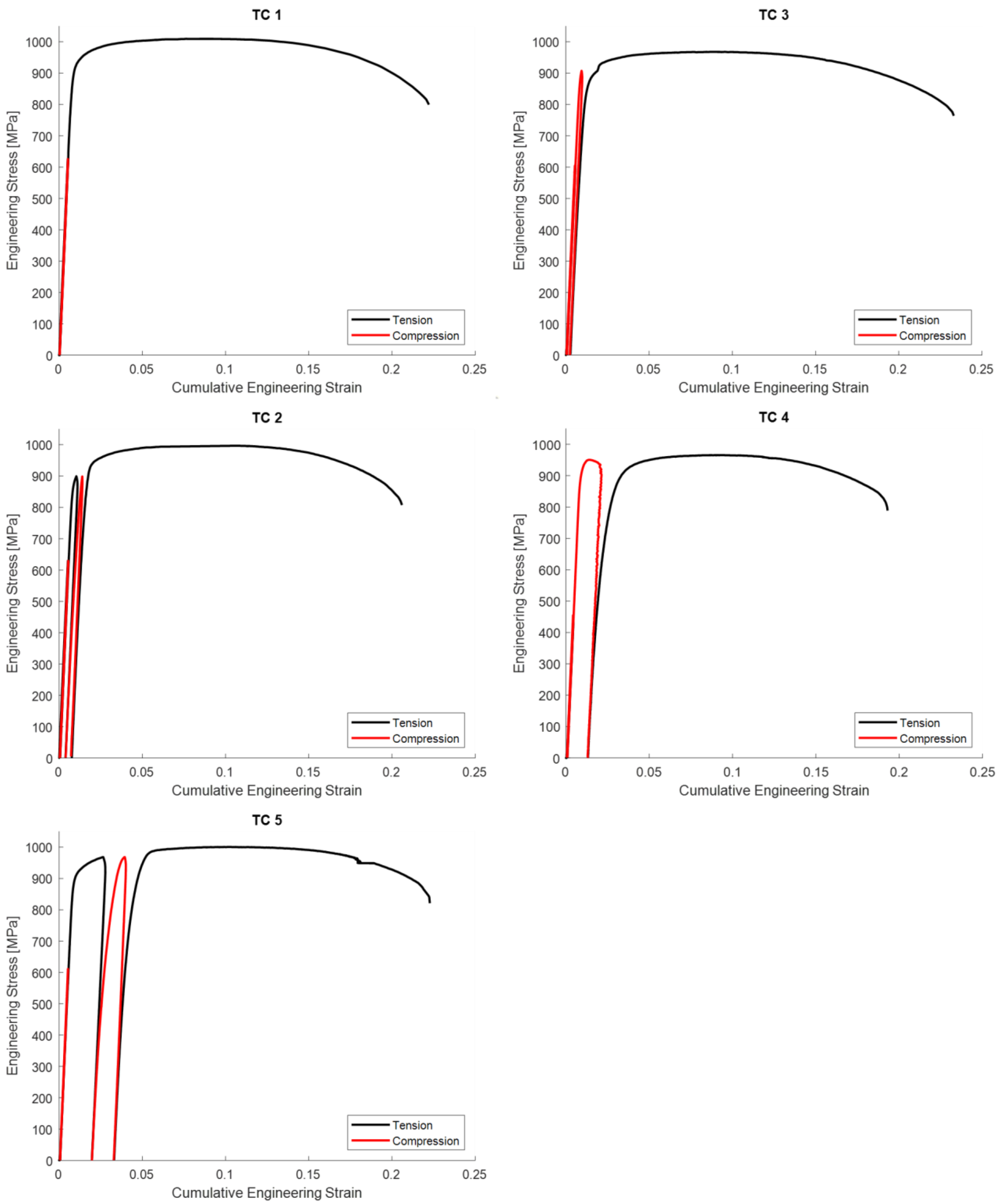

Figure 2.11: Reversed tension-compression stress strain curves, specimen prepared at 0° (⊥BD) orientation.

Table 2.3: Calculated properties from reversed tension-compression tests shown in Figure 2.11. Yield values are from initial yield in each test.

Sample	E [GPa]	σ^T [MPa]	σ^C [MPa]	Cumulative strain %
1	116	897	-	23.4
2	119	871	-	21.8
3	119	-	923	23.0
4	120	-	948	19.3
5	121	880	-	22.3
Average	119.0±1.7	882.6±13.2	935.5±17.7	21.9±1.6

2.4. Discussion

In line with the absence of crystallographic texture in the microstructure of the HIPed LPBF Ti-6Al-4V, no statistically significant directional anisotropy was measured in the tension, compression, or shear properties. The average measured tensile modulus (113$\pm$7 GPa) is comparable to results from similarly processed material (115$\pm$1 GPa). The measured tensile yield strengths (892$\pm$15 MPa) were also close to the reference values (885$\pm$3 MPa). The material exhibited a very high amount of ductility (25$\pm$3 %) that is comparable to or higher than similarly processed LPBF Ti64 (19$\pm$0.5 %) [17]. This ductility can be attributed to the material having a fully dense microstructure, and the presence of large alpha lathes allowing for long dislocation slip distances. A tension-compression asymmetry in the yield strength was measured in the monotonic tests and confirmed in the reversed tension-compression tests. There are observations of tension-compression asymmetry in the Ti-6Al-4V literature [28-31]. It is generally attributed to non-Schmid effects on pyramidal slip systems that make the yield strength dependent on the two orthogonal shear stress components and three normal stress components, as well as the shear stress in the direction of slip.

The coefficients for the yield criteria model in (2.2) are listed in Table 2.4 and were calculated using the monotonic tension, compression, and shear yield data described in Table 2.2 for the build direction BD and in plane (⊥BD). An assumption of transverse isotropy was used in the calculation with the in-plane directions being equivalent (G=H, J=K, and M=N). Though there was not a significant difference between the in plane and build direction properties, the coefficients were still calculated using the respective values. The asymmetry of the yield criteria can be seen in the plane stress biaxial yield surface shown with experimental data points in Figure 2.12. The experimental uniaxial values agree well with the model while the measured shear strengths (defined by a 0.2% offset method) fall well below the yield curves which suggests that the compact forced simple-shear test has complications accurately measuring the initial yield point. Unlike in an uniaxial test, plasticity in the CFSS sample does not initiate homogenously which results in a less sharply defined elastic-plastic transition. This is evident in Figure 2.8 where the shear has a much less sharply defined transition from elastic to plastic. This is further illustrated by the disparity in strain hardening: tensile yield strength of 900 MPa and ultimate tensile strength of 1000 MPa compared to the shear yield strength of 400 MPa and ultimate strength of 700 MPa. The true shear yield strength is likely higher than measured by the 0.2% offset method, which is consistent with the fact that the Von Mises equivalent of 900 MPa in tension would be 520 MPa in shear. Additionally biaxial tests on LPBF Ti-6Al-4V have reported similarly higher values for yielding in pure shear [14]. Taking all this into account a closer investigation of the mechanical response in the CFSS geometry is warranted which is undertaken in the subsequent chapter.

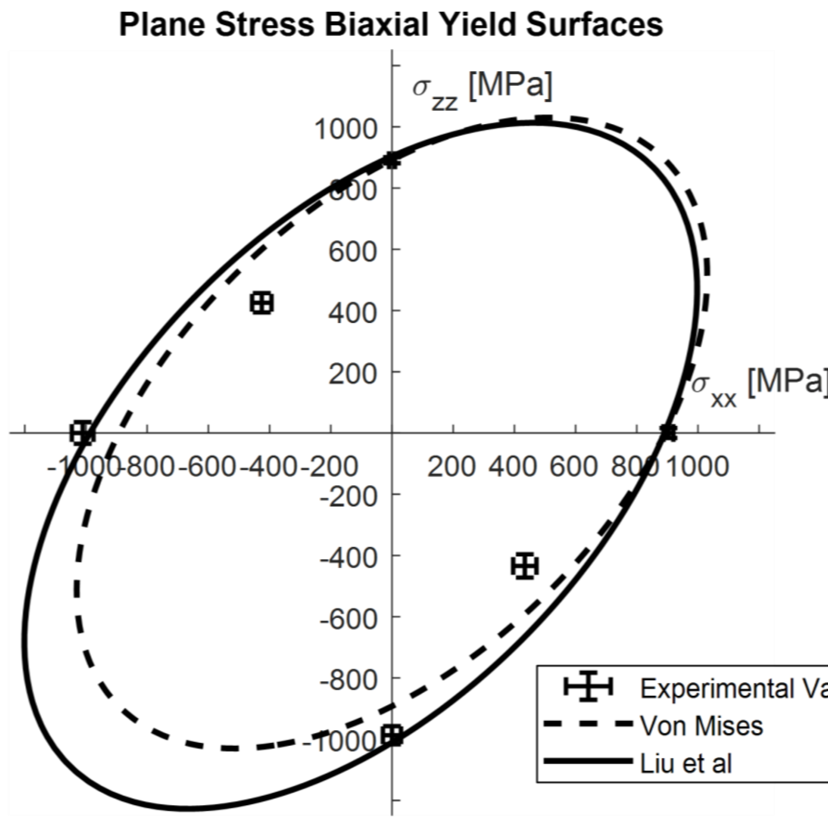

Figure 2.12: Plane stress biaxial yield surface calculated using measured experimental values shown. Tension and compression yield strengths are captured well by the asymmetric model, measured shear strengths lie well below expected values.

Table 2.4: Coefficients for yield criterion (2.2) as plotted in Figure 2.12.

F	G	H	I	J
5.284×10^{-7}	5.701×10^{-7}	5.701×10^{-7}	5.469×10^{-5}	5.873×10^{-5}

K	L	M	N
5.873×10^{-5}	1.638×10^{-6}	2.268×10^{-6}	2.268×10^{-6}

2.5. Chapter Summary

In this chapter experimental procedures were demonstrated to efficiently measure mechanical properties that accurately reflect the elastic and yield behavior of an anisotropic and asymmetric material. A comprehensive study was undertaken and completed in order to accurately characterize LPBF Ti-6Al-4V in a stress relieved, HIPed and aged condition. The results contribute to, and support, the growing literature on LBPF Ti-6Al-4V and have been used to inform topology optimization models developed by our collaborators. Additively manufactured metals commonly have anisotropic microstructures and properties due to the directional solidification inherent in LPBF. Through a combination of monotonic tension, compression, and shear experiments, each oriented in unique material directions an accurate description of the elastic and yield properties of these complex materials can be formed. The standard HIP processed Ti-6Al-4V exhibited a tension-compression asymmetry and an exceptionally high tensile ductility, but no statistically significant anisotropy. This asymmetry has been quantified and imported into TO models, enabling more accurate designs of lightweight lattices and structures. The CFSS shear geometry, is a cost effective and rapid testing method to generate a measure of shear properties along with the added capability of being tested at high strain rates (and high temperatures) when required for an application. The measured shear yield strengths were notably lower than expected when compared against the full yield behavior; further investigation is required and is detailed in the chapter to follow.

2.6. References for Chapter 2

1. Kok, Y., et al., *Anisotropy and heterogeneity of microstructure and mechanical properties in metal additive manufacturing: A critical review.* Materials & Design, 2018. **139**: p. 565-586.
2. Beese, A.M. and B.E. Carroll, *Review of Mechanical Properties of Ti-6Al-4V Made by Laser-Based Additive Manufacturing Using Powder Feedstock.* Jom, 2016. **68**(3): p. 724-734.
3. Körner, C., *Additive manufacturing of metallic components by selective electron beam melting — a review.* International Materials Reviews, 2016. **61**(5): p. 361-377.
4. Pollock, T.M., A.J. Clarke, and S.S. Babu, *Design and Tailoring of Alloys for Additive Manufacturing.* Metallurgical and Materials Transactions A, 2020. **51**(12): p. 6000-6019.
5. Gaynor, A.T. and J.K. Guest, *Topology optimization considering overhang constraints: Eliminating sacrificial support material in additive manufacturing through design.* Structural and Multidisciplinary Optimization, 2016. **54**(5): p. 1157-1172.
6. Pantelakis, S., et al., *Innovative concept of compliant mechanisms made by additive manufacturing.* MATEC Web of Conferences, 2019. **304**: p. 07002.
7. Hill, R., *A theory of the yielding and plastic flow of anisotropic metals.* Proceedings of the Royal Society of London. Series A. Mathematical and Physical Sciences, 1948. **193**(1033): p. 281-297.
8. Drucker, D.C. and W. Prager, *Soil mechanics and plastic analysis or limit design.* Quarterly of Applied Mathematics, 1952. **10**(2): p. 157-165.
9. Liu, C., *On the asymmetric yield surface of plastically orthotropic materials: A phenomenological study.* Acta Materialia, 1997. **45**(6): p. 2397-2406.
10. Gray, G.T., K.S. Vecchio, and V. Livescu, *Compact forced simple-shear sample for studying shear localization in materials.* Acta Materialia, 2016. **103**: p. 12-22.
11. Cady, C.M., et al., *The Shear Response of Beryllium as a Function of Temperature and Strain Rate.* EPJ Web of Conferences, 2018. **183**: p. 02017.
12. Mohr, D. and M. Oswald, *A New Experimental Technique for the Multi-axial Testing of Advanced High Strength Steel Sheets.* Experimental Mechanics, 2007. **48**(1): p. 65-77.
13. Wilson-Heid, A.E. and A.M. Beese, *Fracture of laser powder bed fusion additively manufactured Ti–6Al–4V under multiaxial loading: Calibration and comparison of fracture models.* Materials Science and Engineering: A, 2019. **761**: p. 137967.
14. Wilson-Heid, A.E., S. Qin, and A.M. Beese, *Anisotropic multiaxial plasticity model for laser powder bed fusion additively manufactured Ti-6Al-4V.* Materials Science and Engineering: A, 2018. **738**: p. 90-97.
15. Wilson-Heid, A.E., S. Qin, and A.M. Beese, *Multiaxial plasticity and fracture behavior of stainless steel 316L by laser powder bed fusion: Experiments and computational modeling.* Acta Materialia, 2020. **199**: p. 578-592.
16. Shipley, H., et al., *Optimisation of process parameters to address fundamental challenges during selective laser melting of Ti-6Al-4V: A review.* International Journal of Machine Tools & Manufacture, 2018. **128**: p. 1-20.
17. Kasperovich, G. and J. Hausmann, *Improvement of fatigue resistance and ductility of TiAl6V4 processed by selective laser melting.* Journal of Materials Processing Technology, 2015. **220**: p. 202-214.

18. Van Hooreweder, B., et al., *Analysis of Fracture Toughness and Crack Propagation of Ti6Al4V Produced by Selective Laser Melting.* Advanced Engineering Materials, 2012. **14**(1-2): p. 92-97.
19. H, G., et al., *The Effects of Processing Parameters on Defect Regularity in Ti-6Al-4V Parts Fabricated By Selective Laser Melting and Electron Beam Melting*. 2013. p. 424-439.
20. Song, B., et al., *Effects of processing parameters on microstructure and mechanical property of selective laser melted Ti6Al4V.* Materials & Design, 2012. **35**: p. 120-125.
21. Xu, W., et al., *Additive manufacturing of strong and ductile Ti–6Al–4V by selective laser melting via in situ martensite decomposition.* Acta Materialia, 2015. **85**: p. 74-84.
22. Zhao, P.Y., et al., *Slip transmission assisted by Shockley partials across alpha/beta interfaces in Ti-alloys.* Acta Materialia, 2019. **171**: p. 291-305.
23. Tiley, J.S., et al., *3D reconstruction of prior beta grains in friction stir-processed Ti-6Al-4V.* J Microsc, 2014. **255**(2): p. 71-7.
24. Cunningham, R., et al., *Keyhole threshold and morphology in laser melting revealed by ultrahigh-speed x-ray imaging.* Science, 2019. **363**(6429): p. 849-852.
25. H, G., et al., *Defect Morphology in Ti-6Al-4V Parts Fabricated by Selective Laser Melting and Electron Beam Melting*, in *24rd Annual International Solid Freeform Fabrication Symposium—an Additive Manufacturing Conference*. 2013: Austin, TX. p. 440-453.
26. Yoshida, F. and T. Uemori, *A model of large-strain cyclic plasticity describing the Bauschinger effect and workhardening stagnation.* International Journal of Plasticity, 2002. **18**(5-6): p. 661-686.
27. Knezevic, M., et al., *Thermo-hydrogen refinement of microstructure to improve mechanical properties of Ti–6Al–4V fabricated via laser powder bed fusion.* Materials Science and Engineering: A, 2021. **809**: p. 140980.
28. Roberts, W., et al., *Tension–compression asymmetry of 〈c+a〉 slip in Ti–6Al.* Scripta Materialia, 2020. **178**: p. 119-123.
29. Neeraj †, T., et al., *Observation of tension–compression asymmetry in α and titanium alloys.* Philosophical Magazine, 2005. **85**(2-3): p. 279-295.
30. Lowden, M.A.W. and W.B. Hutchinson, *Texture Strengthening and Strength Differential in Titanium-6al-4v.* Metallurgical Transactions, 1975. **A 6**(3): p. 441-448.
31. Ding, R., et al., *〈c+a〉 Dislocations in deformed Ti–6Al–4V micro-cantilevers.* Acta Materialia, 2014. **76**: p. 127-134.

CHAPTER 3: INVESTIGATION OF THE STRESS-STRAIN RESPONSE IN COMPACT FORCED-SIMPLE-SHEAR SPECIMENS DURING QUASI-STATIC LOADING

3.1. Introduction

The directional dependence of elasticity, yield, and failure are vital inputs for load-bearing applications that rely on structural rigidity and strength. While tension and compression mechanical tests are straight-forward to conduct on a selected volume in a specific direction, investigation of shear responses is not as simple to implement or as thoroughly understood. Shear by nature is difficult to investigate experimentally due to the inclusion of other non-shear stress components often preventing a perfect shear stress state. High fidelity surrogate models have been developed to predict the shear response of materials, but they are no substitute for experimentally measuring the elastic-plastic shear response of a material.

Quasi-static biaxial load frames, illustrated in Figure 3.1(a), enable a precise control of applied shear and normal forces to a thin sheet specimen and have been shown to give accurate measures of yielding and fracture behavior through a range of loading states [1]. The applied loading state is described by a loading angle β that is defined as:

$$tan\,\beta = \frac{F_{\perp}}{F_{\parallel}} \cong \frac{\sigma_{xx}}{\tau_{xy}} \tag{3.1}$$

where $F_{\perp}$ and $F_{\parallel}$ are the loading forces normal and parallel to the shear direction, respectively. While the numerator in the biaxial case illustrated in Figure 3.1(a) would be σ_{yy}, to remain consistent with the orientations used for the analysis described in this work, σ_{xx} is used here. Loading angle of β=0° and β=90° correspond to pure shear and pure tension loading cases, respectively. The normal and shear strain components develop in a consistent ratio and can be measured by digital image correlation (DIC) as shown in Figure 3.1(b). These setups must be extremely stiff to avoid introduction of compliance and unwanted moments and they are often not found in a typical laboratory setting.

Geometries like so-called “top-hat” or shear-compression specimens (SCS) shown in Figure 3.1(c,d) that are capable of being loaded in more standard frames are used in the literature [2-4]. Both geometries can generate significant normal stresses, that affect the results, but they are commonly used in high strain rate experiments involving adiabatic shear banding. In the case of the top-hat specimen the sheared surface rotates during testing incorporating volumes on either side of the geometry and making it difficult to sample a specific volume or orientation [5]. The geometry prevents a complete elimination of a bending moment and a significant portion of loading energy is used to expanding the lower “brim” portion [6].

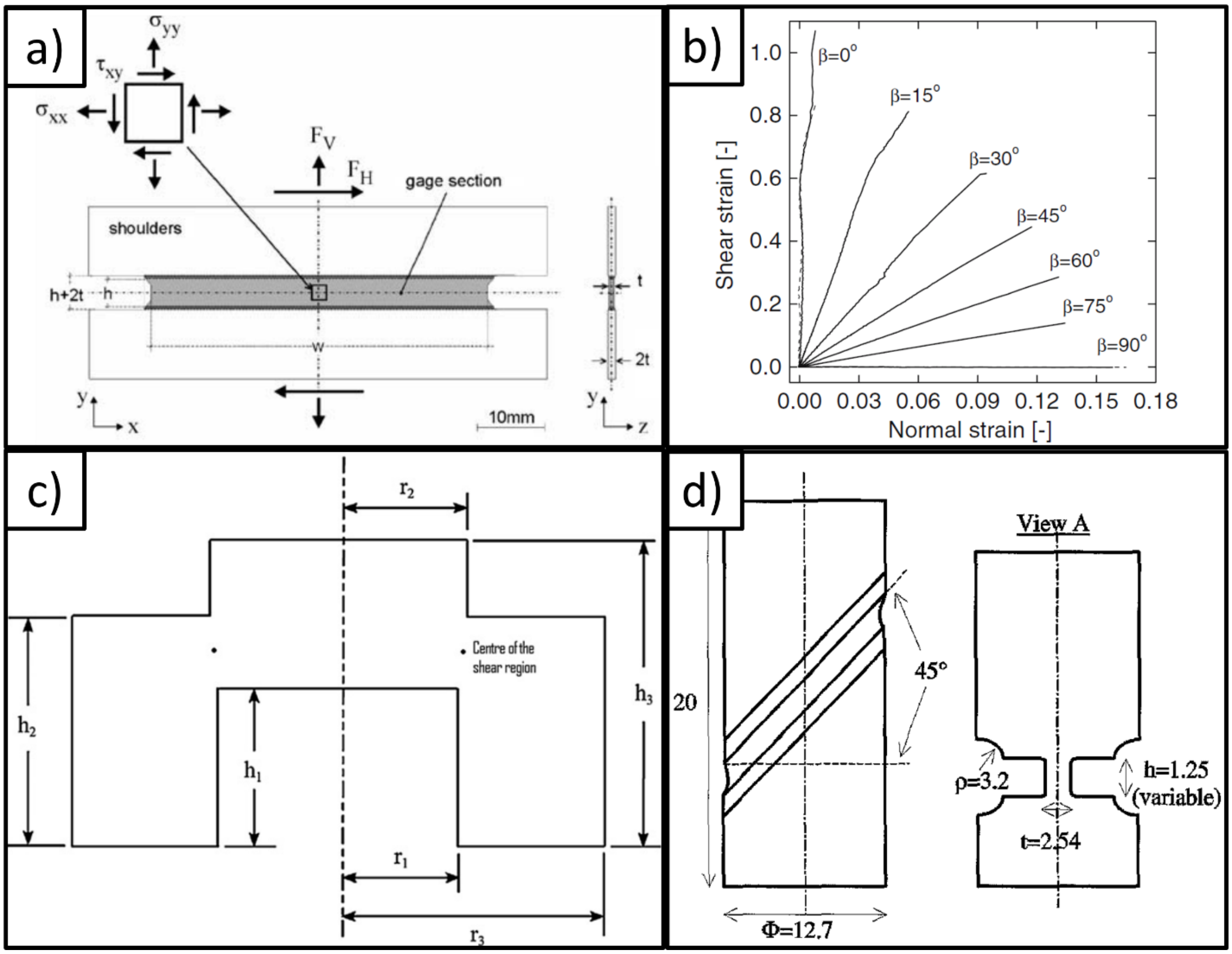

Figure 3.1: (a) Biaxial loading experimental setup, (b) evolution of normal and shear strains under different loading angles β adapted from [1]. (c) Top-hat specimen geometry [2], (d) shear-compression specimen geometry [4].

Gray et. al. introduced a new specimen geometry referred to as the compact forced-simple-shear (CFSS) shown in Figure 3.2(a), which is easily machined, can be oriented in particular material directions, and lends well to quasistatic and high rate testing [7]. The CFSS geometry aims to address the challenges of other shear specimen geometries and to approach Mode II loading, thus enabling a more direct quantification of the shear stress – shear strain response from experimental data. The CFSS has been used with DIC to investigate shear deformation modes across quasi and high strain rates, primarily for adiabatic shear banding [8]. The current work explores using enhanced DIC analysis for the reliable measurement of elastic, yield, and failure properties. The resultant stress and strain states within the geometry were evaluated using a finite element plasticity model of wrought material to compare to quasistatic experimental results. The implementation of DIC and post-analysis with the objective of producing a measure of strain which when combined with measured loads could be used to formulate an accurate stress-strain response. Finally, the technique was evaluated through repeated tests on samples manufactured from a rolled bar of grade 5 Ti-6Al-4V.

3.2. Stress State Validation

A finite element (FE) model of the CFSS geometry was generated and used as a comparison to experimental data that was collected using the wrought material. The model was used to evaluate the stress state through the volume as only boundary loading and surface displacement information is measurable experimentally. The sample geometry was designed using SolidWorks 2017 with corners modeled with a 0.1 mm radius to reflect the true as-machined sample geometry. The edges where surfaces intersect were checked for large angular deviations to prevent sharp interfaces that may cause singularity issues in meshing the geometry as displayed in Figure 3.2(b).

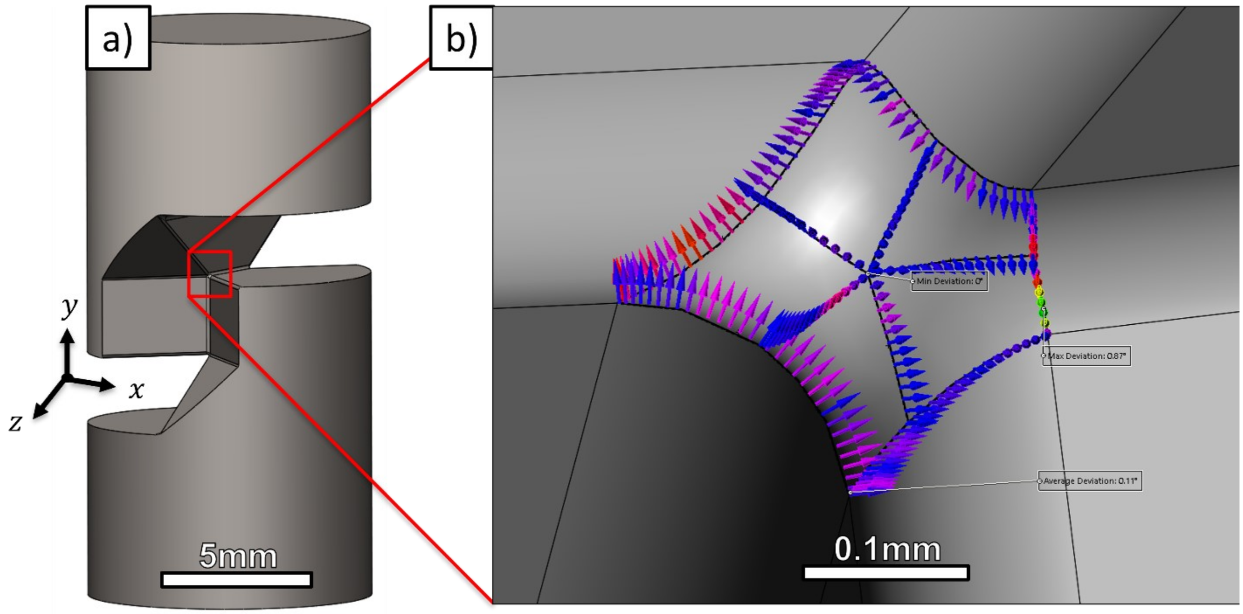

Figure 3.2: (a) CFSS sample geometry generated in SolidWorks. (b) angular deviations across edge interfaces to check for sharp corners that would generate mesh singularities with maximum deviation of 0.87° (vector arrow colors correlate with deviation: minimum blue, maximum red).

To ensure that model material properties reflect the grade 5 Ti-6Al-4V used in the experiments that follow, the tensile stress-strain response was first measured. The flat tensile sample with a gage of 1 mm x 1 mm was machined using EDM and speckled using a mixture of white airbrush paint and printer toner to enable DIC strain measurements shown in Figure 3.3(a). The sample was loaded up to 900 MPa and unloaded to ensure accurate measurement of modulus before loading to failure using an ADMET eXpert 5602 screw driven load frame with a 2.2 kN load cell. The Poisson's ratio was calculated by a linear fit of the normal strains in the elastic regime. Finally, the true stress - true plastic stain curve was determined by subtracting the elastic strain from the total strain beyond yielding:

$$\varepsilon_{plastic} = \varepsilon_{total} - \varepsilon_{elastic} = \varepsilon_{total} - \frac{\sigma}{E} \tag{3.2}$$

This is done to define the strain hardening behavior that is dependent only on the plastic component; only tensile data up to the point of necking was used as the model did not include any failure mechanics.

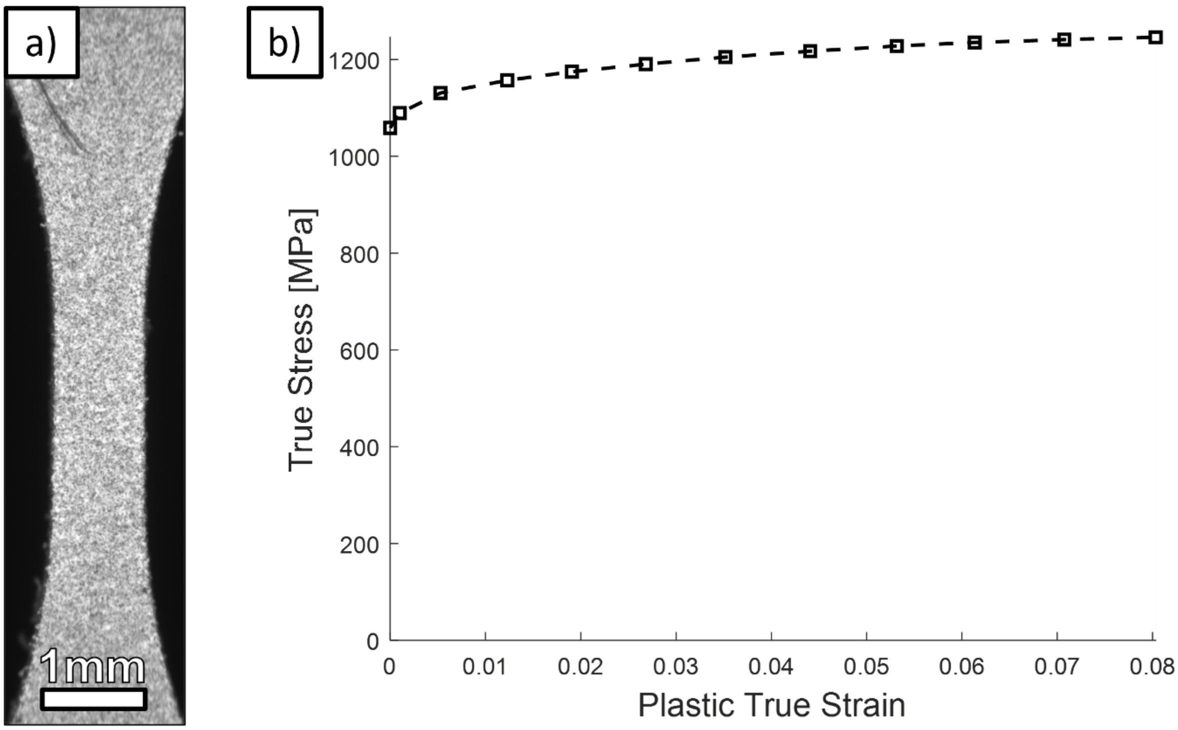

Figure 3.3: (a) Tension sample, (b) resultant true stress-true plastic strain curve used to define isotropic hardening model with squares indicating endpoints of linear sections. Data beyond necking is not included as the hardening model does not include failure mechanisms.

Table 3.1: Elastic properties defined in finite element model. Properties were experimentally measured values from the same grade 5 Ti-6Al-4V used in shear experiments.

E [GPa]	v	G [GPa]	k [GPa]
92.9	0.26	36.7	65.7

The finite element model was generated in Ansys Mechanical 2020 using a quasistatic multilinear isotropic hardening model adapted with measured tensile stress-strain response outlined in Figure 3.3 and Table 3.1. The large deflections option was also enabled to avoid small strain assumptions. The full mesh and a cross section of the sheared plane is displayed in Figure 3.4. Larger tetrahedral element sizes of 0.8 mm were used for the bulk of the geometry to conserve computing power while transmitting the loading condition to the sheared volume where the stress concentrations are higher. Element mesh sizing of 0.1 mm and 0.025 mm was used for the sheared volume and filleted edges, respectively. The refined mesh sizes were evaluated for stress singularities in the linear-elastic regime starting at sizes of 0.25 mm and 0.1. From the evolution of the maximum averaged and unaveraged stress values the final sizes were determined to provide adequate convergence.

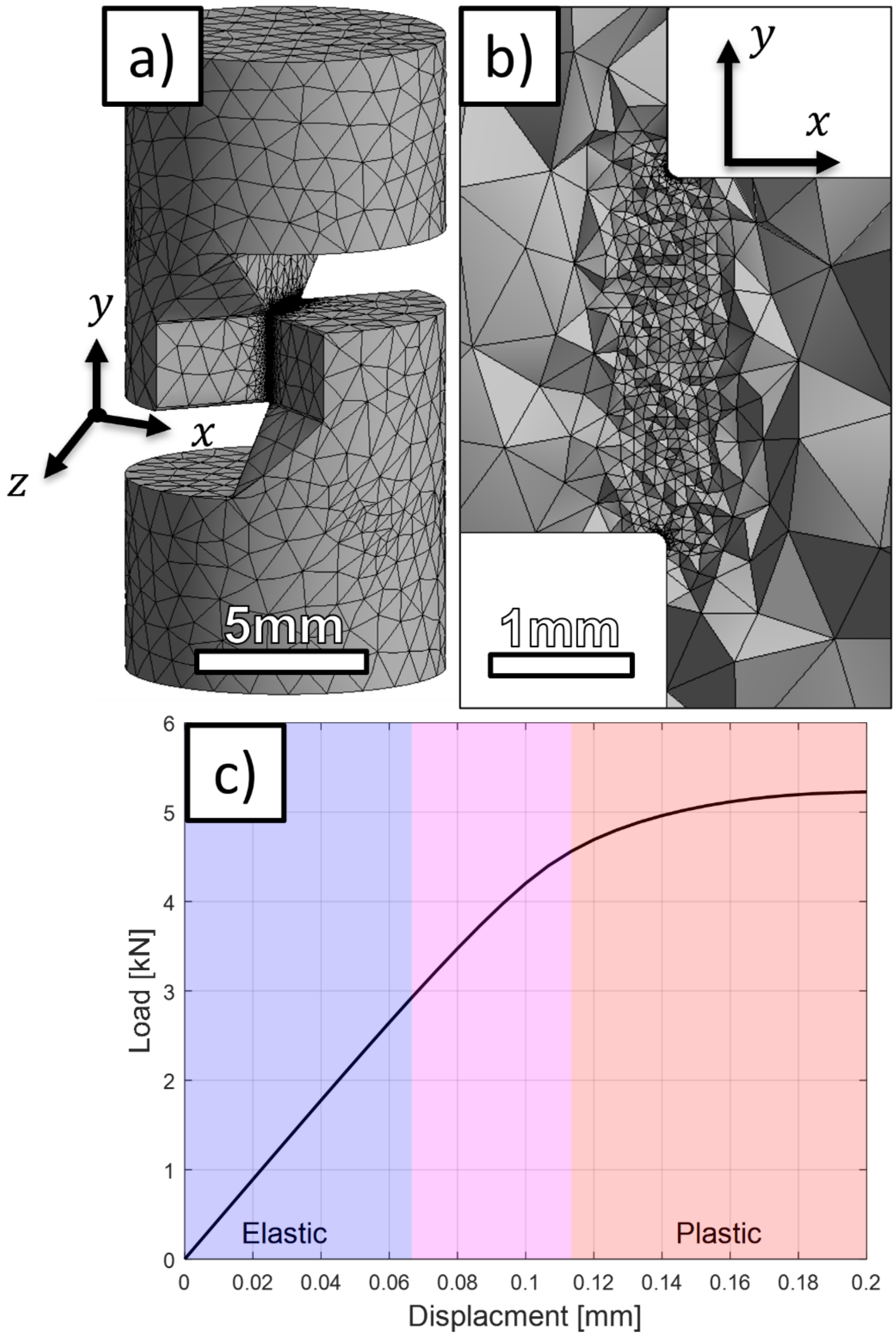

Figure 3.4: Mesh of compact forced simple shear (a) full geometry and (b) center cross-section. (c) Resultant load-displacement curve from boundary conditions, where the blue region indicates full elastic response, purple the first initiation of plasticity, and red where the plastic region expands across entire sheared plane.

A fixed boundary condition was applied to the nodes on the bottom face of the geometry and the top face nodes were free to displace in-plane while a compressive Y displacement to 0.2 mm was applied. Plasticity models are path dependent leading to results that can be heavily affected by the number of individual steps at which calculations are completed. To ensure accuracy and prevent large deformations between individual steps, a total of 31 steps were used through the analysis.

The resultant stress and strain contour maps of the cross sections through the center of the sample viewed from the side and normal to the sheared plane, are shown in Figure 3.5 and Figure 3.6 respectively. Contours output at a displacement level of 0.16 mm. Figure 3.5(c) show the shear stress distribution to be concentrated at the corners, being more diffuse through the volume in a manner consistent with the two-fold symmetry of the sample geometry. While Figure 3.6(c) reveals a relatively uniform shear stress state within the plane. The normal components are negligible on the shear plane except for tension at the side edge and the concentrations of compression at the top and bottom corners. Qualitatively the contours show the stress state in the center of the sample to be close to a pure shear state. While the maximum of the normal stress components at the concentrations is larger than that of the shear components, it is important to remember that shear has a higher relative contribution to von-Mises stress (the yield criterion used in the model).

The strain contours show that the deformation is taking place almost entirely in shear along the plane as intended. In the normal strain contours, there are concentrations at the top and bottom corners, but they become near negligible at the center of the shear plane. The shear component of the strain shows concentrations at the side edges where the experimental displacement information is collected with DIC. These high concentrations are likely due to artifacts from the mesh, like element locking, causing a higher relative plastic strain accumulation that would cause complications when comparing to experimental results. Contour maps are useful in understanding the general distributions, but a closer look that quantifies these values is necessary to better evaluate the results.

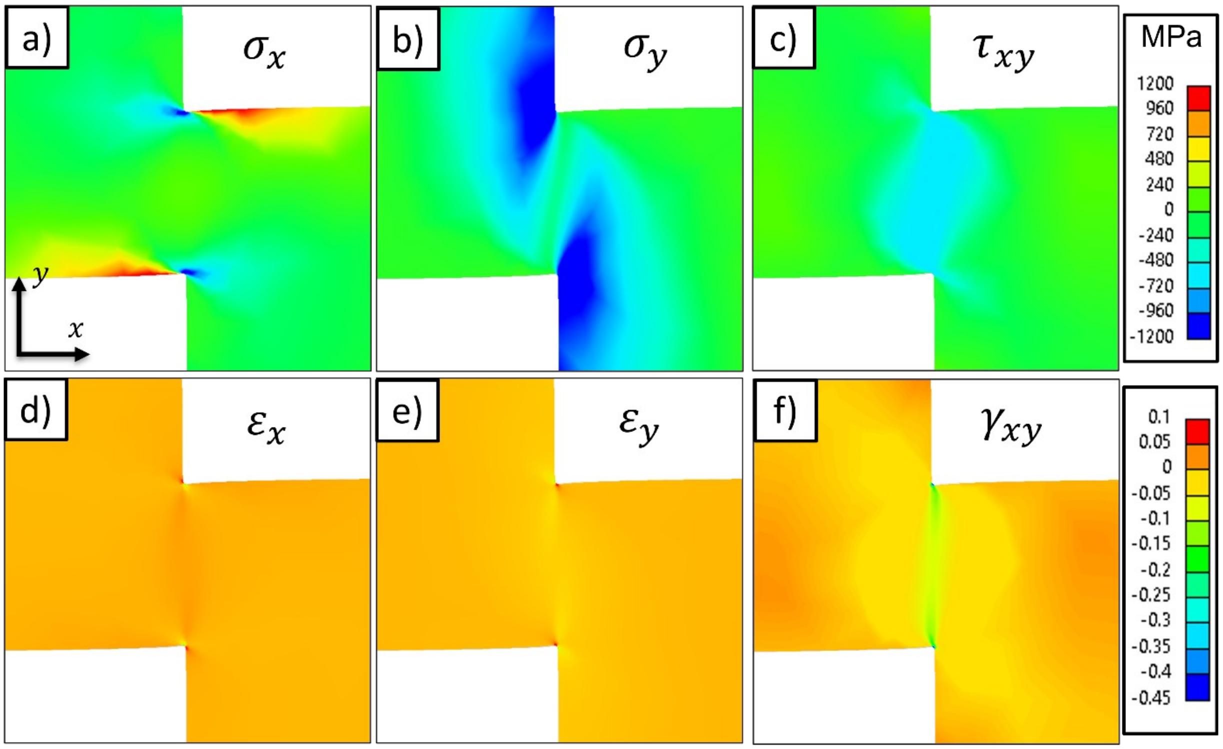

Figure 3.5: FE results cross-sectional view of shear plane contour maps for (a) σ_x, (b) σ_y, (c) τ_{xy} stress components and (d) ε_x, (e) ε_y and (f) γ_{xy} total strain components from a timestep with displacement ΔY=0.16 mm.

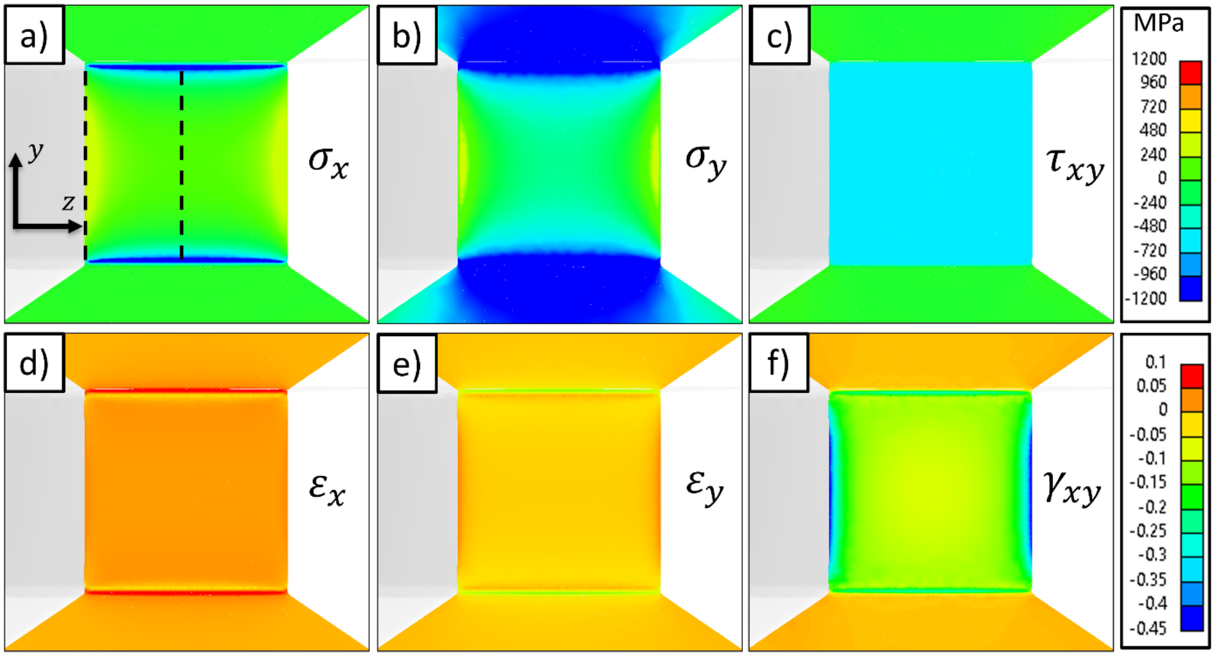

Figure 3.6: FE results cross-sectional view normal to sheared plane contour maps of (a) σ_x, (b) σ_y, (c) τ_{xy} stress components and (d) ε_x, (e) ε_y and (f) γ_{xy} total strain components from timestep with displacement ΔY=0.16 mm. Dashed lines in (a) indicate paths from which values are extracted in Figure 3.8 and Figure 3.10.

Figure 3.7 shows the evolution of the various components of stress averaged in the shear plane. The left axis (black) is stress in MPa and the calculated loading angle β is given on the right axis (blue). The colored regions pertain to fully elastic (blue), the beginning of localized plasticity (pink), and fully developed plasticity across the entire shear plane (red). This illustrates that there is a significant portion of the loading where yielding is inhomogeneous, which differs from uniaxial tension and compression tests where yielding occurs more homogeneously. There is a small positive normal stress σ_{xx} that causes a nonzero loading angle which ranges from a maximum of 6° in the elastic regime to a minimum 2° as plasticity develops in the sheared plane. This metric demonstrates that the stress state is very close to the pure Mode II shear attainable in biaxial load frames. As plasticity sets in, the magnitude of the average shear stress τ_{xy} continuously increases as the material strain hardens, while the average normal stress σ_{yy} peaks and then reduces significantly.

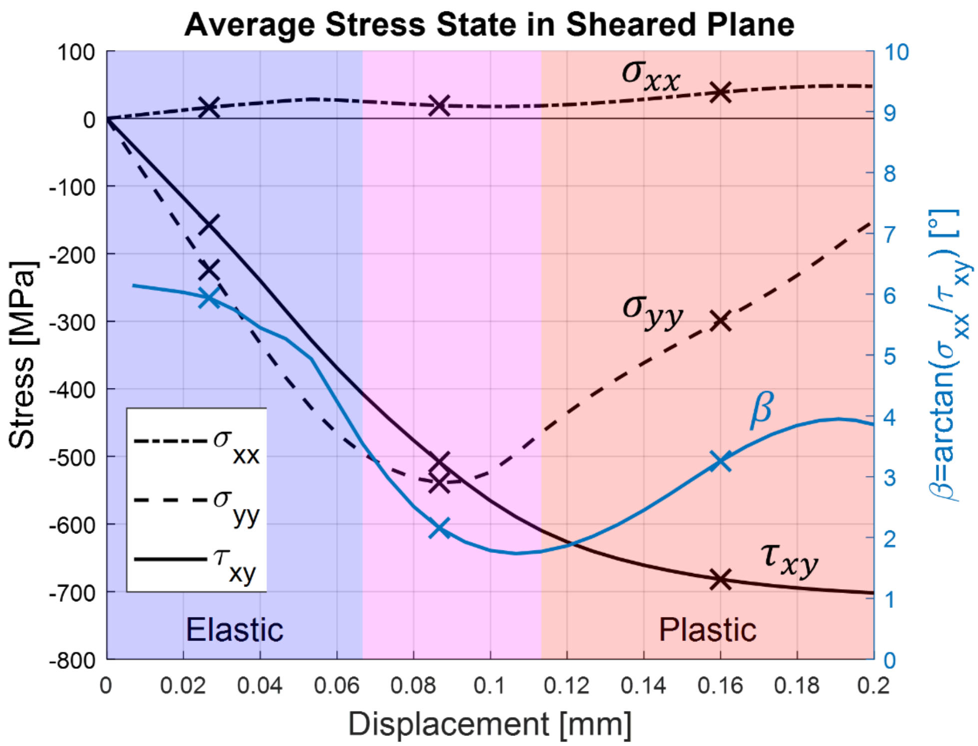

Figure 3.7: FE Results: Evolution of averaged stress components in the sheared plane on the left axis (black) and the loading angle β on the right axis (blue). The colored regions pertain to fully elastic (blue), the beginning of localized plasticity (pink), and fully developed plasticity across the entire shear plane (red). The X's denote the steps of the results displayed in Figure 3.8.

To better quantify the distribution of stresses and strains within the specimen, values were extracted along vertical paths both through the center of the sample and along the edge surface, where images were captured in the experiments (indicated by dashed lines in Figure 3.6(a)). The progression of the stress distribution is plotted in Figure 3.8(a-c) the colors of each displacement step correlate to those used in the regions in Figure 3.7 as noted by the x's. The solid lines are data from the center of the shear plane, which is closer to the average state, and the dashed lines are from the edge of the sample. Comparing the center values of the normal stresses with the surface values indicates a shift in the positive (tensile) direction. The concentration at the top and bottom corners of the sample is evidenced by the parabolic shape of the distributions. As plasticity sets in the normal stresses become more parabolic and the disparity from center to edge increases. The shear component becomes more homogenous along the length and from the edge to center, though there is still a noticeable concentration at the surface edge.

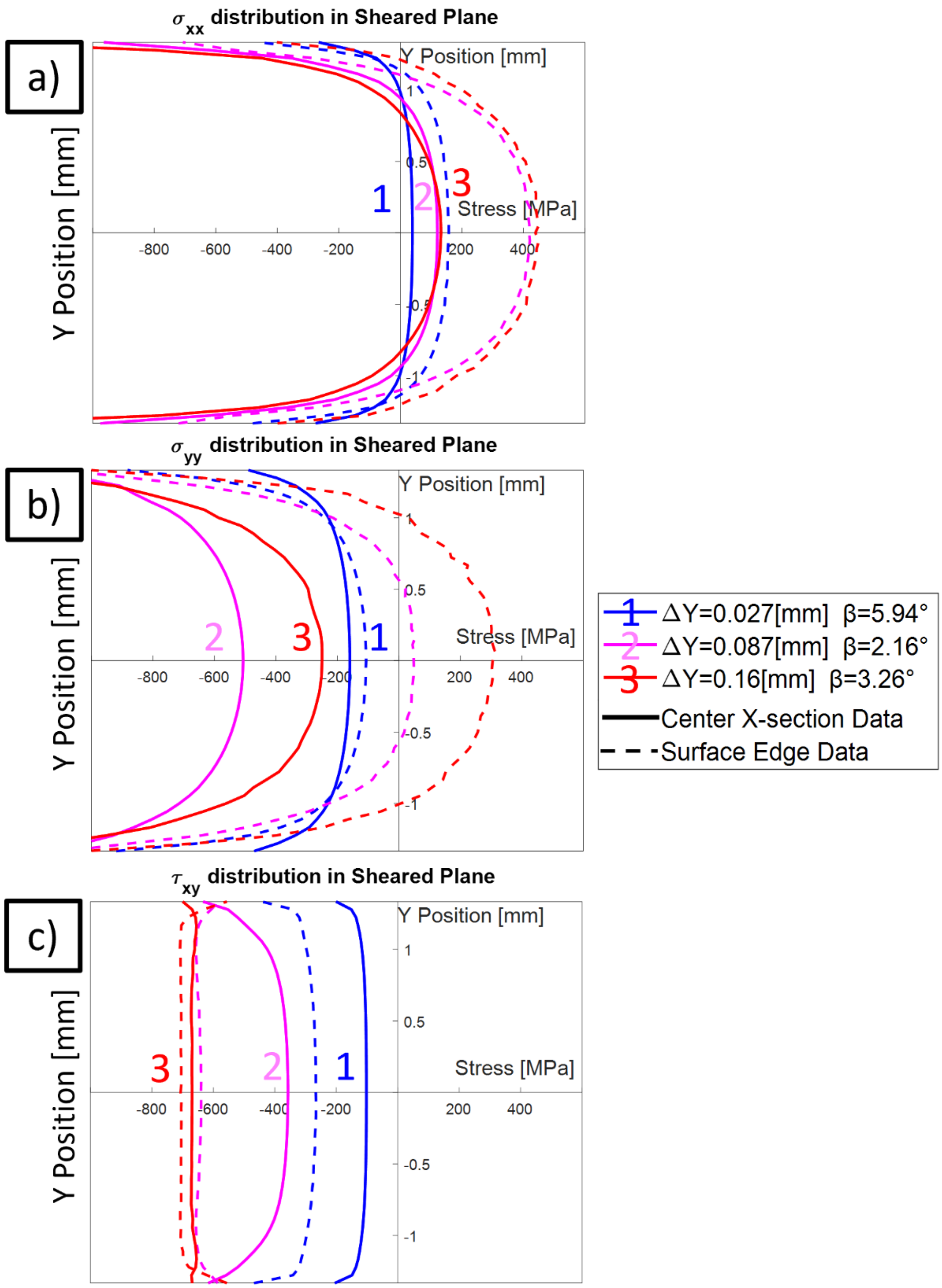

Figure 3.8: FE Results: Vertical distribution of (a) σ_{xx}, (b) σ_{yy}, and (c) τ_{xy} stress components through the center of the sample (solid) and the sample edge (dashed) locations indicated by dashed lines in Figure 3.6(a). Results from displacements of 0.027 mm (blue), 0.087 mm (pink), and 0.16 mm (red) denoted by the X's on the plot in Figure 3.7.

The evolution of the average strain components within the sheared plane and the ratio of normal strain to shear strain $|\varepsilon_{xx}/\gamma_{xy}|$ is shown in Figure 3.9. In a pure Mode II shear state this ratio is expected to be zero. The value starts at 0.22 in the elastic regime and reduces to 0.07 in the plastic regime. Like the stress components, as plasticity sets in the shear strain γ_{xy} continues to increase in magnitude while the normal strains level off. Beyond the 0.16 mm displacement the average normal strain components reduce to zero. The relative amount of elasticity in each strain component can be seen by the difference between the total and plastic strain lines in Figure 3.9, with shear retaining almost all the stored elastic strain as the plastic region fully develops.

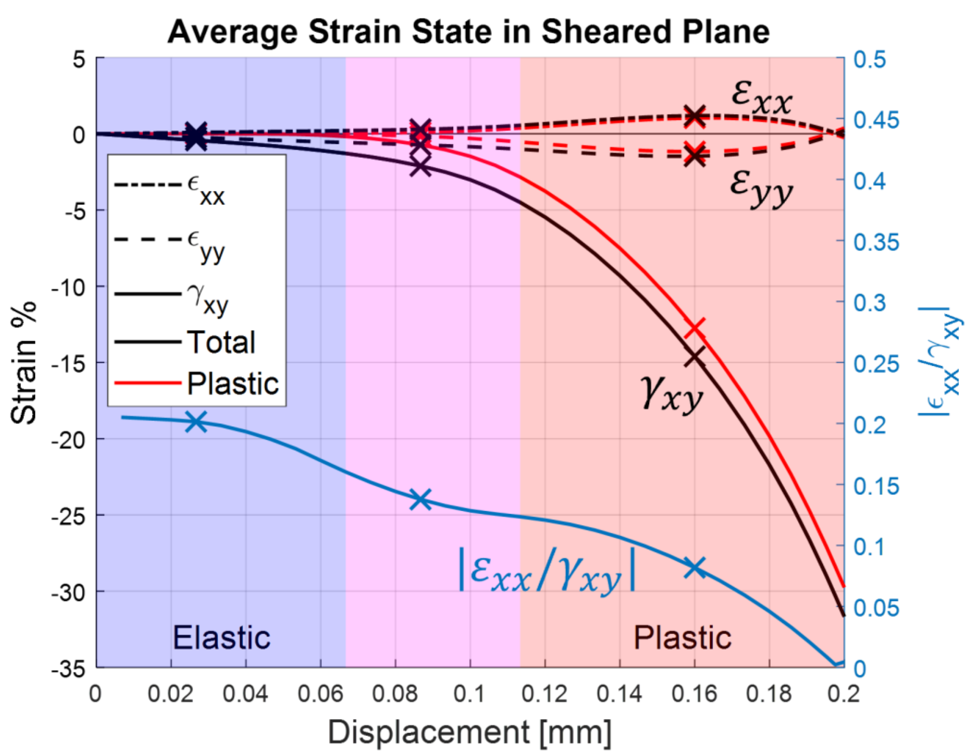

Figure 3.9: FE Results: Evolution of averaged total (black) and plastic (red) strain components in the sheared plane on the left axis and the resultant ratio of $|\varepsilon_{xx}/\varepsilon_{xy}|$ on the right axis (blue). The colored regions pertain to fully elastic (blue), the beginning of localized plasticity (pink), and fully developed plasticity across the entire shear plane (red). The X's denote the steps of the results displayed in Figure 3.10.

The development of the total strain distributions in Figure 3.10 show a similar parabolic shape to the stress, though the shear strain is much higher relative to the normal strains. All strain components, like the stress, shows concentrations at the top and bottom where plasticity first begins. Relevant to the experiment where only surface strain information is attainable; there is a very large disparity between shear strain in the center of the sample and at the surface. This disparity increases significantly as plasticity increases and, if true, would suggest that surface DIC would not be usable in the CFSS tests.

To consider whether the use of surface DIC is relevant it is important to note the strain hardening model was defined to a true tensile plastic strain level of 8%, beyond which the simulation will extrapolate from the last linear segment (slope of ~0 MPa). This near zero tangent modulus causes perfectly plastic behavior and will lead to the development of large plastic strains with continued loading. Due to significant stress concentration, the model definition is locally surpassed on the edge surface as quickly as the plastic zone reaches the center of the sample. The result of this phenomenon is the development of the exceedingly high surface strains that are likely not representative of the true physical response. Implementation of a damage model that captures material softening behavior that occurs beyond necking, which is not included in the strain hardening model, would help address this issue. For the sake of this study the average strain state across the sheared plane will be used to evaluate the overall stress-strain response.

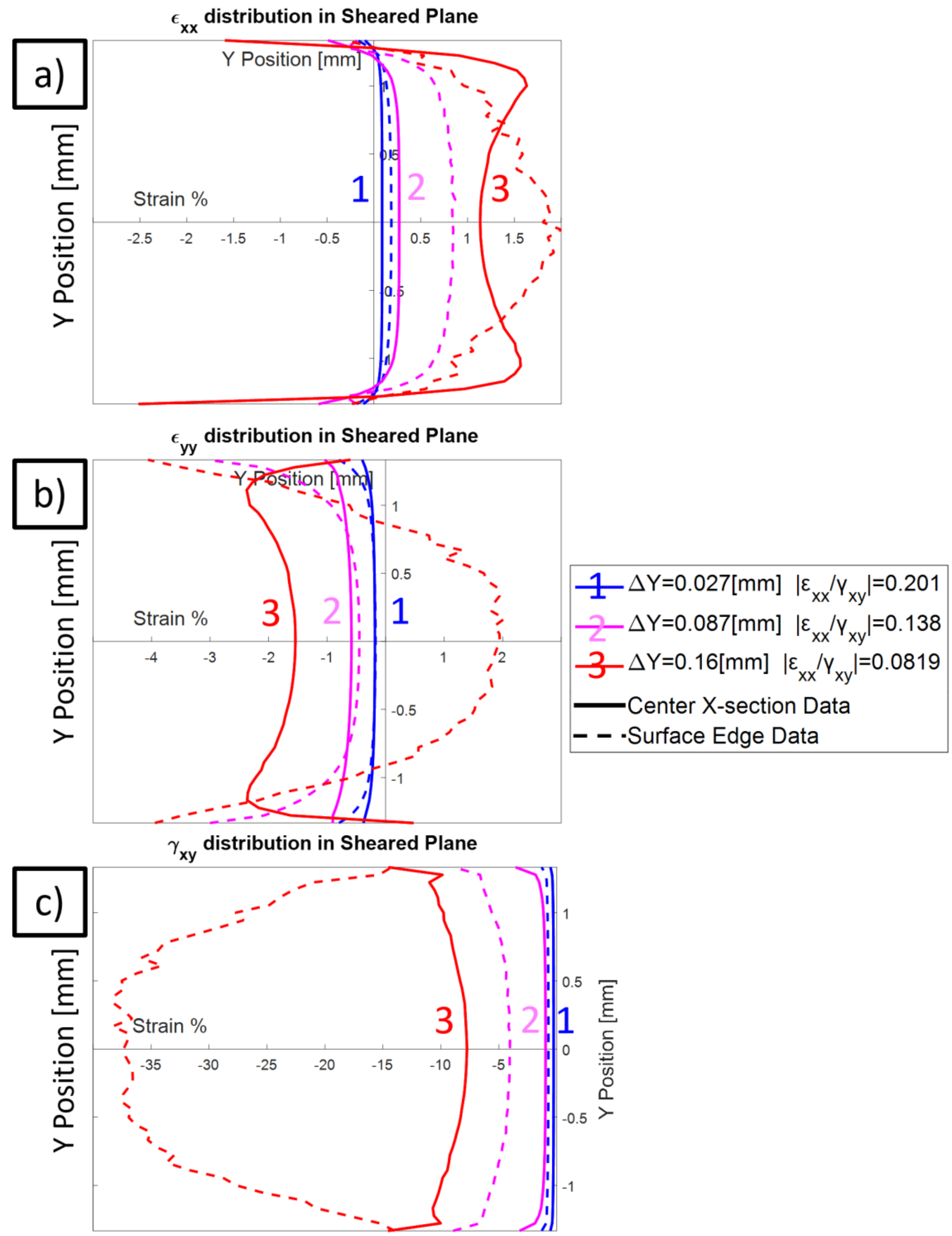

Figure 3.10: FE Results: Vertical distribution of (a) ε_{xx}, (b) ε_{yy}, and (c) γ_{xy} total strain components through the center of the sample (solid) and the sample edge (dashed) locations indicated by dashed lines in Figure 3.6(a). Results from displacements of 0.027 mm (blue), 0.087 mm (pink), and 0.16 mm (red) denoted by the X's on the plot in Figure 3.9.

Constructing an average stress – average strain curve (Figure 3.11) enables a calculation of yield strength the same as would be done for an experimental curve. Using the typical 0.2% strain offset and measured shear modulus suggests a yield strength of 420 MPa. This is well below the shear yield strength as measured from the wrought tensile test and defined in the FE model as 610 MPa. This disparity is due to the localized nature of yielding within the CFSS geometry; the corners yield well before the rest of the sheared region (as can be seen by the evolution of stresses in Figure 3.8c) and that leads to a deviation from a linear stress-strain response well before macroscopic yielding. The known yield strength aligns well with the start of the red region which correlates with macroscopic yielding. Back calculating from the known true yield strength of the wrought material gives a strain offset of 2.8%, which will be utilized with experimental curves to evaluate yield strengths. This offset value is reliant on the assumption of a consistent yielding and strain hardening behavior and would need to be reevaluated for other materials.

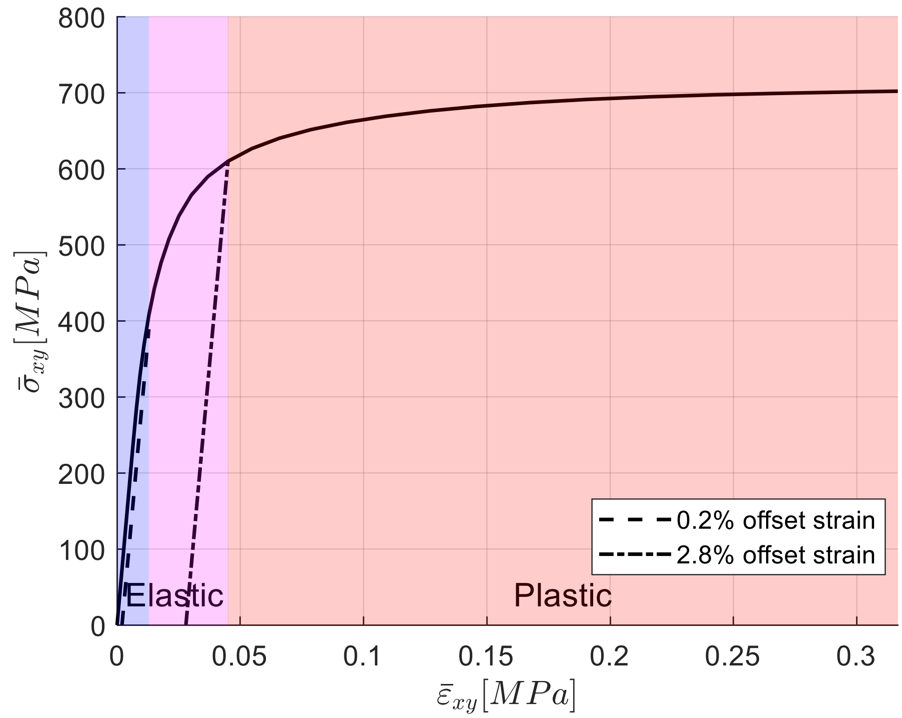

Figure 3.11: FE Results: Average stress - average strain curve for a simulation using known wrought properties. A 0.2% strain offset typically used to calculate yield strength under predicts the yield strength (420 MPa). The true yield strength (610 MPa) is achieved using an offset of 2.8% strain. The colored regions pertain to fully elastic (blue), the beginning of localized plasticity (pink), and fully developed plasticity across the entire shear plane (red).

3.3. Implementation of Digital Image Correlation Analysis

The unique geometry of these samples with non-planar surfaces produces challenges for DIC imaging and due to the inherent high localization of the shear, the acquisition of high-resolution images and application of a reliable speckle is crucial to producing reliable DIC correlation datasets. Samples were machined from the same rolled bar of grade 5 Ti64 used to define the FE model, dimensions were made in accordance with Grey and Vecchio [7]. A speckle pattern was applied using a mixture of black polyester powder (printer toner) and white acrylic paint via airbrush. The resulting speckles are on average 16 μm in diameter and the density of speckling can be controlled by the amount of powder used. The imaging setup (3x telecentric lens on a PixelLink camera) had a pixel size of 1.5 μm, with an optimal speckle size being 4 pixels (6 μm) at 60%

density, leaving opportunity for further optimization of the speckle application [9]. Prepared samples were compressed using a servo-hydraulic MTS load frame at a displacement rate of 0.0005 mm/s with images captured at 1 second intervals.

The captured experimental images were processed using the software VIC2D (Correlated Solutions) to produce surface displacement data that is used in the analysis that follows. The strain contours as shown Figure 3.12, indicate a similar response to that predicted by the FEA (Figure 3.5) with a concentration of higher shear at the top left and bottom right corners. There is less localized strain in the center where the concentration also switches sides favoring the side of the shear plane with the free surface (top left and bottom right in Figure 3.12) like seen in FEA contours.

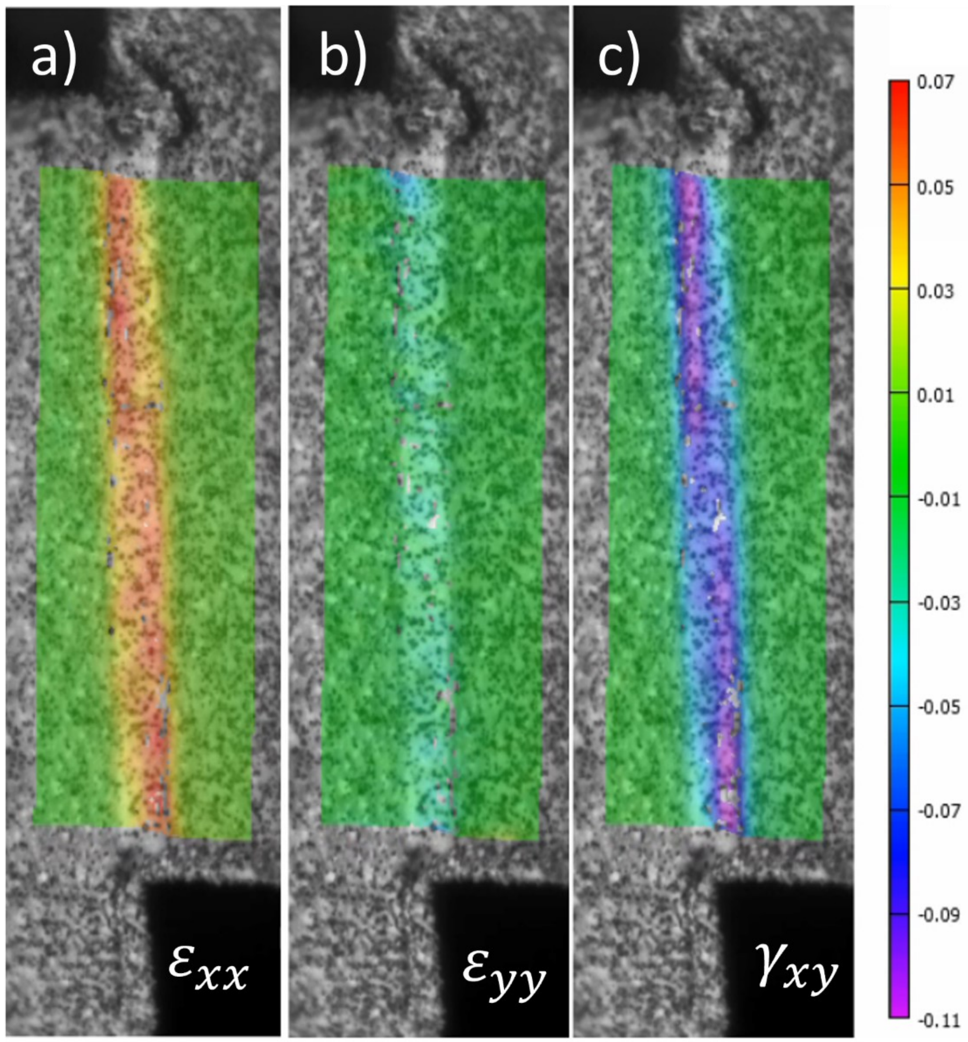

Figure 3.12: VIC2D processed DIC contour maps of (a) ε_{xx}, (b) ε_{yy}, and (c) γ_{xy} strain components from a loaded sample with estimated average strain of 10%.

With the capability to produce a stress-strain curve being the primary objective, a representative strain value is needed for each image's displacements. Unlike for uniaxial compression or tension experiments, a simply defined area average is not an accurate description because it does not capture the inherent localization of the strain. Another metric for interpreting the deformation information must be used. Averaging the strain along the shear plane from corner to corner is a straightforward method, but as seen in the FEA and DIC maps the deformation is not limited to an idealized plane. To calculate a more accurate representative strain, an automated method for identifying the shear zone and extracting the necessary displacement information was established. The components of engineering strain were calculated using displacement gradients as described by:

$$\varepsilon_{xx} = \frac{\partial u}{\partial X} \tag{3.3}$$

$$\varepsilon_{xx} = \frac{\partial v}{\partial Y} \tag{3.4}$$

$$\varepsilon_{xy} = \frac{1}{2}\left(\frac{\partial u}{\partial Y} + \frac{\partial v}{\partial X}\right) \tag{3.5}$$

Figure 3.13(a) and (d) show an example of the horizontal and vertical displacement distributions generated from an image of a sample with approximately 5% shear strain. Figure 3.13(b) gives the vertical displacements v along a horizontal line across the center of the sample. The slopes $\frac{\partial v}{\partial X}$ is a component of shear strain. There is a steep gradient in the center where the strain is localized. A similar localization of normal strain is evident in Figure 3.13(e). The plots in Figure 3.13(c) and (f), corresponding to $\frac{\partial u}{\partial Y}$ and $\frac{\partial v}{\partial Y}$, show a linear behavior with much smaller gradients. From these plots it can be determined that the shear zone is best bounded horizontally by the inflection points seen in Figure 3.13(b) and (e). Each term of the strain will be approximated by averaging the gradient of the displacement data within these bounds. A Matlab program was produced to automate the process by fitting a plane to the identified shear region as well as cleaning up any erroneously tracked points to improve reliability.

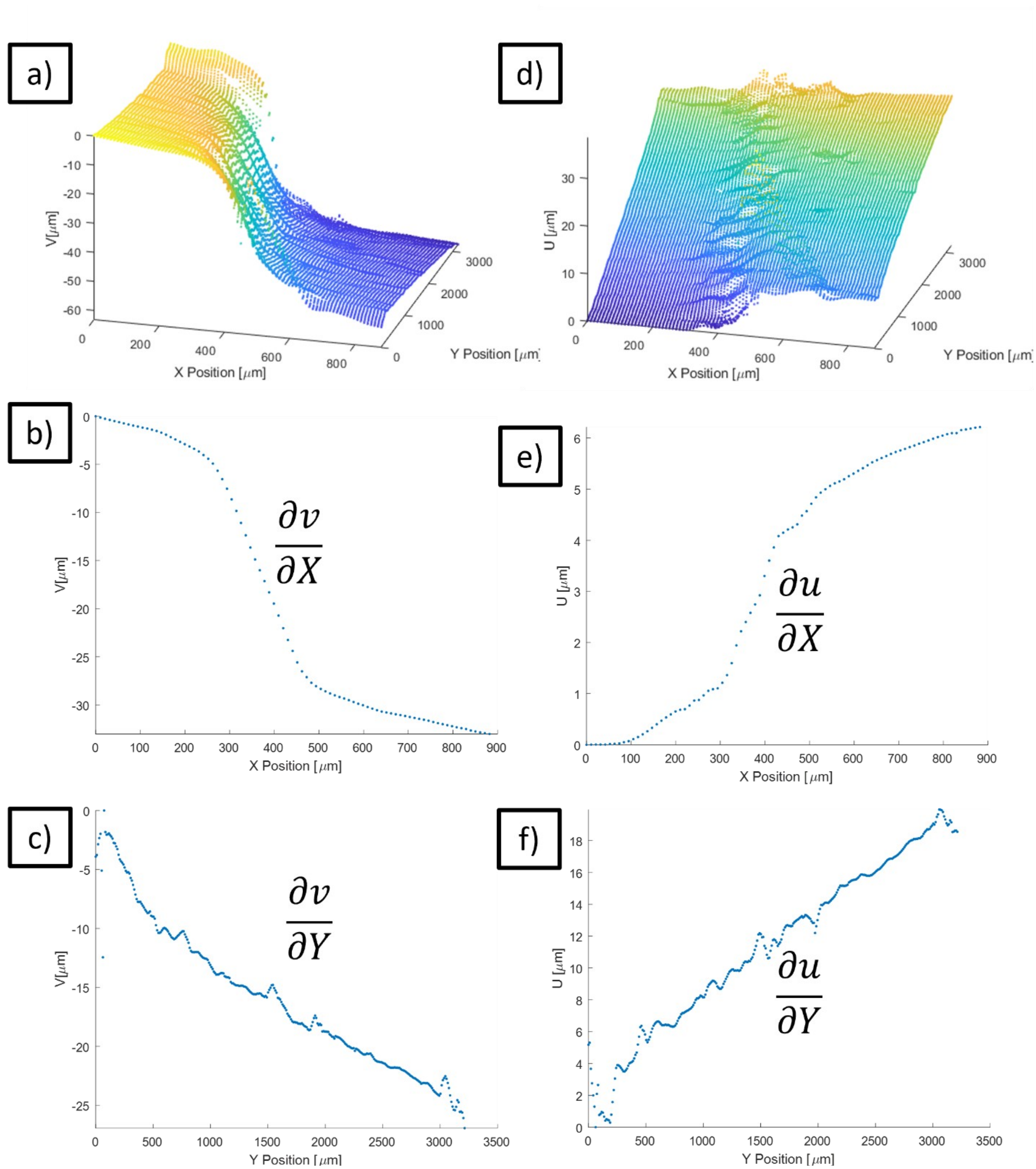

Figure 3.13: Displacement fields from an image with estimated shear strain of 5%. (a-c) vertical displacement v with x and y. (d-f) horizontal displacement u in x and y. (b) and (e) traces taken through center of data at Y=1750 μm. (c) and (f) traces taken through center of data at X=450 μm. Localization of strain is evident by steep gradients in the center of (b) and (e).

In DIC analysis a larger subset size will increase the reliability of correlation as a larger number of pixels are used in the correlation. However excessively large subset size will not be able to capture the underlying deformations [10], which is of prime importance to the localized strain in these tests. The size of the subset or the step between tracking points do not have a strong effect on the calculated displacement gradients so long as they are sufficiently small in relation to the shear localization. A subset size of 90 μm was used in the analysis presented. The experimental results had a shear band width of 225-300 μm, with a step size of 10.5 μm (7 pixels) yielding 20-30 correlated points across. A decrease in the step size would have increased the number of correlated points within the sheared band and the spatial resolution, however was not needed for the analysis.

3.4. Results and Discussion

3.4.1. Implementation with Wrought Ti-6Al-4V

The efficacy of the application of the DIC methodology was evaluated experimentally. Five CFSS samples were machined from the same rolled bar of grade 5 Ti64 used to define the FE model, dimensions were made in accordance with Grey and Vecchio [7]. Speckled samples were compressed using a servo-hydraulic MTS load frame at a displacement rate of 0.0005 mm/s with images captured at 1 second intervals.

Using the localized gradient fit described above engineering strain values were calculated for each image in a CFSS experiment, and stress was calculated from the measured load over the gage area being sheared. Comparing this with a simple average of VIC2D post-processed strains along the idealized shear plane as shown in Figure 3.14, revealed that the simple average method reports higher strain values than the localized fit. The localized fit yields a shear modulus of 38 GPa while the simple average yields an artificially low modulus of 14 GPa; the expected value is 37 GPa. Both show a linear relation between the displacement and calculated strain that shifts to a higher slope once plasticity sets in around displacement of 0.14 mm. The simple average begins to break down after the peak stress when the sample begins to fail around 0.24 mm of displacement, but the localized fit method is still able to provide a reasonable measurement to a higher level of deformation. This all demonstrates the robustness of the localized fit method over a simple average.

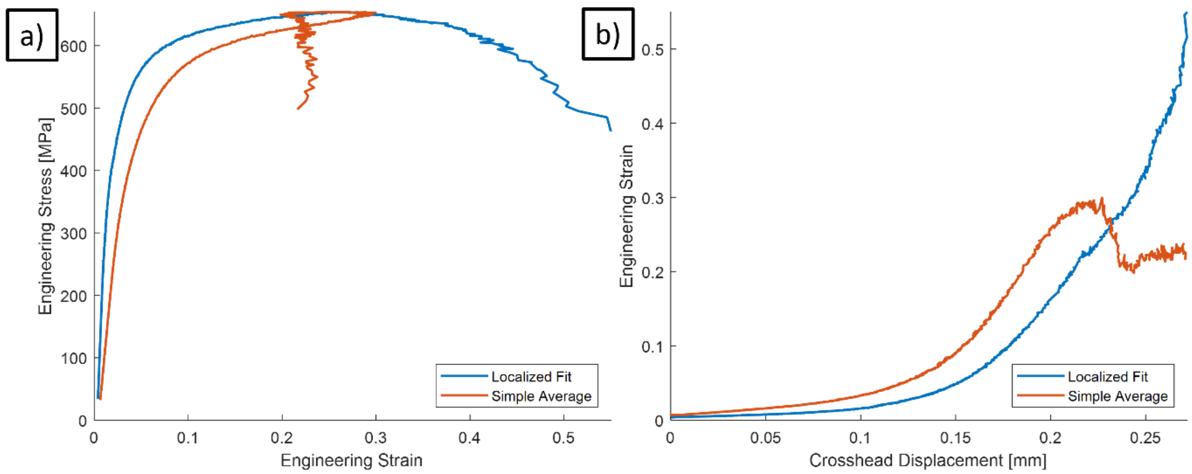

Figure 3.14: Experimental results (a) Stress-strain and (b) displacement-strain curves from localized DIC fit and simple average along shear plane of VIC2D post processed strains. The reliability of the localized method is demonstrated both in the accuracy of the elastic response and the production of strain measures even as the simple average breaks down.

The localized method is also not as negatively affected by poor tracking at high strains in the sheared area; it can approximate the displacement gradients from the points on either side of the shear plane even if there are some missing data points in the very center. In the post-processing used in DIC software like VIC2D the strains are calculated by fitting displacement gradients to neighboring points within a defined radius. This leads to it being much more susceptible to untracked points when compared to the localized method that uses all the points within the identified area. At high strains the tracking of subsets begins to break down as the speckle pattern is deformed to such an extent that it is not able to meet the correlation quality requirements when compared with the undeformed image. This can be addressed by using incremental correlation, where each immediately preceding image is used as the reference instead of the undeformed image.

However, any errors in the correlation quickly compound and can lead to false strains, so it was not implemented in this study.

The calculated strain state within the shear zone along with the ratio of normal strain to shear strain $\varepsilon_{xx}/\gamma_{xy}$ (Figure 3.15) exhibited a similar evolution to that seen in the FE simulation (Figure 3.9). There are again two sections in the displacement-strain curves that correlate to the elastic and plastic regimes. In contrast to the averaged FE results however, each component of the strain begins to increase in amount at a higher rate after yielding. The ratio of normal strain over the shear strain ($\varepsilon_{xx}/\gamma_{xy}$) ranges from a maximum of 0.5 just before yielding and decreases of 0.25 at failure, in contrast with the range suggested by FEA of 0.22 to 0.07. It is worth noting that the FE values were averaged across the shear plane as opposed to the surface in the DIC.

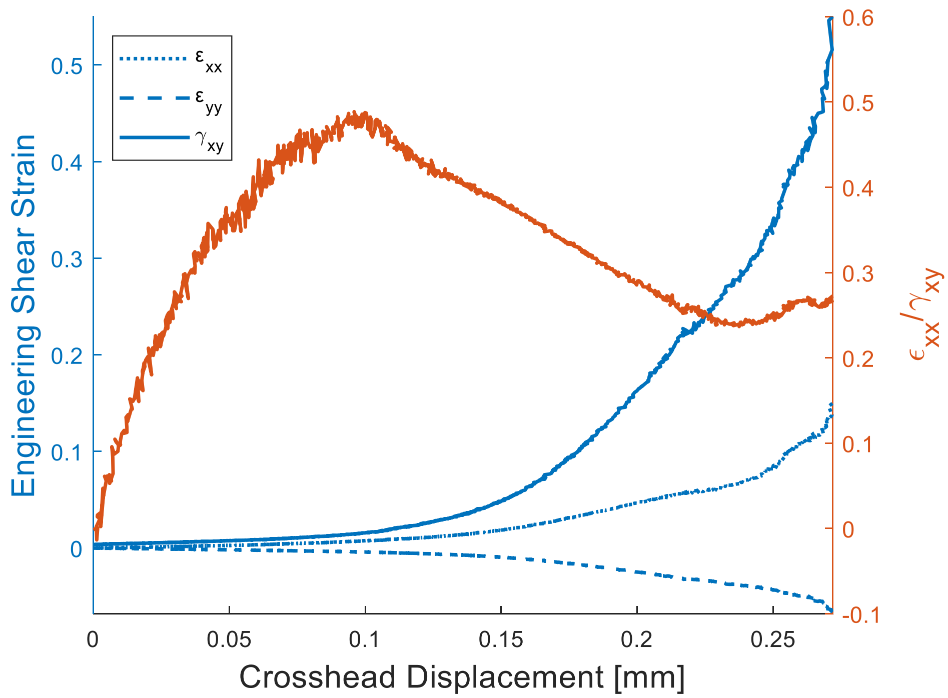

Figure 3.15: Development of normal, transverse, and shear DIC strains (left blue axis) and calculated ratio of $\varepsilon_{xx}/\gamma_{xy}$ (right red axis) as a function of crosshead displacement.

The repeatability between individual samples was investigated; the results from five different tests are presented in Figure 3.16 and were taken to failure. The curves all have the same general shape, but there is a noticeable variability in the load-displacement response in Figure 3.16(a). This could be due to a variation in the machined geometry, though it is difficult to confirm from the fractured samples. From the plot in Figure 3.16(b) there is good agreement in the elastic regime, but as yielding begins there is a spread in strain values and all measured values are lower than the FE simulation predicted. When the results are processed into stress-strain curves the agreement is much improved with only small variations in the initial yielding behavior.

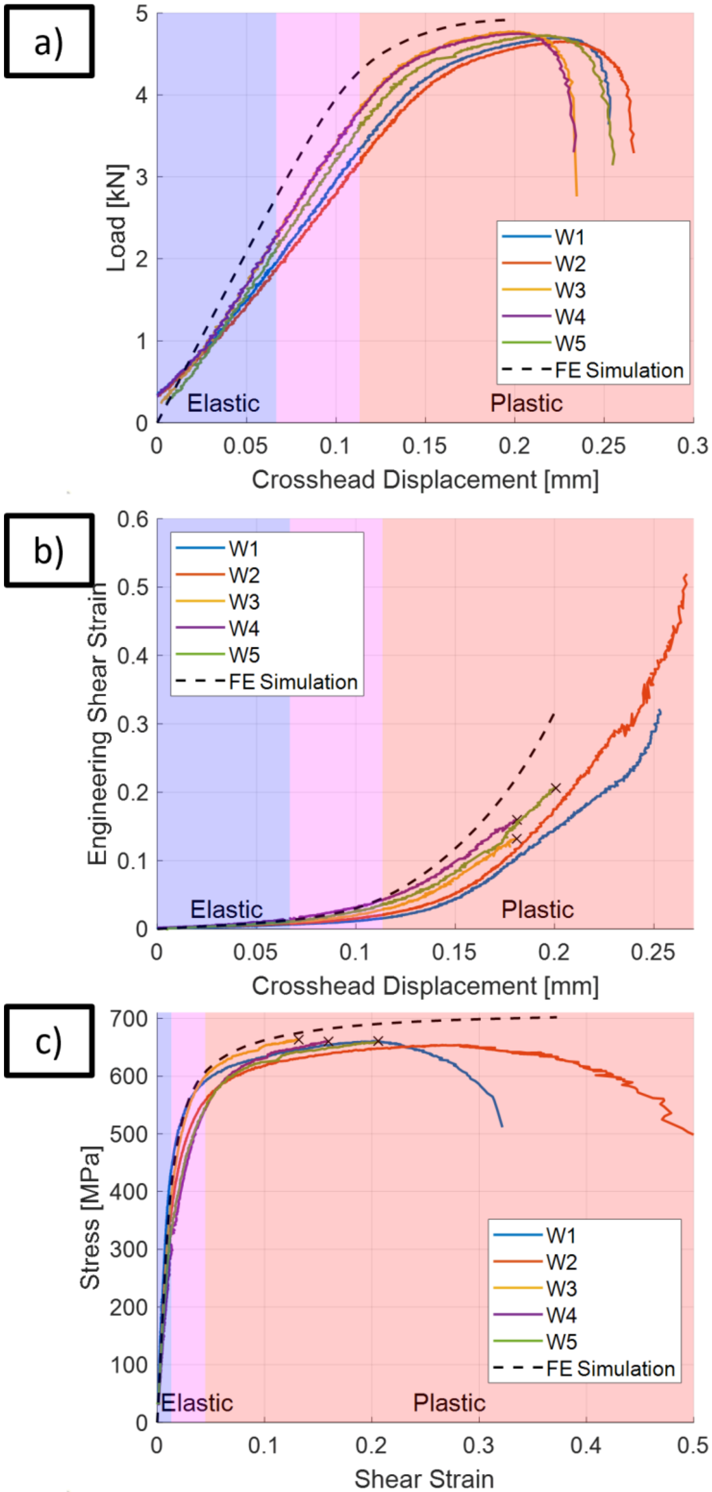

Figure 3.16: (a) Measured load-displacement, (b) calculated (localized fit) strain-displacement and (c) resultant stress-strain curves of all grade 5 Ti-6Al-4V samples along with FE simulation predicted response. Curves that end with an X indicate that paint unadhered from sample surface.

While fracture was not of interest in this study it is worth noting that there was a noticeable variation in the displacement and calculated strain to failure. The samples that have curves ending in X's (W3, W4, W5) signify that the paint unadhered to the sample surface at high strains. This was likely due to the samples being tested a few days after being speckled, allowing more time for the acrylic paint to cure, forming a more coherent film than those tested immediately after painting. This caused the film of paint to pull away from the surface prematurely as the film was stronger than the adherence to the sample surface. Further investigation would be warranted to determine the efficacy of the CFSS for evaluating fracture behavior.

The elastic response between three of the samples was evaluated by unloading within the plastic regime of the curve as shown in Figure 3.17. This unloading in the plastic regime was guided by the simulation observation of the elastic strain being more concentrated in the shear component after yielding (Figure 3.9). There is much better agreement with the load-displacement stiffness than seen in the initial loading, likely aided by the samples being better settled between the platens in addition to the elastic effect. The resultant shear moduli 39.2$\pm$0.4 GPa are close to the expected value of 36.7 GPa, values are shown in Table 3.2. The modulus as used in the FE simulation was estimated from the measured tensile properties using the approximation of $G = \frac{E}{2(1+\nu)}$.

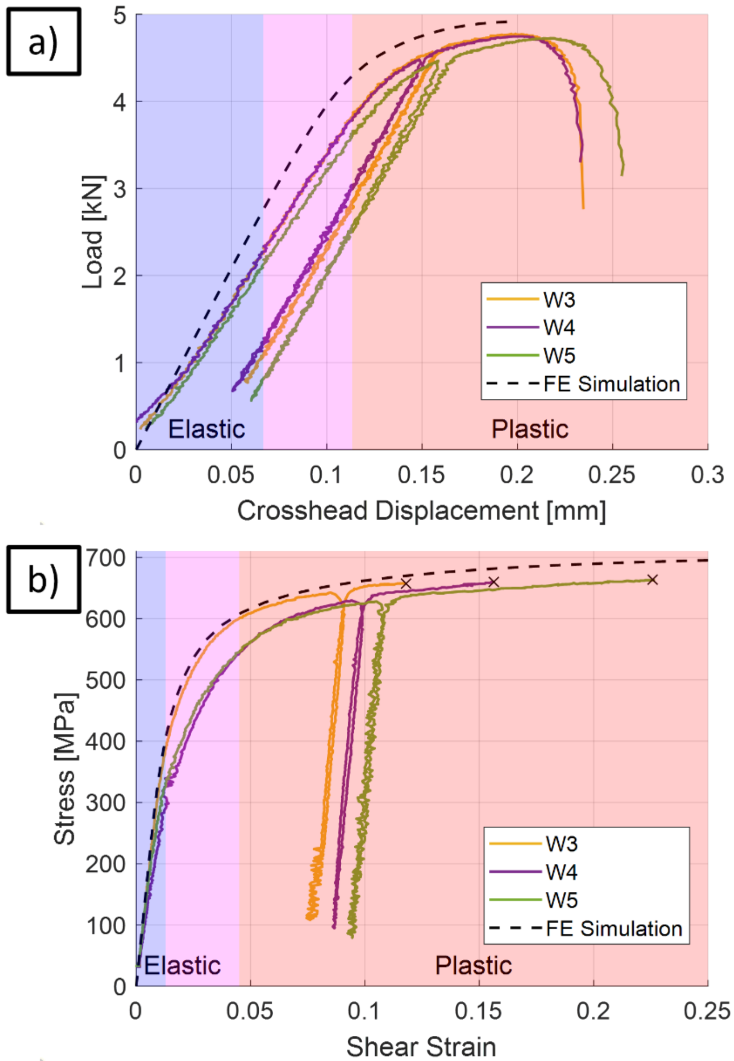

Figure 3.17: (a) Measured load-displacement and (b) calculated stress-strain curves for specimens unloaded within the plastic zone along with FE simulation predicted response.

Table 3.2: Calculated load-displacement stiffness and shear moduli from unloading in plastic regime from curves shown in Figure 3.17.

Sample	Load-Displacement Stiffness [kN/mm]	G [GPa]
W3	38.0	39.1
W4	38.1	39.7
W5	38.8	38.9
FE Simulation	44.4	36.7

3.4.2. Revisiting LPBF Ti-6Al-4V Yield Surface

The lessons learned regarding the yielding behavior of the CFSS geometry for wrought Ti-6Al-4V samples was used to revisit the initial yield surface study of LPBF Ti-6Al-4V. The AM shear results were reevaluated using the 2.8% strain offset to calculate the yield strengths as suggested by the results of, and adjustments required for the wrought CFSS samples. This method increased the apparent yield strength from 410 MPa to 560 MPa. As plotted against the yield surface in Figure 3.18 this method produces values that fall on the Liu yield surface and are much more in line with the measured tension and compression yield strengths.

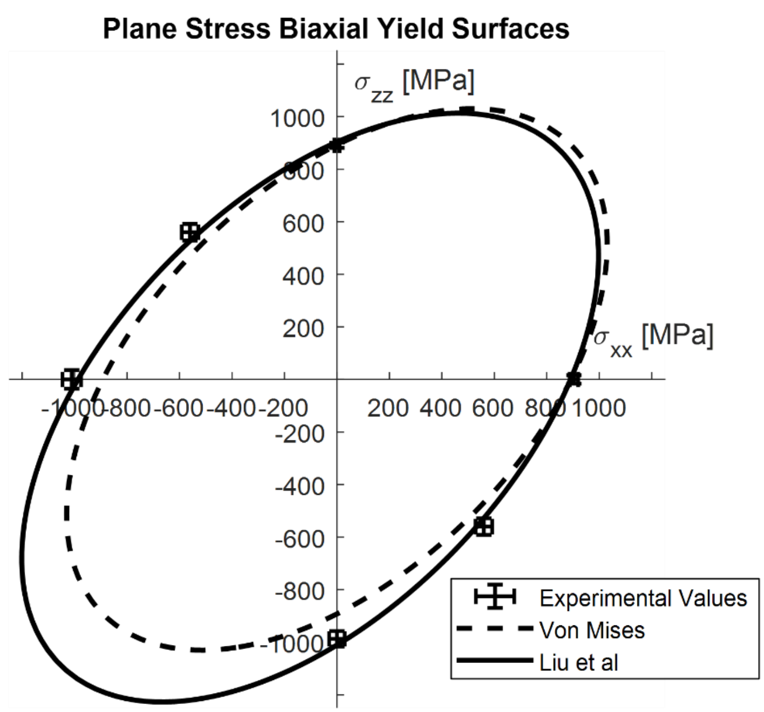

Figure 3.18: Revised LPBF Ti-6Al-4V plane stress biaxial yield surface from Figure 2.12 using the 2.8% strain offset suggested by the investigation of wrought samples to calculate the shear yield points.

3.5. Chapter Summary

The stress and strain states in a CFSS specimen were evaluated using an elastic-plastic FE model. The FE model indicated that the stress state is close to the intended pure shear with the loading angle β reaching a maximum value of 6° in the elastic regime, that reduces to 2° as yielding occurs. The model confirms that the plasticity is predominantly shear in character within the intended plane. An experimental method for implementing DIC, automatically identifying the sheared area, and calculating resultant surface strains was developed. The experimental data transitioned towards a more pure-shear state after yielding as was seen in the model. Using the calculated strains combined with measured load data, stress-strain plots were produced and reliable measures of shear moduli for wrought CFSS samples were made by unloading within the plastic regime. It was determined that using the conventional 0.2% strain offset for calculating yield points significantly underestimate the yield strength due to the localized nature of yielding in the geometry causing a premature deviation from linearity. Back calculating from the known yield strength in the simulation produced a strain offset of 2.8% to provide for a more accurate calculation of the yield. This was then utilized with the experimental data from the previous chapter to produce measures of shear yield strength that aligned remarkably well with the yield surface composed from the tension and compression results.

3.6. References for Chapter 3

1. Mohr, D. and M. Oswald, *A New Experimental Technique for the Multi-axial Testing of Advanced High Strength Steel Sheets.* Experimental Mechanics, 2007. **48**(1): p. 65-77.
2. Peirs, J., et al., *The use of hat-shaped specimens to study the high strain rate shear behaviour of Ti–6Al–4V.* International Journal of Impact Engineering, 2010. **37**(6): p. 703-714.
3. Meyers, M.A. and S. Manwaring, *Critical adiabatic shear strength of low alloyed steel under compressive loading*, in *Metallurgical applications of shock-wave and high-strain-rate phenomena*, L.E. Murr, K.P. Staudhammer, and M.A. Meyers, Editors. 1986: New York. p. 657-674.
4. Rittel, D., S. Lee, and G. Ravichandran, *A shear-compression specimen for large strain testing.* Experimental Mechanics, 2002. **42**(1): p. 58-64.
5. Bronkhorst, C.A., et al., *An experimental and numerical study of the localization behavior of tantalum and stainless steel.* International Journal of Plasticity, 2006. **22**(7): p. 1304-1335.
6. Xue, Q., et al., *Influence of shock prestraining on the formation of shear localization in 304 stainless steel.* Metallurgical and Materials Transactions A, 2005. **36**(6): p. 1471-1486.
7. Gray, G.T., K.S. Vecchio, and V. Livescu, *Compact forced simple-shear sample for studying shear localization in materials.* Acta Materialia, 2016. **103**: p. 12-22.
8. Cady, C.M., et al., *The Shear Response of Beryllium as a Function of Temperature and Strain Rate.* EPJ Web of Conferences, 2018. **183**: p. 02017.
9. Wang, Y., et al., *Optimal Aperture and Digital Speckle Optimization in Digital Image Correlation.* Experimental Mechanics, 2021. **61**(4): p. 677-684.
10. Pan, B., et al., *Study on subset size selection in digital image correlation for speckle patterns.* Opt Express, 2008. **16**(10): p. 7037-48.

CHAPTER 4: EFFECT OF TEMPERATURE IN THERMO-HYDROGEN REFINEMENT OF MICROSTURE WITH LPBF Ti-6Al-4V

4.1. Introduction

Metal additive manufacturing (AM) has revolutionized manufacturing over the past few decades with the ability to fabricate complex components previously unimaginable with conventional subtractive manufacturing techniques. The thermal cycling and rapid cooling rates often result in inhomogeneous microstructures and formation of non-equilibrium phases [1]. While metal AM has its many benefits, especially its ability to manufacture complex geometries like metamaterials [2], it is also prone to porosity in the form of lack of fusion (LOF) and keyhole pores [3, 4], and to large residual stresses [5]. These undesired features can be mitigated through the optimization of manufacturing processing parameters with varying levels of success and repeatability [6-10], but there is still a strong demand for post-processing heat treatments to achieve the requisite material properties [11].

Of particular interest to this study the rapid cooling rates in AM often result in as-built Ti-6Al-4V with non-ideal phases and structures, such as the strong but brittle α' martensitic phase [1]. Because of this and porosity, as-built DMLS Ti-6Al-4V components often fall short of meeting the requisite level of ductility and fatigue performance. Standard post-processing heat treatments such as stress relief and HIP are often implemented to mitigate deleterious microstructural features. HIP operates by imposing high isostatic pressures with inert gas along with elevated temperatures to promote closure of pores through a combination of diffusion, plastic flow and creep [14]. The elevated temperatures (>950 °C) used in HIP allows for decomposition of retained martensite and coarsens the fine lathe structure to produce properties and microstructures that are close to wrought Ti-6Al-4V [11, 15]. HIP has been shown to transform as-built materials, imbuing them with properties that meet Grade 5 Ti-6Al-4V requirements as outlined in ASTM B348 standard [16-19]. However, HIP involves the use of specialized furnaces that are sizeable, expensive, and not as accessible as conventional furnaces.

Hydrogen sintering and phase transformation (HSPT), a low-cost process developed for powder metallurgy, has demonstrated full material densification along with microstructural control without the need of external applied pressures. This allows for post-print heat treatments to be carried out in a standard vacuum furnace [20, 21]. The HSPT processing of Ti-6Al-4V, summarized in Figure 4.1, employs hydrogen as a temporary alloying element in the Ti matrix, which allows for: (i) an increase in Ti self-diffusivity that enables pore closures without applied pressure and (ii) a novel phase transformation from typical $\beta \rightarrow \alpha + \beta + \alpha_2$ to $\beta \rightarrow \beta + \alpha_2$ that facilitates the formation of fine microstructures through homogenous α_2 (Ti_3Al) nucleation within the β grains [22].

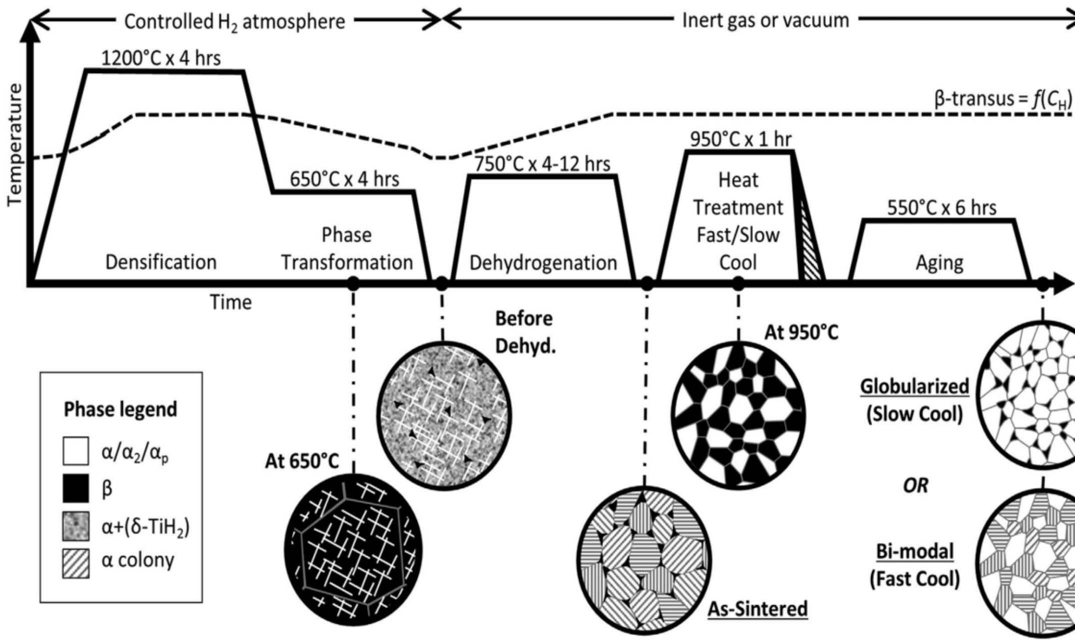

Figure 4.1: Hydrogen sintering and phase transformation thermal processing steps illustrating evolution of phases and microstructure of Ti-6Al-4V. Adapted from [20]

These two effects are accomplished in the first two heating steps within a hydrogen environment; densification happens above the β transus and the temperature is then reduced to 650 °C where the $\beta \rightarrow \beta + \alpha_2$ phase transformation takes place. As the material is cooled to room temperature the deleterious hydride δ (TiH_2) precipitates in the microstructure along with the α, these steps are described in the phase diagram (Figure 4.2). The material undergoes a dehydrogenation step to bring the hydrogen content below the ASTM limit of 150 ppm, removing any possible δ phase [23]. With additional heating steps the refined structure can be converted to a globularized or bimodal structure enabling a reproduction of wrought-like microstructures. The process is especially attractive because it can be performed in a commonly accessible vacuum furnace without needing applied deformation at any point [20]. Applying the first three steps of HSPT (densification, phase transformation and dehydrogenation) in the place of a post heat treatment is referred to as thermo-hydrogen refinement of microstructure (THRM) [24], and has been demonstrated to produce material with tensile properties similar to wrought from as-built Ti-6Al-4V [25].

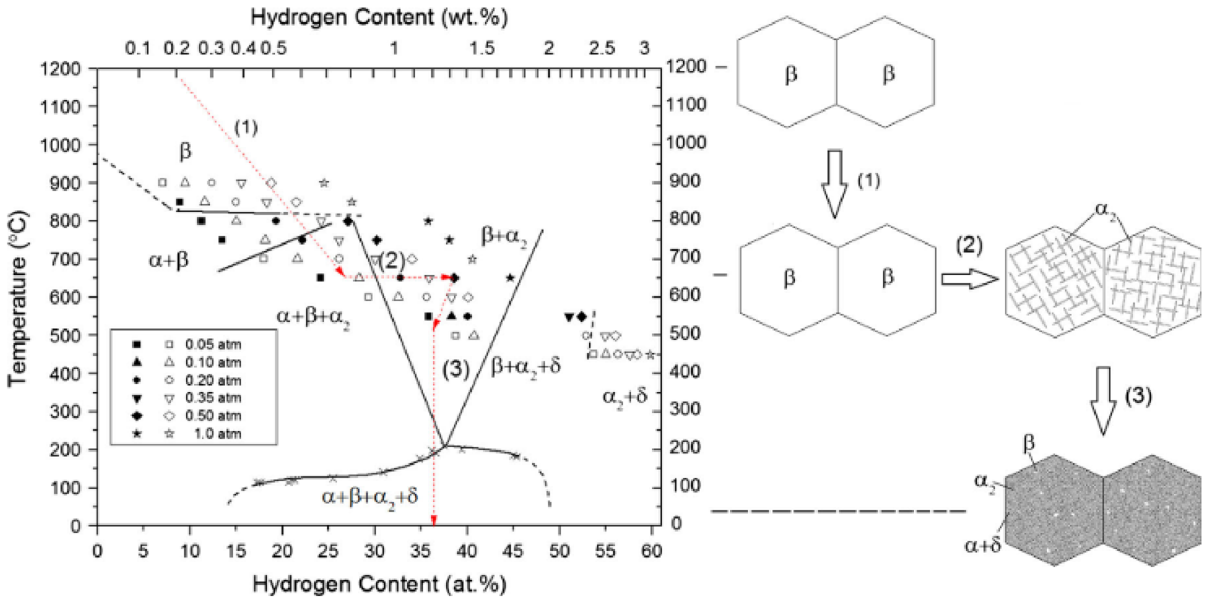

Figure 4.2: Pseudo-binary phase diagram of Ti-6Al-4V and hydrogen illustrating (1) cooling from densification step (1200 °C) to (2) phase transformation stage (650 °C) where homogenous α_2 nucleation occurs before (3) cooling to room temperature for α nucleation. Heating to 750 °C in vacuum environment to allow for dehydrogenation follows to remove hydride precipitates and preserve fine $(\alpha + \beta)$ microstructure. Adapted from [22]

This study investigated the effect of the first heating step above the β transus on the microstructure and tensile properties of LPBF Ti-6Al-4V. The differences in yield strength, ultimate tensile strength, and elongation to failure are then explained through characterization of the grain structure, crystallographic orientation and fractography, using a combination of light optical microscopy (LOM), scanning electron microscopy (SEM) and electron backscatter diffraction (EBSD).

4.2. Materials and Methods

Commercial Ti-6Al-4V ELI spherical powder feedstock with chemical composition detailed in Table 4.1 and 99% of the particle diameters in the range of 10μm-45μm was used with a

3DSystems ProX320 DMLS printer. Cylinders with a 13mm diameter and 115 mm length were printed with the longitudinal axis in 0° and 90° orientations with respect to the build direction. All samples were manufactured on a Ti-6Al-4V base plate with a laser power of 245 W, scan speed of 1250 mm/s, 113 μm hatch spacing and layer height of 60 μm. These parameters have been demonstrated previously to produce mostly dense as-built material with few LOF defects (>99.8% dense) [6, 19, 26]. As-printed samples were stress relieved at 600 °C for 4 h while still attached to the build plate, then removed by wire electrical discharge machining and separated into four different groups – a control group, which is the stress relieved condition, and three different THRM conditions.

Table 4.1: Measured chemical content of 3D Systems LaserForm Ti Gr. 23 Type A powder provided by supplier.

Ti	Al	V	C	O	N	H	Fe	Y	Other
Balance	6.35	3.91	0.02	0.08	0.02	0.0012	0.18	<0.001	<0.4

A schematic of the THRM process implemented for this study is shown in Figure 4.3. Three values of T_{max} were investigated (850 °C, 1025 °C, and 1200 °C), and a dynamically controlled H_2 partial pressure of 50 kPa H_2 and 50 kPa Ar was used during the 1 hour hold at T_{max} and during the 4 hr hold at 650 °C during which the $\beta \rightarrow \beta + \alpha_2$ phase transformation occurred. To facilitate dehydrogenation, the samples were held under vacuum (1x10^{-3} Pa) at 750 °C for 12 hr.

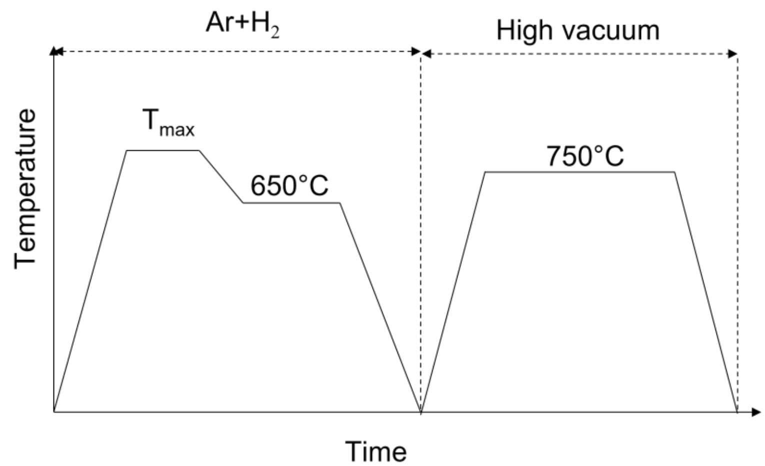

Figure 4.3: THRM processing diagram: maximum temperatures (T_{max}) used were 850 °C, 1025 °C and 1200°C for 1 hr, phase transformation $\beta \rightarrow \beta + \alpha_2$ takes place at 650°C step over 4 hr, and dehydrogenation at 750°C step for 12 hr.

Cross-sections of rods from each processing temperature were cut using wire electrical discharge machining for microstructural characterization. Samples were mechanically polished to 0.05μm colloidal silica and then etched with Kroll's reagent to reveal the microstructure. Etched samples were imaged using light optical microscopy (LOM) to observe the bulk grain morphology. Crystallographic orientations were measured on unetched material via a Tescan Mira 3 scanning electron microscope (SEM) equipped with an Oxford electron back-scattered diffraction (EBSD) detector and analyzed using EDAX OIM Analysis 7.

Five tensile specimens per treatment condition and orientation were machined with a gage length of 18 mm and diameter of 6 mm in accordance with ASTM E8. Tensile testing to fracture was carried out on an MTS servo-hydraulic load frame at a constant strain rate of 3 x 10^{-4} s^{-1} using an extensometer to measure strain. Post-mortem fracture surfaces were imaged using the SEM, and cross-sections of fracture were further prepared for LOM and EBSD characterization to investigate the fracture mechanisms.

4.3. Results

4.3.1. Microstructural Characterization

Representative LOM images of etched microstructures are shown in Figure 4.4 for the control (stress relieved), and the three (T_{max} = 850, 1050, and 1200 °C) THRM processed conditions. The stress relief condition exhibits small prior β grains comparable in size to the print layer height ~100 μm. Within the β grains, a needle-like basket weave/Widmanstätten structure is visible and consistent with the fast-cooled LPBF process. All THRM treated samples recrystallized and the stress relieved acicular microstructure was transformed to the characteristic fine homogeneously nucleated THRM microstructure. A continuous grain boundary α layer (GB α) lining the prior β grain boundaries was evident (red arrows in Figure 4.4).

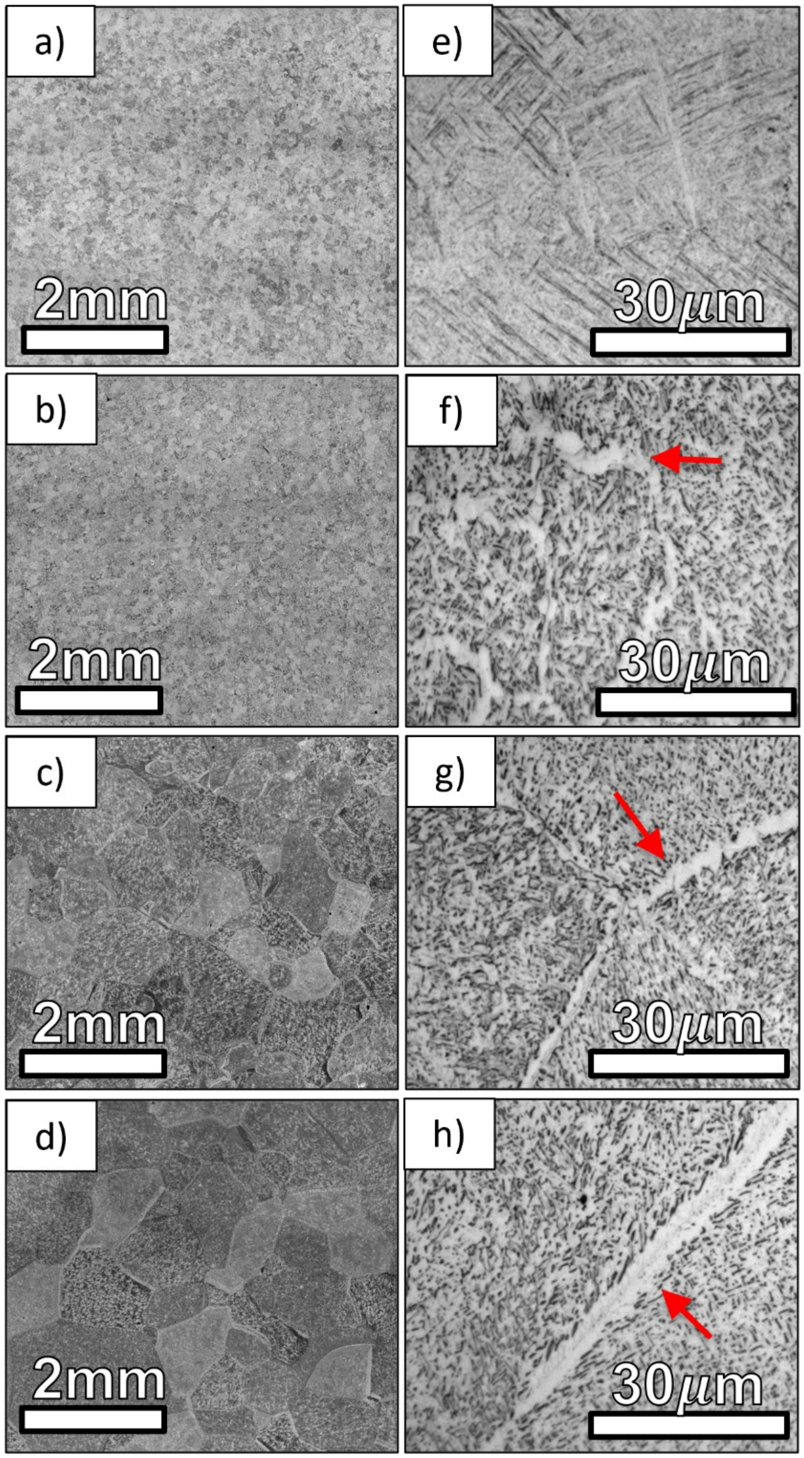

Figure 4.4: Representative optical micrographs revealing prior β grain structure (a,e) stress relief only (b,f) 850°C (c,g) 1025°C and (d,h)1200°C THRM densification temperature processed samples. No prior β grain growth was observed for sub-transus (a,b) HT, but large grain growth was observed for higher temperatures (c,d). Growth of continuous α layers at prior β grain boundaries was observed in all THRM samples (f-h).

Representative inverse pole figure (IPF) maps were used to highlight the α structures for all post-processing conditions, see Figure 4.5 for an example. The stress relieved control sample, shown in Figure 4.5(a), displays a fine acicular structure with no recognizable colonies of parallel lathes with shared orientation. By contrast, the THRM post-processed samples exhibit a consistent fine structure with low aspect ratios. Though the THRM microstructures appear to be lacking colonies STEM observations of samples treated with the similar HSPT process have shown their microstructures to contain ultra-fine parallel lathes (500 nm in width) within the contiguous orientations [20].

The following relevant microstructural measurements are summarized in Table 4.2. The optical micrographs were used to quantify prior β grain boundary α thickness and prior β grain sizes by measuring the average distance between intercepts along 50 randomly oriented lines through the microstructure. EBSD scans were used to quantify the average α lath width and length through automated technique in orientation mapping software. The samples treated at 850 °C exhibited prior β grains consistent sizes with the stress relieved samples (~100 μm), while the 1025 °C and 1200 °C samples show a large amount of growth in the prior β grains with some reaching as large as 2 mm in the samples processed at 1200 °C. There was some growth in the prior β grain boundary α layer thickness in the 1200 °C condition as compared to the lower THRM temperatures.

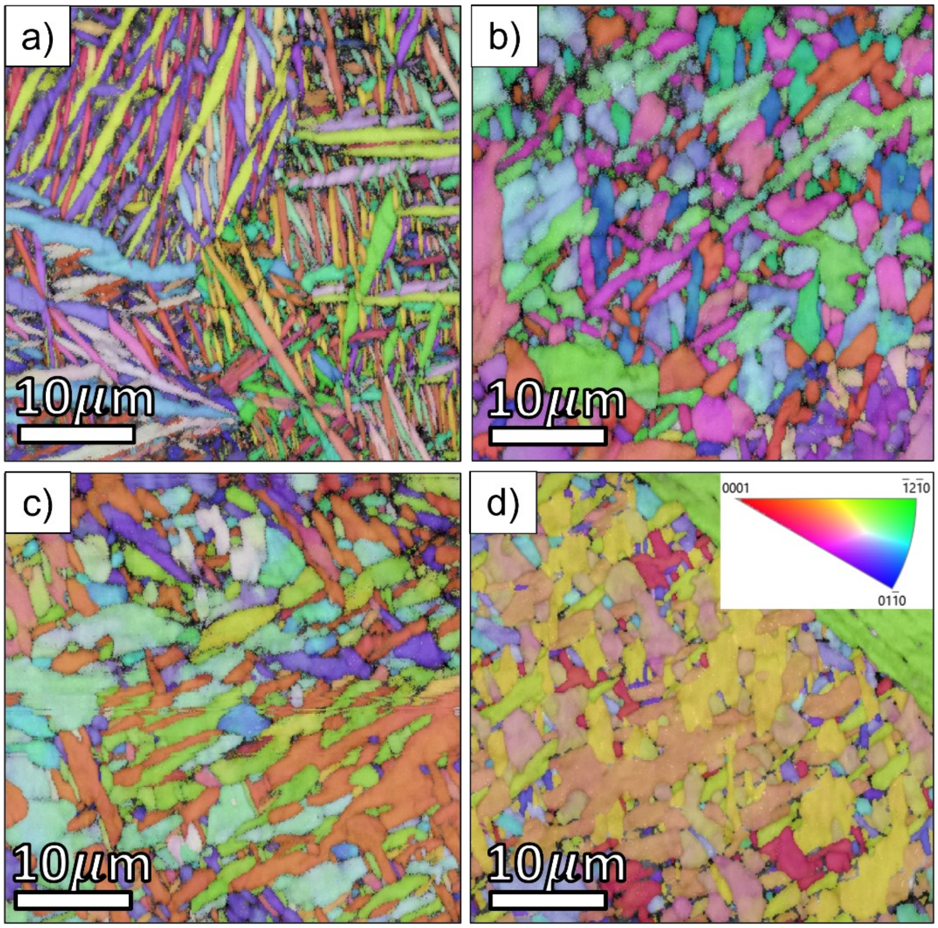

Figure 4.5: Representative EBSD maps of α lathe structure in a) stress relief only b) 850°C c) 1025°C and d) 1200°C THRM densification temperature processed samples.

Table 4.2: Relevant microstructural measurements for each processing condition. Large prior β grain growth observed in 1025°C and 1200°C samples. Homogenously nucleated α structure consistent across THRM samples.

Post Processing	Beta Grain size [μm]	GB α Width [μm]	Lathe Length [μm]	Lathe Width [μm]
Stress Relief	94	~	9.17	0.89
THRM 850°C	101	4.25	5.27	1.65
THRM 1025°C	496	4.10	6.37	1.76
THRM 1200°C	742	5.87	5.70	1.54

4.3.2. Tensile Properties

Samples were loaded in the 0° and 90° orientations with respect to the build direction, and resultant properties are displayed in Table 4.3. No significant trend of anisotropy was evident in the results, consistent with the lack of anisotropy evident in the microstructure. Two outlier samples caused the large spread in the 90° orientation 850 °C samples, otherwise the standard deviation for each group is consistent.

Table 4.3: Mechanical properties of each treatment temperature and tested orientation.

HT Temp	Orientation	UTS [MPa]	Yield Strength [MPa]	Elongation %
SR Only	0°	1203 ± 11	1057 ± 9	4.1 ± 1.3
SR Only	90°	1187 ± 4	1042 ± 4	5.05 ± 0.6
850 °C	0°	1003 ± 3	910 ± 9	14.6 ± 1.4
850 °C	90°	988 ± 51	890 ± 44	15.6 ± 6.3
1025 °C	0°	1004 ± 4	905 ± 9	10.4 ± 1.4
1025 °C	90°	1003 ± 5	906 ± 7	12.2 ± 1.1
1200 °C	0°	1011 ± 4	905 ± 7	12.2 ± 1.0
1200 °C	90°	1002 ± 6	907 ± 6	9.0 ± 0.9

A compilation of the mechanical properties is plotted in Figure 4.6 to better visualize the differences between conditions. The samples that only received stress relief were very brittle with 5% strain to failure. The THRM treated samples exhibited a drastic increase in ductility to an average 15 % failure strain for samples treated with a T_{max} of 850 °C. The ductility showed some reduction in the higher temperature THRM samples with an average strain to failure of 10 % in the T_{max} of 1200 °C samples. Samples treated with a T_{max} of 850 °C had the largest amount of variability in elongation with some samples reaching over 20 % elongation and the least ductile 10 %.

While there was a reduction in ductility for the samples treated with high T_{max}, the treatment temperature had little effect the strength of the THRM samples; all retained consistent yield and ultimate strengths of 900 and 1000 MPa, respectively. This consistent strength is due to the homogeneously nucleated microstructure seen in Figure 4.5.

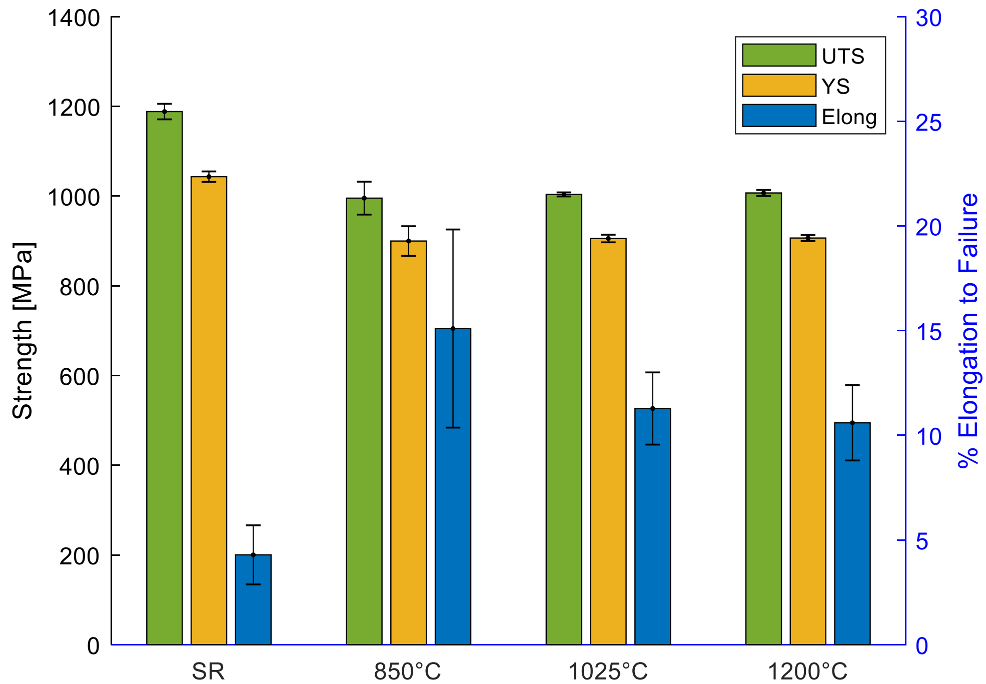

Figure 4.6: Resultant average tensile properties for heat treated conditions. Consistent reduction in strength from stress relieved to THRM conditions. Large increase in ductility observed for the 850°C condition that is reduced at higher temperatures.

4.3.3. Fractography

To investigate the failure modes associated with variations in ductility the fracture surfaces of tensile samples were imaged by SEM. Representative examples of each condition are shown in Figure 4.7. Fracture surfaces of the stress-relieved samples (Figure 4.7(a,b)) exhibited 500 μm pores with recognizable unmelted powder particles lining the interior, consistent with a lack of fusion pore. The samples with T_{max} 850 °C (Figure 4.7(c,d)) exhibited cup and cone fracture and extensive necking; some but not all samples also had lack of fusion pores present on the fracture surfaces with an apparent size around 200μm. The samples with higher densification temperature had an absence of lack of fusion pores but also showed a reduction in necking and did not exhibit cup-cone fracture. Samples treated at 1025°C (Figure 4.7(e,f)) show some faceted fracture, while those with a T_{max} of 1200°C (Figure 4.7(g,h)) have even more faceting. Faceted features were not observed in the fracture morphologies of the stress relief only or the 850°C samples.

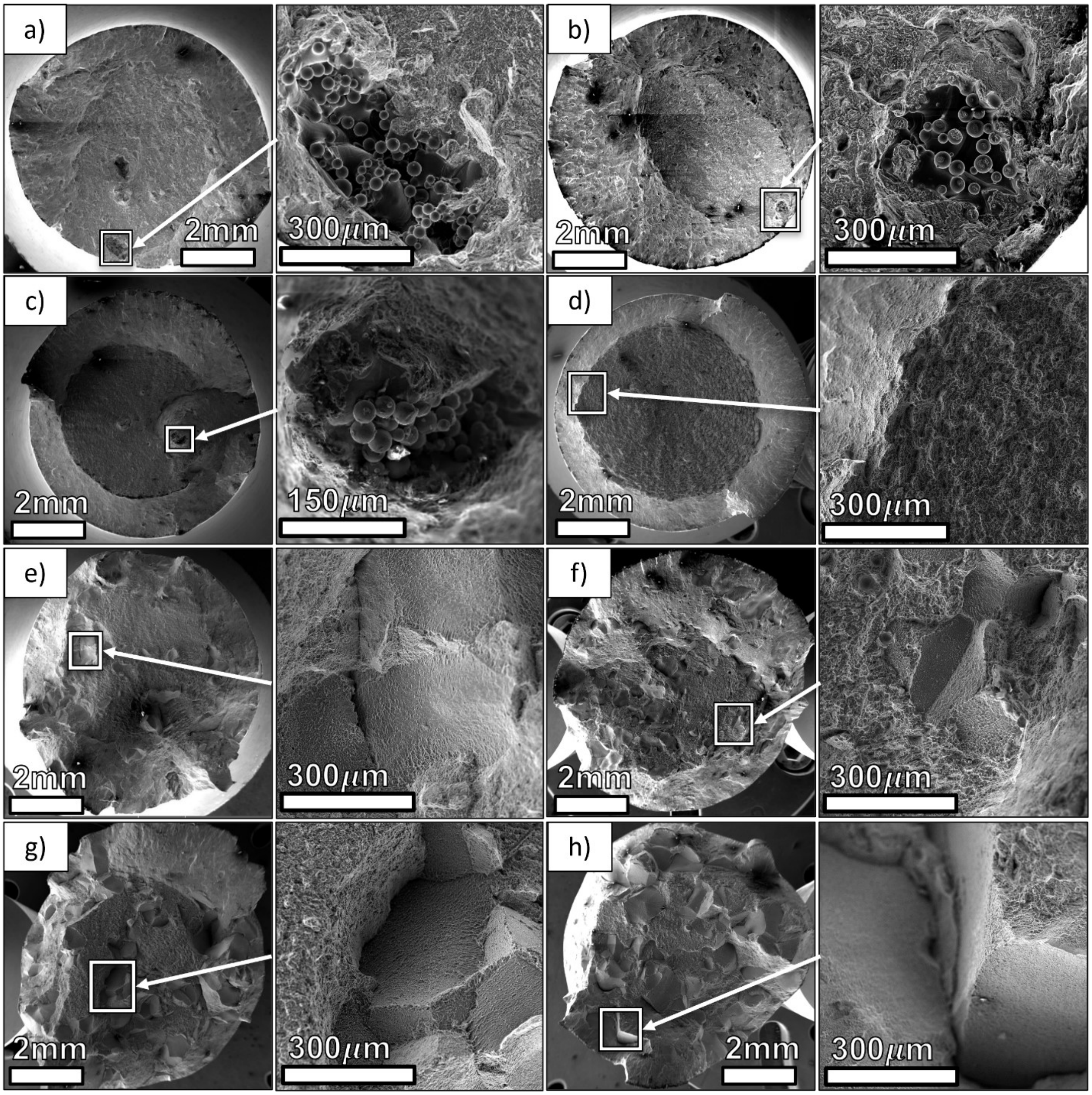

Figure 4.7: Representative fracture surfaces of (a,b) stress relief only (c,d) 850°C (e,f) 1025°C and (g,h) 1200°C densification temperature THRM treated samples. Magnified views of boxed regions: (a-c) LOF pores, (d) transition from ductile dimple fracture to shear cup, and (e-h) faceted fracture.

Cross-sections of fractured tension samples representative of each THRM condition are shown in Figure 4.8. Magnified views of the boxed regions show subsurface cracks forming along α decorated prior β grain boundaries (Figure 4.8(b,e)). Subsurface cracking along the prior β grain boundaries was observed in both 1025 °C and 1200 °C treated samples but was not seen in SR only or 850 °C samples. It is interesting to note that retained pores from print defects are visible adjacent to developing cracks in Figure 4.8(a,e) denoted by arrows, indicating that the grain boundary α was a preferential failure mode to the pores.

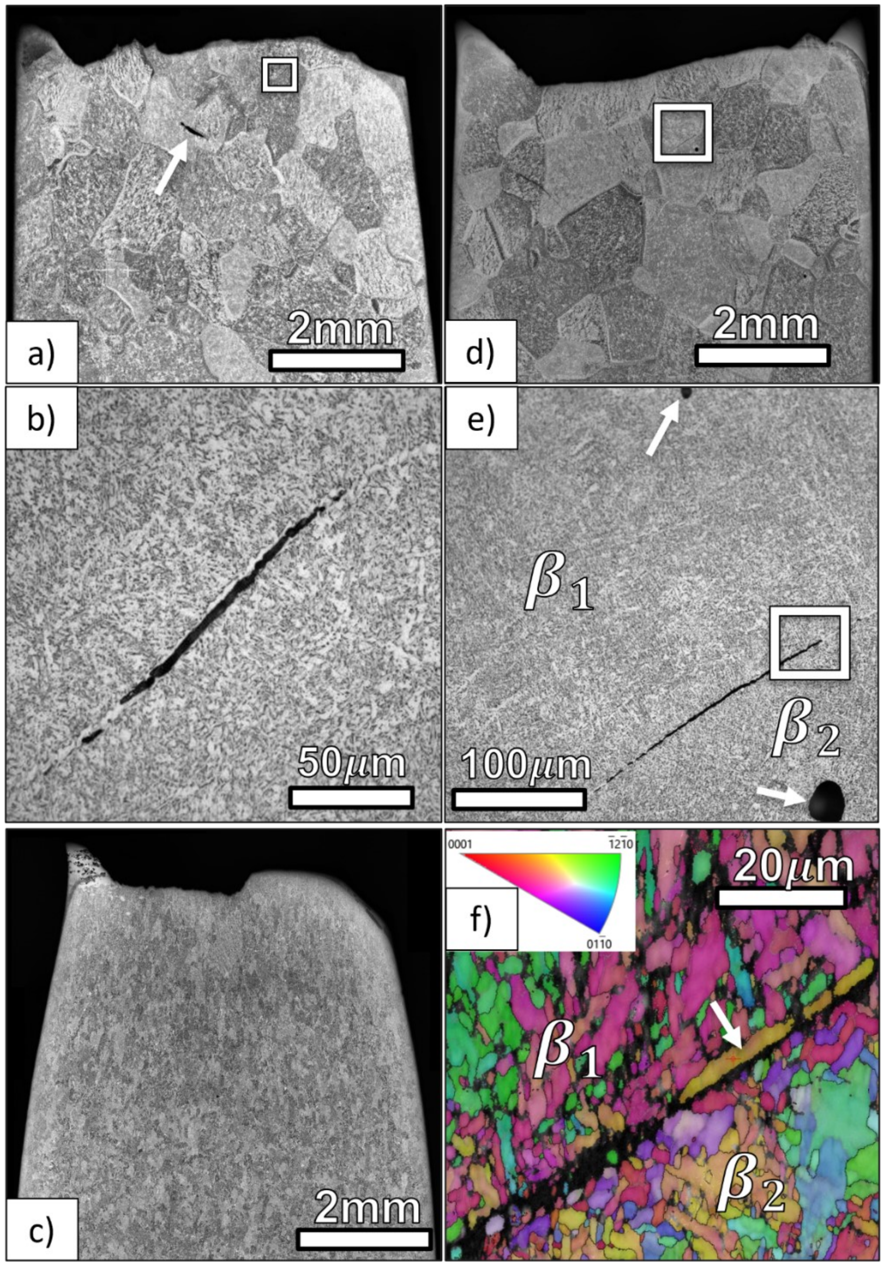

Figure 4.8: Optical microscopy etched microstructures of cross-section of fractured (a) 1025 °C, (c) 850 °C, (d) 1200 °C samples with tensile loading direction vertical. Subsurface cracks along continuous α layer in (b) 1025 °C and (e) 1200 °C from outlined boxes in (a) and (d). (f) EBSD orientation map of crack tip between prior β grain boundaries outlined in (e) with α layer denoted by the arrow. Retained pores noted by arrows in (a) and (e).

A magnified cross-section of a fracture facet in a 1200 °C sample is shown in Figure 4.9 with IPF mapping of the tip (Figure 4.9(b)) and root (Figure 4.9(c)) of the facet. The facet shows where a crack grew along the prior β grain boundary as was demonstrated in Figure 4.8. This crack propagated until a sufficient point was reached to trigger the less favorable fracture path through the interior of another prior β shown by the jagged fracture on the left of the SEM image denoted by an arrow. The tip of the arrested crack growing between the two grains can be seen in Figure 4.9(c). The two grains can be distinguished by the difference in variant orientations present, for example β_2 exhibits $[0001]$ and $[01\bar{1}0]$ orientations that are not present in β_1.

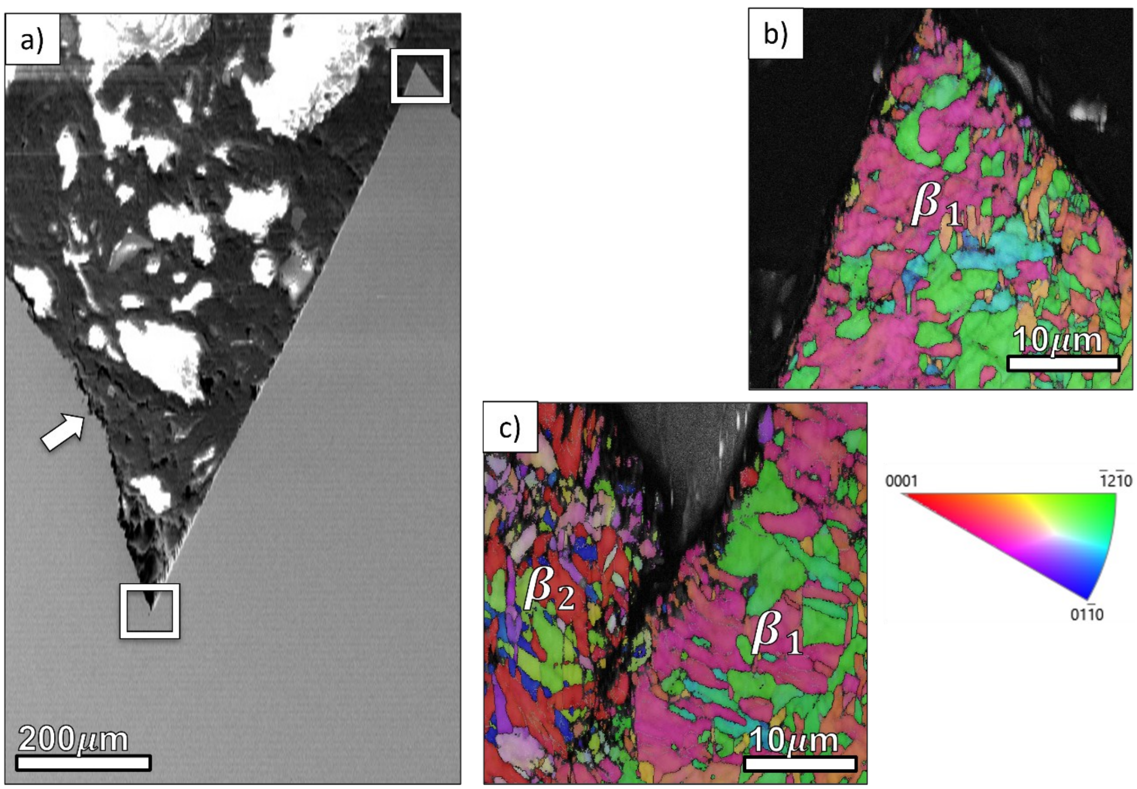

Figure 4.9: Cross-section of a fractured 1200 °C sample with tensile direction aligned vertically. (a) SEM image shows mounted sample on bottom with areas identified for (b,c) EBSD orientation maps; in (a) black and white features on top are the conductive mounting material, sample is grey on bottom. Straight intergranular fracture along prior β_1 grain observed on right, with jagged transgranular fracture through prior β_2 grain on left noted by arrow.

4.4. Discussion of Results

THRM has been shown to provide densification and reproduction of wrought-like microstructures from as-printed Ti-6Al-4V resulting in a moderate reduction in strength (UTS: 1200 to 1000 MPa) and a large increase in ductility (5% to 16% elongation to failure). Previous work used a higher densification temperature of 1050 °C, the addition of globularization and aging steps yielded properties that are comparable to those seen in the current 850 °C samples as opposed to the similar temperature 1025 °C condition in this study [25]. The globularization step increased the α lathe sizes (from a width of 2 μm to 5 μm). This allows for a longer slip distances that alleviated the preferential fracture along the prior grain boundaries, as demonstrated by ductile dimple fracture morphologies.

The reduction of ductility from the 850 °C samples to the 1025 °C and 1200 °C samples can be attributed to the larger prior β grains that allow for longer uninterrupted grain boundary α. Cracks nucleate and propagate along the grain boundary α, which is easier than going through the fine structure within the prior β grains. The phenomenon of grain boundary α causing longer slip lengths resulting in faceted fracture has also been reported to affect fatigue with the similar HSPT PM process [27]. The fracture of the stress-relieved and 850 °C samples were found to be influenced by residual porosity as evidenced by the LOF pores on the fracture surfaces. By contrast, the fracture of 1025 °C and 1200 °C samples is dominated by the grain boundary cracking.

All three temperatures investigated here produced material with tensile properties that meet the requirements set by the ASTM B348 standard for annealed wrought Ti-6Al-4V and are comparable to results from studies applying HIP to LPBF Ti-6Al-4V [16-19]. The THRM process presents a simplification of the post-processing of AM Ti-6Al-4V as it can be done in commonly accessible vacuum furnaces as opposed to the specialized equipment required for HIP while providing an additional control over the microstructure.

4.5. Chapter Summary

In this chapter, the effect that the densification temperature in the THRM process has on microstructure and tensile properties of LPBF Ti-6Al-4V was explored. All THRM temperatures produced the characteristic fine homogeneously nucleated microstructure and resulted in continuous α layers along the prior β grain boundaries. As compared to control samples with the stress-relieved martensitic microstructure, there was a consistent moderate reduction in strength and a large increase in ductility. In the 850 °C condition retained porosity was noted and appeared to affect ductility, though was still the most ductile condition (15% elongation to failure). Samples processed with a T_{max} well above the β transus temperature underwent large growth in the prior β grains and exhibited a prior grain boundary cracking fracture morphology. This limited ductility to 11% elongation by providing longer uninterrupted paths for cracks to grow. With further optimization of the process including the addition of a globularization step, the negative effects of the continuous α layer lining the prior β grains can be mitigated so that the microstructural control and potential for densification benefits of the process can be fully utilized. The THRM process has demonstrated the capacity to produce preferential microstructures with resultant tensile properties comparable to HIP without requiring an expensive and specialized HIP chamber.

4.6. References for Chapter 4

1. Xu, W., et al., *Additive manufacturing of strong and ductile Ti–6Al–4V by selective laser melting via in situ martensite decomposition.* Acta Materialia, 2015. **85**: p. 74-84.
2. Askari, M., et al., *Additive manufacturing of metamaterials: A review.* Additive Manufacturing, 2020. **36**: p. 101562.
3. Cunningham, R., et al., *Keyhole threshold and morphology in laser melting revealed by ultrahigh-speed x-ray imaging.* Science, 2019. **363**(6429): p. 849-852.
4. H, G., et al., *Defect Morphology in Ti-6Al-4V Parts Fabricated by Selective Laser Melting and Electron Beam Melting*, in *24rd Annual International Solid Freeform Fabrication Symposium—an Additive Manufacturing Conference*. 2013: Austin, TX. p. 440-453.
5. Mercelis, P. and J.P. Kruth, *Residual stresses in selective laser sintering and selective laser melting.* Rapid Prototyping Journal, 2006. **12**(5): p. 254-265.
6. Shipley, H., et al., *Optimisation of process parameters to address fundamental challenges during selective laser melting of Ti-6Al-4V: A review.* International Journal of Machine Tools & Manufacture, 2018. **128**: p. 1-20.
7. H, G., et al., *The Effects of Processing Parameters on Defect Regularity in Ti-6Al-4V Parts Fabricated By Selective Laser Melting and Electron Beam Melting*. 2013. p. 424-439.
8. Song, B., et al., *Effects of processing parameters on microstructure and mechanical property of selective laser melted Ti6Al4V.* Materials & Design, 2012. **35**: p. 120-125.
9. Kasperovich, G., et al., *Correlation between porosity and processing parameters in TiAl6V4 produced by selective laser melting.* Materials & Design, 2016. **105**: p. 160-170.
10. Ali, H., et al., *In-situ residual stress reduction, martensitic decomposition and mechanical properties enhancement through high temperature powder bed pre-heating of Selective Laser Melted Ti6Al4V.* Materials Science and Engineering: A, 2017. **695**: p. 211-220.
11. Lewandowski, J.J. and M. Seifi, *Metal Additive Manufacturing: A Review of Mechanical Properties.* Annual Review of Materials Research, 2016. **46**(1): p. 151-186.
12. Huang, R., et al., *Energy and emissions saving potential of additive manufacturing: the case of lightweight aircraft components.* Journal of Cleaner Production, 2016. **135**: p. 1559-1570.
13. Hao, Y.-L., S.-J. Li, and R. Yang, *Biomedical titanium alloys and their additive manufacturing.* Rare Metals, 2016. **35**(9): p. 661-671.
14. Helle, A.S., K.E. Easterling, and M.F. Ashby, *Hot-isostatic pressing diagrams: New developments.* Acta Metallurgica, 1985. **33**(12): p. 2163-2174.
15. Dutta, B. and F.H. Froes, *Additive Manufacturing of Titanium Alloys*. 2016: Elsevier.
16. Hrabe, N., T. Gnäupel-Herold, and T. Quinn, *Fatigue properties of a titanium alloy (Ti–6Al–4V) fabricated via electron beam melting (EBM): Effects of internal defects and residual stress.* International Journal of Fatigue, 2017. **94**: p. 202-210.
17. Qiu, C., N.J.E. Adkins, and M.M. Attallah, *Microstructure and tensile properties of selectively laser-melted and of HIPed laser-melted Ti–6Al–4V.* Materials Science and Engineering: A, 2013. **578**: p. 230-239.

18. Leuders, S., et al., *On the mechanical behaviour of titanium alloy TiAl6V4 manufactured by selective laser melting: Fatigue resistance and crack growth performance.* International Journal of Fatigue, 2013. **48**: p. 300-307.
19. Kasperovich, G. and J. Hausmann, *Improvement of fatigue resistance and ductility of TiAl6V4 processed by selective laser melting.* Journal of Materials Processing Technology, 2015. **220**: p. 202-214.
20. Paramore, J.D., et al., *Hydrogen-enabled microstructure and fatigue strength engineering of titanium alloys.* Sci Rep, 2017. **7**: p. 41444.
21. Paramore, J.D., et al., *Powder Casting: Producing Bulk Metal Components from Powder Without Compaction.* Jom, 2020. **72**(9): p. 3112-3120.
22. Sun, P., et al., *Phase Transformations and Formation of Ultra-Fine Microstructure During Hydrogen Sintering and Phase Transformation (HSPT) Processing of Ti-6Al-4V.* Metallurgical and Materials Transactions A, 2015. **46**(12): p. 5546-5560.
23. Dunstan, M.K., et al., *Manipulation of microstructure and mechanical properties during dehydrogenation of hydrogen-sintered Ti–6Al–4V.* Materials Science and Engineering: A, 2019. **764**: p. 138244.
24. Paramore, J.D., et al., *THERMO - HYDROGEN REFINEMENT OF MICROSTRUCTURE OF TITANIUM MATERIALS*. 2019.
25. Knezevic, M., et al., *Thermo-hydrogen refinement of microstructure to improve mechanical properties of Ti–6Al–4V fabricated via laser powder bed fusion.* Materials Science and Engineering: A, 2021. **809**: p. 140980.
26. Van Hooreweder, B., et al., *Analysis of Fracture Toughness and Crack Propagation of Ti6Al4V Produced by Selective Laser Melting.* Advanced Engineering Materials, 2012. **14**(1-2): p. 92-97.
27. Dunstan, M.K., et al., *Analysis of microstructural facet fatigue failure in ultra-fine grained powder metallurgy Ti-6Al-4V produced through hydrogen sintering.* International Journal of Fatigue, 2020. **131**: p. 105355.

CHAPTER 5: SUMMARY AND FINDINGS

This thesis work was undertaken to expand the understanding of the mechanical properties of additively manufactured (AM) material and to inform topology optimized designs for lightweight structures. Additively manufactured metals are prone to anisotropic inhomogeneous microstructures and defects that must be characterized along with their attendant mechanical properties to accurately predict part performance [1]. The alloy Ti-6Al-4V was selected due to its high specific strength and ubiquity in AM as well as general structural applications [2].

5.1. Review of key findings

Cylinders of 0°, 45°, and 90° orientations with respect to the build direction were printed using laser powder bed fusion (LPBF) then subjected to stress relief, hot isostatic pressing (HIP), and aging heat treatments. The processed material was subjected to microstructural characterization including optical microscopy, X-ray diffraction (XRD), electron backscatter diffraction (EBSD), and computed tomography (CT). Cylinders were machined into tension, compression, and shear mechanical test specimens and tested at quasi-static strain rates to provide measurements of the elasticity and yield behavior. The results can be summarized as follows:

- Post-processed material was revealed to have undergone a significant amount of microstructural coarsening by optical micrographs, to be absent of any strong texture by XRD and EBSD results, and to be fully dense by CT scans.
- The measured mechanical properties did not exhibit anisotropy, but a significant asymmetry in the tension and compression strengths was evident. The material was exceptionally ductile due to the absence of porosity and very large lamellae in the microstructure.

- The asymmetric yield surface was constructed using experimental results, capturing the tension and compression strengths well. The shear strengths measured using a 0.2% strain offset method fell well below the yield surface suggesting a further evaluation of the shear experiment was necessary.

A finite element simulation of the compact forced simple-shear (CFSS) experiment was generated to evaluate the resultant stress and strain states throughout the quasi-static experiment. As isotropic strain hardening model was defined using measured tensile properties from a rolled bar of Grade 5 Ti-6Al-4V that was also used for CFSS samples in experiments conducted to support the simulations. A procedure for automating the analysis of digital image correlation (DIC) experimental datasets by identifying the localization of strain on the sheared plane was developed. The results are summarized as follows:

- Finite element simulation results confirmed that the stress and strain state on the sheared plane is very close to a pure Mode II shear state. The average stress-strain behavior in the simulations agreed well with the experimental results. The simulations also showed that in the plastic regime the elastic strain is concentrated in the shear component, which was demonstrated experimentally by unloading after yielding with measurements of shear moduli 39.2$\pm$0.4 GPa as compared to expected value of 36.7 GPa.
- It was demonstrated that due to inhomogeneous and localized yielding on the shear plane the average stress-strain response diverges from linear well before reaching macroscopic yielding. Back-calculating from the true yield strength in the simulation results it was determined that a 2.8% offset is required to achieve extended yielding and measure accurate yield strengths in wrought Ti-6Al-4V CFSS specimens.

- Revisiting the yield values of the printed LPBF CFSS specimens using the new 2.8% offset produced results that fell on and supported the yield surface derived from the tension and compression results.

The dependence of microstructure and resultant properties on temperature used in a hydrogen-based heat treatment referred to as thermo-hydrogen refinement of microstructure (THRM) was investigated. The temperatures investigated were T_{max}= 850 °C (β transus), T_{max}= 1025 °C, and T_{max}= 1200 °C. The results are summarized as follows:

- All three temperatures effectively recrystallized the as-built martensitic microstructure to the ultrafine $\alpha + \beta$ microstructure characteristic of the THRM process. This change in microstructure was correlated with a large increase in ductility and moderate reduction in strength from the strong but brittle stress-relieved results.
- The maximum ductility was found in the 850 °C condition (15% elongation to failure) with reduction in the 1025 °C (11%) and 1200 °C (10%) conditions. Fractography and microstructural analysis revealed this reduction to be due to the growth of large faceted prior β grains at the higher temperatures and the formation of continuous grain boundary α that promoted grain boundary cracking.
- The THRM process does present a simplification of post-processing of AM Ti-6Al-4V as it produces properties comparable to HIP without requiring the specialized equipment. The selection of annealing temperatures can have a big effect on microstructure and properties and must be chosen judiciously.

Taken as a whole, an effective and efficient means for measuring the full directional elastic and plastic performance of AM materials was demonstrated. A promising alternative post-process was evaluated and shown to present a simplified and cost-effective alternative for the production of AM Ti-6Al-4V.

5.2. Future Directions

The results and conclusions in this dissertation help elucidate mechanical responses in additively manufactured titanium under different processing conditions. The findings in this work can be utilized to streamline LPBF processing and heat treatment, and to inform topology optimization methods for the design of lightweight structures, which will undoubtedly prompt further investigations. Areas where this work may be expanded in the future are as follows:

- The accuracy of the measured yield and elastic properties as implemented in topology optimized designs are yet to be determined. The preeminent feature of the mechanical properties in stress-relieved and HIPed LPBF Ti-6Al-4V was an asymmetry in the tension-compression yield strengths. A design problem that incorporates both tensile and compressive stresses, like beam bending, would best demonstrate improvements over more traditional symmetric assumptions. Coupling experiments with DIC could be used as a direct comparison to simulation predictions.
- As conventionally and topology optimized light weighted structures often have lattice-like features with relatively small ligament sizes, an investigation into mechanical responses of these structures is warranted. Probing the effect of feature sizes on microstructures and resultant properties absent surface machining could provide important insight when implementing design rules on reduced length scales. Lattices are essentially periodic structures of connected nodes, investigating individual nodes would provide a detailed understanding of mechanical responses that could be

extrapolated to full structures. Expanding beyond quasi-static strain rates would be of particular interest to energy absorption applications [3].

- The THRM process was demonstrated to be effective in producing desirable microstructures and reliable properties from as-built material. THRM with an additional globularization step was recently demonstrated to significantly increase the endurance limit in fatigue and did not exhibit the same fracture issues associated with continuous α along prior β grain boundaries as was observed in the current study [4]. As grain boundary sliding is a dominant creep mechanism, a study of these different THRM conditions with their unique grain structures would also be of interest in high temperature applications relevant to turbine components.

5.3. References for Chapter 5

1. Lewandowski, J.J. and M. Seifi, *Metal Additive Manufacturing: A Review of Mechanical Properties.* Annual Review of Materials Research, 2016. **46**(1): p. 151-186.
2. Liu, S. and Y.C. Shin, *Additive manufacturing of Ti6Al4V alloy: A review.* Materials & Design, 2019. **164**: p. 107552.
3. Tancogne-Dejean, T., A.B. Spierings, and D. Mohr, *Additively-manufactured metallic micro-lattice materials for high specific energy absorption under static and dynamic loading.* Acta Materialia, 2016. **116**: p. 14-28.
4. Knezevic, M., et al., *Thermo-hydrogen refinement of microstructure to improve mechanical properties of Ti–6Al–4V fabricated via laser powder bed fusion.* Materials Science and Engineering: A, 2021. **809**: p. 140980.

APPENDIX 1: SHEAR DIC ANALYSIS MATLAB CODE

```
function DIC_Visualizer_test
```

```
global handles vars
clear all global
clc
```

Creating GUI

```
%Create window to contain everything
screen_pos = get(0,'ScreenSize');
main_pos = [(screen_pos(3)-1200)/2,(screen_pos(4)-500)/2,1200,500];
handles.window = figure('Name','DIC
Visualizer','NumberTitle','off','Visible','off','Position',main_pos);%,'ResizeFcn',@resize_fcn);
set(handles.window, 'MenuBar', 'none');
set(handles.window, 'ToolBar', 'none');

handles.main_menu = uimenu(handles.window,'Text','&File');
handles.edit_menu = uimenu(handles.window,'Text','&Edit');
handles.analyze_menu = uimenu(handles.window,'Text','&Analyze','Visible','off');

handles.panel_w = 215;
handles.file_h = 90;
handles.plot_h = 300;
plot_panel_pos = [main_pos(3)-handles.panel_w,main_pos(4)-handles.file_h-handles.plot_h-
10,handles.panel_w,handles.plot_h];


%Add tabs section
    handles.tabgp = uitabgroup(handles.window,'Units','pixels','Position',[0 0 main_pos(3)
main_pos(4)]);

    %Plot Tab
    handles.tab{1} = uitab(handles.tabgp,'Title','Dic Data');
        %Panel to house plot
        handles.rawDIC_tab = uipanel(handles.tab{1},'Units','pixels','Position',[0 0 main_pos(3)-
handles.panel_w main_pos(4)-20],'Visible','off');
        handles.plot_axes{1} = axes(handles.rawDIC_tab);

    %Menu items to load Data and images
    handles.m_open = uimenu(handles.main_menu,'Text','&Open
Project','Accelerator','o','MenuSelectedFcn',@OpenProject);
    handles.m_saveproj = uimenu(handles.main_menu,'Text','&Save
Project','Accelerator','s','MenuSelectedFcn',@SaveWksp,'Visible','off');
    handles.m_saveexcel =
uimenu(handles.main_menu,'Text','&Export','Accelerator','e','MenuSelectedFcn',@SaveXLS,'Visible',
'off');
    handles.m_DIC = uimenu(handles.main_menu,'Text','Select DIC
Data','MenuSelectedFcn',@select_DICdata);
    handles.m_img = uimenu(handles.main_menu,'Text','Select
```

```
Images','MenuSelectedFcn',@select_images);
    handles.m_load = uimenu(handles.main_menu,'Text','Select Load
Data','MenuSelectedFcn',@load_data);
    handles.m_clear = uimenu(handles.main_menu,'Text','Clear
Data','MenuSelectedFcn',@clear_data,'Visible','off');
    handles.m_analyze = uimenu(handles.analyze_menu,'Text','Analyze Shear
Data','MenuSelectedFcn',@Analyze);
    handles.m_surffit = uimenu(handles.analyze_menu,'Text','Surface Fit Shear Data
(faster)','MenuSelectedFcn',@AnalyzeSurf);
    handles.m_stitchload = uimenu(handles.analyze_menu,'Text','Match Load
Data','MenuSelectedFcn',@stitch_load);

    %Add Side Panel for plot options
    handles.plotopt_panel =
uipanel(handles.tab{1},'Units','pixels','Position',plot_panel_pos,'Title','Plot
Options','Visible','off');
    panel_pos = handles.plotopt_panel.Position;


    %Sliders to select image and position to plot
    handles.text{1} = uicontrol(handles.plotopt_panel,'Style','Text','String','Image
Number:','Position',[5 panel_pos(4)-40 100 20]);
    handles.text{2} =
uicontrol(handles.plotopt_panel,'Style','Text','String','/1200','Position',[panel_pos(3)-
40,handles.text{1}.Position(2)-15,40,20]);
    handles.edit{1} = uicontrol
(handles.plotopt_panel,'Style','edit','String','50','Position',[handles.text{2}.Position(1)-
40,handles.text{2}.Position(2),40,20],'Callback',@ImgEdit);
    handles.sldr{1} = uicontrol
(handles.plotopt_panel,'Style','slider','Position',[5,handles.text{2}.Position(2),...
        panel_pos(3)-
(handles.text{2}.Position(3)+handles.edit{1}.Position(3)+10),20],'Min',1,'Max',100,'Value',50,'Ca
llback',@ImgSlide);

    handles.text{3} = uicontrol(handles.plotopt_panel,'Style','Text','String','Cross-Section
Position:','Position',[5 handles.text{2}.Position(2)-45 150 20]);
    handles.text{4} =
uicontrol(handles.plotopt_panel,'Style','Text','String','/1200','Position',[panel_pos(3)-
40,handles.text{3}.Position(2)-15,40,20]);
    handles.edit{2} = uicontrol
(handles.plotopt_panel,'Style','edit','String','50','Position',[handles.text{4}.Position(1)-
40,handles.text{4}.Position(2),40,20],'Callback',@PosEdit);
    handles.sldr{2} = uicontrol
(handles.plotopt_panel,'Style','slider','Min',1,'Max',100,'Position',[5,handles.text{4}.Position(
2),...
        panel_pos(3)-
(handles.text{4}.Position(3)+handles.edit{2}.Position(3)+10),20],'Value',50,'Callback',@PosSlide)
;

    %Button Group to select direction plot
    handles.bg{1} = uibuttongroup(handles.plotopt_panel,'Units','pixels',...
          'Position',[5 handles.text{4}.Position(2)-75 handles.panel_w/2 50],'Title','Plot Slice
Direction','SelectionChangedFcn',@pos_btn);
```

```
    handles.r1{1} = uicontrol(handles.bg{1},'Style','radiobutton','String','X','Position',[10 0
30 30]);

    handles.r1{2} = uicontrol(handles.bg{1},'Style','radiobutton','String','Y','Position',[45 0
100 30]);

    %Apply fit to the slice plot?
    handles.fitcheck = uicontrol(handles.plotopt_panel,'Style','checkbox','String','Linear
Fit','Position',...
        [2,handles.bg{1}.Position(2)-30,75,20],'Callback',@FitCheck);
    handles.infledit = uicontrol (handles.plotopt_panel,'Style','edit','Position',[75
handles.fitcheck.Position(2) 20 20],'Callback',@InflEdit);
    set(handles.infledit,'Enable','off');
    handles.text{5} = uicontrol (handles.plotopt_panel,'Style','Text','String',':Max # of
inflections','Position',[100 handles.fitcheck.Position(2) 110 20]);

    %select spatial data to plot
    handles.colselect = uicontrol(handles.plotopt_panel,'Style','popupmenu','Position',[5
handles.text{5}.Position(2)-30 100 20],'Callback',@strain_btn,'Visible','off');


    %Priming values
    vars = [];
    vars.path = [];

%Make window visible
handles.window.Visible = 'on';

a=1;
```

Select DIC data

```
    function select_DICdata(src,event)

        if isempty(vars.path)==0 && any(vars.path ~= 0)
            [DICfile,DICpath] = uigetfile({'*.csv;*.xls;*.xlsx'},'Select Your DIC
Files',vars.path,'MultiSelect','on');
        else
            [DICfile,DICpath] = uigetfile({'*.csv;*.xls;*.xlsx'},'Select Your DIC
Files','MultiSelect','on');
        end

        if DICfile{1} == 0
            return
        end

        vars.path = DICpath;


        vars.DIC.files = DICfile;
        vars.DIC.filepath = strcat(DICpath,DICfile);

        data = importdata(vars.DIC.filepath{end});
```

```
        vars.DIC.data = data.data;

        vars.DIC.colheaders = data.colheaders;
        handles.colselect.String = data.colheaders;
        set(handles.colselect,'Value',9);

        vars.poscol(1) = find(contains(data.colheaders,{'"x"'},'IgnoreCase',true));
        vars.poscol(2) = find(contains(data.colheaders,{'"y"'},'IgnoreCase',true));
        vars.col.x = vars.poscol(1);
        vars.col.y = vars.poscol(2);
        vars.col.u = find(cell2mat(cellfun(@(x)
contains(vars.DIC.colheaders,x,'IgnoreCase',true),{'"u"'}, 'UniformOutput', 0)));
        vars.col.v = find(cell2mat(cellfun(@(x)
contains(vars.DIC.colheaders,x,'IgnoreCase',true),{'"v"'}, 'UniformOutput', 0)));
        vars.col.sig = find(cell2mat(cellfun(@(x)
contains(vars.DIC.colheaders,x,'IgnoreCase',true),{'"Sigma"'}, 'UniformOutput', 0)));

        vars.unicol{1} = unique(vars.DIC.data(:,vars.poscol(1)));
        vars.unicol{2} = unique(vars.DIC.data(:,vars.poscol(2)));

        lastimg = vars.DIC.data;

        %find mins and maxs of data


            %decides if the data is negative and needs to be flipped to positive
        for i = 1:3
            last_max = max(lastimg(:,i+8));
            last_min = min(lastimg(:,i+8));

            if abs(last_min) > abs(last_max)
                vars.factor(i) = -1;
            else
                vars.factor(i) = 1;
            end
        end





        handles.sldr{1}.Min = 1;
        handles.sldr{1}.Max = length(DICfile);
        handles.sldr{1}.Value = handles.sldr{1}.Max;
        handles.edit{1}.String = length(DICfile);
        handles.text{2}.String = sprintf('/%d',length(DICfile));

        handles.sldr{2}.Min = 1;
        handles.sldr{2}.Max = length(vars.unicol{2});
        handles.sldr{2}.Value = round((handles.sldr{2}.Max-handles.sldr{2}.Min)/2);
        handles.edit{2}.String = vars.unicol{2}(round(handles.sldr{2}.Value));
        handles.text{4}.String = sprintf('/%d',max(vars.unicol{2}));

        %handles.bg{1}.Visible = 'off';
        handles.rawDIC_tab.Visible = 'on';
```

```
        handles.plotopt_panel.Visible = 'on';
        handles.colselect.Visible = 'on';
        handles.analyze_menu.Visible = 'on';
        handles.m_saveproj.Visible = 'on';
        handles.m_clear.Visible = 'on';



        update_plots
    end


    function [DICdata] = load_DIC(filenames,img)

        data = importdata(filenames{img});
        DICdata = data.data;
        vars.DIC.colheaders = data.colheaders;

    end
```

Loading load data

```
    function load_data(src,event)
        if isempty(vars.path)==0 && any(vars.path ~= 0)
            [loadfile,loadpath] = uigetfile({'*.csv;*.xls;*.xlsx;*.dat;*.txt'},'Select Your DIC
Files',vars.path,'MultiSelect','off');
        else
            [loadfile,loadpath] = uigetfile({'*.csv;*.xls;*.xlsx;*.dat;*.txt'},'Select Your DIC
Files','MultiSelect','off');
        end

        vars.path = loadpath;
        if loadfile == 0
            return
        end

        vars.load = importdata(strcat(loadpath,loadfile));
        vars.load.filepath = strcat(loadpath,loadfile);

    end
```

Select Image files for stitching to load data

```
    function select_images(src,event)

        if isempty(vars.path)==0 && any(vars.path ~= 0)
            [IMGfile,IMGpath] = uigetfile({'*.tif;*.bmp;*.jpeg'},'Select Your Image
Files',vars.path,'MultiSelect','on');
        else
            [IMGfile,IMGpath] = uigetfile({'*.tif;*.bmp;*.jpeg'},'Select Your Image
Files','MultiSelect','on');
        end
```

```
        if IMGfile{1} == 0
            return
        end

        vars.path = IMGpath;
        vars.IMG.files = IMGfile;
        vars.IMG.filepath = strcat(IMGpath,IMGfile);

    end
```

Stitch Load-Strain Data

```
    function stitch_load(src,event)

        %identify load data properties
        loadcols = length(vars.load.colheaders);
        exptime = find(cell2mat(cellfun(@(x)
contains(vars.load.colheaders,x,'IgnoreCase',true),{'Time','sec'}, 'UniformOutput', 0)));
        exptime = max(exptime-(ceil(exptime./loadcols)-1)*loadcols);
        expload = find(cell2mat(cellfun(@(x)
contains(vars.load.colheaders,x,'IgnoreCase',false),{'Load','load','Force','force','N'},
'UniformOutput', 0)));
        expload = expload-(ceil(expload./loadcols)-1)*loadcols;
        expdisp = find(cell2mat(cellfun(@(x)
contains(vars.load.colheaders,x,'IgnoreCase',true),{'Disp','Position','mm'}, 'UniformOutput',
0)));
        expdisp = expdisp-(ceil(expdisp./loadcols)-1)*loadcols;

        %identify image FPS
        img_start = dir(vars.IMG.filepath{1});
        img_final = dir(vars.IMG.filepath{end});
        fps = etime(datevec(img_final.date),datevec(img_start.date))/length(vars.IMG.filepath);

        elapse_image = ([0:length(vars.IMG.filepath)-1].*fps).';

        elapse_load = vars.load.data;
        shift_daq = elapse_load(end,exptime)-elapse_image(end);
        elapse_load(:,exptime) = elapse_load(:,exptime)-shift_daq; %makes final image and final
data pt at same time interval

        vars.load.stitch = cell(length(elapse_image),size(elapse_load,2));

        for i = 1:length(elapse_image)
            [~,ind] = min(abs(elapse_image(i)-elapse_load(:,exptime)));
            vars.load.stitch(i,:) = num2cell(elapse_load(ind,:));
        end
    end
```

Analyzing entire ROI at once

```
    function AnalyzeSurf(src,event)
        check_parpool
        tic

        unicol = vars.unicol; %making global variable available
        filepath = vars.DIC.filepath;
        imagenum = length(filepath);

        dim=1; %which dimension the slopes are calculated with (1=x,2=y)
        dim_col = vars.poscol(dim); %setting column numbers
        x_col = vars.poscol(1);
        y_col = vars.poscol(2);
        u_col = find(cell2mat(cellfun(@(x)
contains(vars.DIC.colheaders,x,'IgnoreCase',true),{'"u"'}, 'UniformOutput', 0)));
        v_col = find(cell2mat(cellfun(@(x)
contains(vars.DIC.colheaders,x,'IgnoreCase',true),{'"v"'}, 'UniformOutput', 0)));
        sig = find(cell2mat(cellfun(@(x)
contains(vars.DIC.colheaders,x,'IgnoreCase',true),{'"Sigma"'}, 'UniformOutput', 0)));

        method = 'Engineering';

        %setting up variables

        F = cell(imagenum,1);
        F{1} = [0,0;0,0];
        exx = zeros(imagenum,1);
        eyy = zeros(imagenum,1);
        exy = zeros(imagenum,1);
        x = [1:imagenum].';
        track = zeros(imagenum,1);

        left_idx = cell(imagenum,1);
        right_idx = cell(imagenum,1);
        left_pts = cell(imagenum,1);
        right_pts = cell(imagenum,1);
        u_fit = cell(imagenum,1);
        v_fit = cell(imagenum,1);
        gof = zeros(imagenum,2);

        WaitMessage = parfor_wait(imagenum, 'Waitbar', true);
        q = parallel.pool.DataQueue;

        %window to plot progress in
        handles.prog_plot = figure('Name','Plot Progress','NumberTitle','off');
        handles.prog_plot.Position = [500,400,850,575];

        handles.p1 = subplot(3,2,[1,3]);
        handles.p2 = subplot(3,2,[2,4]);
        handles.p3 = subplot(3,2,[5,6]);

        plot(x,zeros(imagenum,1),x,zeros(imagenum,1),x,zeros(imagenum,1),'LineWidth',2)
        handles.p3.XAxisLocation = 'origin';
        xlabel('Image Number')
```

```
        ylabel('Calculated Strain')
        legend({'e_x_x','e_y_y','e_x_y'},'Location','EastOutside')
        xlim([1 imagenum])

        afterEach(q,@par_plot);

        parfor j = 2:imagenum

            tempdata = importdata(filepath{j});
            data = tempdata.data;
            tempdata = [];
            j;

            FitData = cell(length(unicol{2}),1);
            cleandata = cell(length(unicol{2}),1);
            for k = 1:length(unicol{2})

                %clean up data and find sheared data
                ind = data(:,vars.poscol(2))==unicol{2}(k);
                a = [];
                [a,~,~,~] = feval(@CleanDIC,data,ind,dim_col,u_col,sig);
                [a,~,~,~] = feval(@CleanDIC,a,true(size(a,1),1),dim_col,v_col,sig);
                temp_pts = findchangepts(a(:,v_col),'Statistic','linear','MaxNumChanges',2); %
use vertical displacement vs x to find location of shear

                if isempty(temp_pts) == 1 || size(temp_pts,1) < 2 % if it doesn't find pts fits
whole range
                    r = [1;length(a(:,dim_col))];
                else %sets individual ranges to fit
                    r = [temp_pts];
                end

                %FitData = [FitData;a(r(1):r(2),:)];
                left_idx{j}(end+1,1) = r(1);
                right_idx{j}(end+1,1) = r(2);
                left_pts{j}(end+1,:) = [a(r(1),:)];
                right_pts{j}(end+1,:) = [a(r(2),:)];

                cleandata{k} = a;
                FitData{k} = [a(r(1):r(2),:)];
            end

            %fixing outlier fit ranges (likely caused by bad tracking in corners)
            out_right = find(isoutlier(right_pts{j}(:,vars.col.x)));
            out_left = find(isoutlier(left_pts{j}(:,vars.col.x)));
            close_left = zeros(1,length(out_left));
            close_right = zeros(1,length(out_right));

            for i_left = 1:length(out_left)
                good_col = setdiff(1:length(left_pts{j}),out_left);
                [~,idx_left] = min(abs(good_col-out_left(i_left)));
                close_left(i_left) = good_col(idx_left);
            end
```

```
            for i_right = 1:length(out_right)
                good_col = setdiff(1:length(right_pts{j}),out_right);
                [~,idx_right] = min(abs(good_col-out_right(i_right)));
                close_right(i_right) = good_col(idx_right);
            end

            left_pts{j}(out_left,:) = left_pts{j}(close_left,:);
            right_pts{j}(out_right,:) = right_pts{j}(close_right,:);
            left_idx{j}(out_left,1) = left_idx{j}(close_left);
            right_idx{j}(out_right,1) = right_idx{j}(close_right);

            %replace fit data with fixed boundaries
            fix_pos = unique(vertcat(out_right,out_left));
            for i_fix = 1:length(fix_pos)
                %FitData{fix_pos(i_fix)} =
cleandata{k}(left_idx{j}(i_fix):right_idx{j}(i_fix),:);
                FitData{fix_pos(i_fix)} = [];
            end

            %fitting/assembling relevant data
            final_FitData = vertcat(FitData{1:end});
            [u_fit{j},u_gof] = fit([final_FitData(:,x_col)
final_FitData(:,y_col)],final_FitData(:,u_col),'poly11');
            u_coeff = coeffvalues(u_fit{j});
            dudx = u_coeff(2);
            dudy = u_coeff(3);
            [v_fit{j},v_gof] = fit([final_FitData(:,x_col)
final_FitData(:,y_col)],final_FitData(:,v_col),'poly11');
            v_coeff = coeffvalues(v_fit{j});
            dvdx = v_coeff(2);
            dvdy = v_coeff(3);
            gof(j,:) = [u_gof.rsquare v_gof.rsquare];
            F{j} = [dudx,dvdx;dudy,dvdy];

            [exx(j),eyy(j),exy(j)] = feval(@calc_strains,dudx,dvdx,dudy,dvdy,method);

            if rem(j,50)==0
                send(q,j)
            end

                %send(q,j)
                WaitMessage.Send;
                pause(0.002);
        end

        function par_plot(j) %updates plots as fit is going

            data_pts = find(~cellfun(@isempty,left_pts));
            if any(data_pts==j)
                ind_plot = j;
            else
                ind_plot = max(data_pts);
            end
```

```
            handles.prog_plot.Name = sprintf('Processed Image %d',ind_plot);

            tempdata = importdata(filepath{ind_plot});
            data = tempdata.data;


            %subplot(3,2,[5,6],ax)
            axes(handles.p3)
                plot(x,exx,x,eyy,x,exy,'LineWidth',2)
                xlabel('Image Number')
                ylabel('Calculated Strain')
                legend({'e_x_x','e_y_y','e_x_y'},'Location','EastOutside')
                axis([1 imagenum -inf inf])
                handles.p3.XAxisLocation = 'origin';

            %subplot(3,2,[1,3],ax)
            axes(handles.p1)
            cla(handles.p1)
                hold on
                scatter3(data(:,x_col),data(:,y_col),data(:,u_col),2,data(:,u_col))
                %left_pts{j}

plot3(left_pts{ind_plot}(:,x_col),left_pts{ind_plot}(:,y_col),left_pts{ind_plot}(:,u_col),'r','Li
neWidth',2)

plot3(right_pts{ind_plot}(:,x_col),right_pts{ind_plot}(:,y_col),right_pts{ind_plot}(:,u_col),'r',
'LineWidth',2);

                surfv = plot(u_fit{ind_plot});
                surfv.EdgeColor = 'none';
                surfv.FaceColor = '#FFA500';
                alpha 0.75;

                xlim([min(data(:,x_col)) max(data(:,x_col))])
                ylim([min(data(:,y_col)) max(data(:,y_col))])
                zlim([min(data(:,u_col)) max(data(:,u_col))])
                view(45,45);
                xlabel('X')
                ylabel('Y')
                zlabel('u')
                title(sprintf('Fit Horz. Displacement dx=%1.3f,
dy=%1.3f',F{ind_plot}(1,1),F{ind_plot}(2,1)))
                hold off

            %subplot(3,2,[2,4],ax)
            axes(handles.p2)
            cla(handles.p2)
                hold on
                %plot3(data(:,1),data(:,2),data(:,v_col),'.')
                scatter3(data(:,x_col),data(:,y_col),data(:,v_col),2,data(:,v_col))

plot3(left_pts{ind_plot}(:,x_col),left_pts{ind_plot}(:,y_col),left_pts{ind_plot}(:,v_col),'r','Li
neWidth',2);
```

```
plot3(right_pts{ind_plot}(:,x_col),right_pts{ind_plot}(:,y_col),right_pts{ind_plot}(:,v_col),'r',
'LineWidth',2);

                surfu = plot(v_fit{ind_plot});
                surfu.EdgeColor = 'none';
                surfu.FaceColor = '#FFA500';
                alpha 0.75;

                xlim([min(data(:,x_col)) max(data(:,x_col))])
                ylim([min(data(:,y_col)) max(data(:,y_col))])
                zlim([min(data(:,v_col)) max(data(:,v_col))])
                view(45,45);
                xlabel('X')
                ylabel('Y')
                zlabel('v')
                title(sprintf('Fit Vert. Displacement dx=%1.3f,
dy=%1.3f',F{ind_plot}(1,2),F{ind_plot}(2,2)))
                hold off
            end

        vars.data.dispgrad = F;
        vars.data.gof = gof;
        vars.data.strain = [exx eyy exy];
        vars.data.strainmethod = {'Surface Fit' method};
        vars.data.leftpts = left_pts;
        vars.data.rightpts = right_pts;
        vars.data.u_fit = u_fit;
        vars.data.v_fit = v_fit;


        WaitMessage.Destroy;
        handles.m_saveexcel.Visible = 'on';
        handles.m_saveproj.Visible = 'on';

        par_plot(imagenum)
        elapse = toc;
        disp(fprintf('Total Time elapsed = %0.0f sec \n Time per image = %0.2f
sec',elapse,(elapse/(imagenum-1))))
    end
```

Analyze row by row

```
    function Analyze(src,event)
        check_parpool
        tic
        %allocate space for data
        images = length(vars.DIC.filepath);
        slopes = cell(images,1); %{du/dx,dv/dx,du/dy,dv/dy}
        rsq = cell(images,1);
        pts = cell(images,1);
        bounds = cell(images,1);
        xrsq = cell(images,1);
        yrsq = cell(images,1);
```

```
    xslopes = cell(images,1);
    yslopes = cell(images,1);

    avg_pts = zeros(images,2);
    avg_bounds = zeros(images,2);
    avg_xslopes = zeros(images,6);
    avg_yslopes = zeros(images,2);
    avg_xrsq = zeros(images,6);
    avg_yrsq = zeros(images,2);

    unicol = vars.unicol; %making global variables available to parfor loop
    filepath = vars.DIC.filepath;

    %calculating and plotting average strains as code runs
    %(initializing)

    strain_plot = figure('Name',append('Calculated Lagrange Strain'),'NumberTitle','off');
    x = [1:images].';
    plot(x,zeros(images,1),x,zeros(images,1),x,zeros(images,1))
    xlabel('Image Number')
    ylabel('Average Strain in Shear Zone')
    legend({'E_x_x','E_y_y','E_x_y'},'Location','NorthWest')
    %ylim([min(data{end}(:,9:11),[],'all') max(data{end}(:,9:11),[],'all')])
    xlim([1 images])

    WaitMessage = parfor_wait(images, 'Waitbar', true);
    q = parallel.pool.DataQueue;
    afterEach(q,@update_strains);

    parfor j = 2:images

        tempdata = importdata(filepath{j});
        colheaders = tempdata.colheaders;
        data = tempdata.data;
        tempdata = [];

%d()/dx
        dim=1; %which dimension the slopes are calculated with (1=x,2=y)
        dim_col = vars.poscol(dim);
        u_col = find(strcmp(vars.DIC.colheaders,{'  "u"'}));
        v_col = find(strcmp(vars.DIC.colheaders,{'  "v"'}));
        sig = find(strcmp(vars.DIC.colheaders,{'  "sigma"'}));
        x_slopes = zeros(length(unicol{2}),6);
        x_rsq = zeros(length(unicol{2}),6);


        avg_pts =zeros(length(unicol{2}),2);

        for k = 1:length(unicol{2})

            ind = data(:,2)==unicol{2}(k);
            a = [];

            [a,~,~,~] = feval(@CleanDIC,data,ind,dim_col,u_col,sig);
```

```
                [a,~,~,~] = feval(@CleanDIC,a,true(size(a,1),1),dim_col,v_col,sig);

                grad_plot = gradient(a(:,v_col))./gradient(a(:,dim_col));
                temp_pts =
findchangepts(grad_plot(:,1),'MinDistance',8,'MaxNumChanges',str2num(handles.infledit.String));

                if isempty(temp_pts) == 1 || size(temp_pts,1) < 2 % if it doesn't find pts fits
whole range
                    r = [1;length(a(:,1))];
                    pts{j}(k,:) = r;
                else %sets individual ranges to fit
                    r = [1;temp_pts;length(a(:,1))];
                    pts{j}(k,:) = temp_pts;
                end

                bounds{j,1}(k,:) = unicol{1}(pts{j}(k,:)); %pixel positions of either the shear
zone bounds

                %applies fits to the x and y displacements on the 3 sections

                for m = 1:2
                    fit_col = [u_col,v_col];
                    imax = length(r)-1;
                    for i = 1:imax %applies fit on ranges
                        [lin_fit,gof,~] =
fit(a(r(i):r(i+1),dim_col),a(r(i):r(i+1),fit_col(m)),'poly1');
                        coeff = coeffvalues(lin_fit);
                        col = i+(m-1)*3;
                        x_slopes(k,col) = coeff(1);
                        x_rsq(k,col) = gof.rsquare;
                    end

                    if length(r) == 2 %if there is only one fit, it applies it to left,center and
right slopes
                        x_slopes(k,m*1:m*3) = coeff(1);
                        x_rsq(k,m*1:m*3) = gof.rsquare;
                    end
                end
            end

        %d()/dy in b/w the mean X positions of shear zone
            dim=2; %which dimension the slopes are calculated with (1=x,2=y)


            avg_pts(j,:) = round(mean(pts{j},1));
            avg_bounds(j,:) = unicol{1}(avg_pts(j,:));
            range = avg_pts(j,1) : avg_pts(j,2);
            y_slopes = zeros(length(range),2);
            y_rsq = zeros(length(range),2);

            for k = range
                ind = data(:,1)==unicol{1}(k);
                a = [];
```

```
            [a,~,~,~] = feval(@CleanDIC,data,ind,dim,u_col,sig);
            [a,~,~,~] = feval(@CleanDIC,a,true(size(a,1),1),dim,v_col,sig);

            for m = 1:2 %applies fit
                [lin_fit,gof,~] = fit(a(:,dim),a(:,fit_col(m)),'poly1');
                coeff = coeffvalues(lin_fit);
                y_slopes(k,m) = coeff(1);
                y_rsq(k,m) = gof.rsquare;
            end
        end


        avg_pts(j,:) = round(mean(pts{j},1));
        avg_bounds(j,:) = unicol{1}(avg_pts(j,:));
        avg_xslopes(j,:) = mean(x_slopes,1);
        avg_yslopes(j,:) = mean(y_slopes,1);
        avg_xrsq(j,:) =  mean(x_rsq,1);
        avg_yrsq(j,:) =  mean(y_rsq,1);

        xrsq{j,1} = x_rsq;
        yrsq{j,1} = y_rsq;
        xslopes{j,1} = x_slopes;
        yslopes{j,1} = y_slopes;


        send(q,j)
        WaitMessage.Send;
        pause(0.002);
    end

    function update_strains(~)
        %saving the data to the global variables
        vars.slopes.raw = cell(images,4);
        vars.slopes.raw{1,1} = zeros(length(unicol{2}),3);
        vars.slopes.raw{1,2} = zeros(length(unicol{2}),3);
        vars.slopes.raw{1,3} = zeros(length(unicol{1}),1);
        vars.slopes.raw{1,4} = zeros(length(unicol{1}),1);

        img = zeros(images,1)==0;
        [vars.data.raw.slopes{img,1}] = xslopes{img,1};  %d/dx
        [vars.data.raw.slopes{img,2}] = yslopes{img,1}; %d/dy
        [vars.data.raw.rsq{img,1}] = xrsq{img,1}; %Rsquared for fits
        [vars.data.raw.rsq{img,2}] = yrsq{img,1};

        %vars.slopes.raw = slopes;

        vars.data.raw.bounds = bounds;

        vars.data.avg.slopes{1} = avg_xslopes;
        vars.data.avg.slopes{2} = avg_yslopes;
        vars.data.avg.rsq{1} = avg_xrsq;
        vars.data.avg.rsq{2} = avg_yrsq;
        vars.data.avg.bounds = avg_bounds;
```

```
            method = 'Lagrange';
            [vars.data.strain(:,1),vars.data.strain(:,2),vars.data.strain(:,3)] =
calc_strains(avg_xslopes(:,2),...
                avg_xslopes(:,5),avg_yslopes(:,1),avg_yslopes(:,2),method);


            clf(strain_plot)
            ax = axes(strain_plot);
            x = [1:size(vars.data.strain,1)].';
            plot(x,vars.data.strain(:,1),x,vars.data.strain(:,2),x,vars.data.strain(:,3))
            xlim([1 length(x)])
            xlabel('Image Number')
            ylabel('Average Strain in Shear Zone')
            legend({'E_x_x','E_y_y','E_x_y'},'Location','NorthWest')

        end

        update_strains
        WaitMessage.Destroy;
        handles.m_saveexcel.Visible = 'on';
        handles.m_saveproj.Visible = 'on';

         a= 1;
         toc
    end
```

Export Data to Excel

```
    function SaveXLS(src,event)
        %Pick where you want to save file
        if isempty(vars.path)==0
            [file,path] = uiputfile({'*.xlsx'},'Save Analyzed Data',vars.path);
        else
            [file,path] = uiputfile({'*.xlsx'},'Save Analyzed Data');
        end

        if path == 0
            return
        end

        vars.path = path;

        filepath = strcat(vars.path,file);

        if isfield(vars,'load')
            A =
cell(size(vars.data.strain,1)+1,size(vars.data.strain,2)+size(vars.load.stitch,2)+1);
            A(1,:) = [{'Image','Exx','Eyy','Exy'},vars.load.colheaders];
            A(2:end,1) = num2cell([1:length(vars.data.strain)].');
            A(2:end,2:end) = [num2cell(vars.data.strain),vars.load.stitch];
        else
            A = cell(size(vars.data.strain,1)+1,size(vars.data.strain,2)+1);
```

```
        A(1,:) = {'Image','Exx','Eyy','Exy'};
        A(2:end,1) = num2cell([1:length(vars.data.strain)].');
        A(2:end,2:end) = num2cell(vars.data.strain);
    end

    delete(filepath)
    writecell(A,filepath,'Sheet',1);%,'WriteMode','replacefile');
    disp('File saved.')
end
```

Save Project

```
function SaveWksp(src,event)
    %Pick where you want to save file
    if isempty(vars.path)==0
        [file,path] = uiputfile('*.mat','Save Analyzed Data',vars.path);
    else
        [file,path] = uiputfile('*.mat','Save Analyzed Data');
    end

    if path == 0
        return
    end

    vars.path = path;

    filepath = strcat(vars.path,file);
    data = vars.data;
    DIC = vars.DIC;
    unicol = vars.unicol;

   if isfield(vars,'load')
       load = vars.load;
       save(filepath,'data','DIC','unicol','load')
   else
       save(filepath,'data','DIC','unicol')
   end

    disp('File saved.')
end
```

Open Workspace

```
function OpenProject(src,event)

    %Select Project file
    if isfield(vars,'path') && isempty(vars.path)==0
        [file,path] = uigetfile('*.mat','Save Analyzed Data',vars.path);
    else
        [file,path] = uigetfile('*.mat','Save Analyzed Data');
    end
```

```
        if path == 0
            return
        end

        filepath = strcat(path,file);
        vars = load(filepath);
        vars.path = path;
        vars.DIC.data = load_DIC(vars.DICfiles,length(vars.DICfiles));
        vars.DIC.filepath = vars.DICfiles;

        vars.unicol{1} = unique(vars.DIC.data(:,1));
        vars.unicol{2} = unique(vars.DIC.data(:,2));

        handles.sldr{1}.Min = 1;
        handles.sldr{1}.Max = length(vars.DICfiles);
        handles.sldr{1}.Value = handles.sldr{1}.Max;
        handles.edit{1}.String = length(vars.DICfiles);
        handles.text{2}.String = sprintf('/%d',length(vars.DICfiles));

        handles.sldr{2}.Min = 1;
        handles.sldr{2}.Max = length(vars.unicol{2});
        handles.sldr{2}.Value = round((handles.sldr{2}.Max-handles.sldr{2}.Min)/2);
        handles.edit{2}.String = vars.unicol{2}(round(handles.sldr{2}.Value));
        handles.text{4}.String = sprintf('/%d',max(vars.unicol{2}));
        handles.colselect.String = vars.DIC.colheaders;

        %handles.bg{1}.Visible = 'off';
        handles.rawDIC_tab.Visible = 'on';
        handles.plotopt_panel.Visible = 'on';
        handles.colselect.Visible = 'on';
        handles.analyze_menu.Visible = 'on';
        handles.m_saveproj.Visible = 'on';
        handles.m_clear.Visible = 'on';
        handles.m_saveexcel.Visible = 'on';
        handles.window.Name = sprintf('DIC Visualizer: %s',file);

        update_plots
    end
```

Clear Variables

```
    function clear_data(src,event)

        handles.rawDIC_tab.Visible = 'off';
        handles.plotopt_panel.Visible = 'off';
        handles.colselect.Visible = 'off';
        handles.analyze_menu.Visible = 'off';
        handles.m_saveproj.Visible = 'off';
        handles.m_clear.Visible = 'off';
        handles.window.Name = 'DIC Visualizer';

        path = vars.path;
        clear vars
```

```
        vars.path = path;
    end
```

Update The plots

```
    function update_plots(src,event)

        imgnum = round(handles.sldr{1}.Value);
        plotstrain = handles.colselect.Value;

        if strcmp(handles.bg{1}.SelectedObject.String,handles.r1{1}.String)
            vars.plot_dim = 2;
        elseif strcmp(handles.bg{1}.SelectedObject.String,handles.r1{2}.String)
            vars.plot_dim = 1;
        end

        %flips 3D strain plots to be positive to be easier to visualize

        sigma = vars.DIC.data(:,strcmp(vars.DIC.colheaders,{'  "sigma"'}));
        z =vars.DIC.data(:,plotstrain);

        %defining 3D mesh data and removing untracked pts
        x = vars.DIC.data(:,vars.poscol(1));
        log_badpts = sigma(:,1)==-1;
        x(log_badpts,:) = [];
        y = vars.DIC.data(:,vars.poscol(2));
        y(log_badpts,:) = [];
        z(log_badpts,:) = [];
        z_u = [];
        z_v = [];

        if isempty(x)
            return
        end

        xlin = linspace(min(x),max(x),length(vars.unicol{1}));
        ylin = linspace(min(y),max(y),length(vars.unicol{2}));
        [X,Y] = meshgrid(xlin,ylin);
        Z = griddata(x(:,1),y(:,1),z(:,1),X,Y,'cubic');

        %check what slice direction to plot
        dir = strcmp(handles.bg{1}.SelectedObject.String,handles.r1{1}.String);

        %points for plotting line on mesh where slice is
        if dir ==1;
            dim = 1;
            dim_col = vars.poscol(dim);
            ind = vars.DIC.data(:,vars.poscol(2))==vars.unicol{2}(round(handles.sldr{2}.Value));
            xl = [min(vars.unicol{1})*0.95 max(vars.unicol{1})*1.05];
            yl = [vars.unicol{2}(round(handles.sldr{2}.Value))
vars.unicol{2}(round(handles.sldr{2}.Value))];
        else
            dim = 2;
```

```
            dim_col = vars.poscol(dim);
            ind = vars.DIC.data(:,vars.poscol(1))==vars.unicol{1}(round(handles.sldr{2}.Value));
            xl = [vars.unicol{1}(round(handles.sldr{2}.Value))
vars.unicol{1}(round(handles.sldr{2}.Value))];
            yl = [min(vars.unicol{2})*0.95 max(vars.unicol{2})*1.05];
        end

        sig = strcmp(vars.DIC.colheaders,{'  "sigma"'});
        [a,left_bound,right_bound,slice_badpts] =
CleanDIC(vars.DIC.data,ind,dim_col,plotstrain,sig);

        strains = {'e_x','e_y','e_x_y','e_1','e_2'};
        position_label = {'X [px]','Y [px]'};
        pos_in = ["X","Y"];

        handles.plot_axes{1} = axes(handles.rawDIC_tab);
        cla(handles.plot_axes{1});
        %axes(handles.plot_axes{1})
        ax1 = subplot(1,2,1);
            cla
            %mesh(X,Y,Z)
            hold on
            scatter3(x,y,z,2,z)
            plot3(xl,yl,[min(Z,[],'all') min(Z,[],'all')],'r')

            if isfield(vars,'data') && isfield(vars.data,'v_fit') && plotstrain == vars.col.v %if
surface fit data exists plot it over data

plot3(vars.data.leftpts{imgnum}(:,vars.col.x),vars.data.leftpts{imgnum}(:,vars.col.y),vars.data.l
eftpts{imgnum}(:,vars.col.v),'r');%,'LineWidth',2

plot3(vars.data.rightpts{imgnum}(:,vars.col.x),vars.data.rightpts{imgnum}(:,vars.col.y),vars.data
.rightpts{imgnum}(:,vars.col.v),'r');%,'LineWidth',2

                surfu = plot(vars.data.v_fit{imgnum});
                surfu.EdgeColor = 'none';
                surfu.FaceColor = '#FFA500';
                alpha 0.75;
                out_right = find(isoutlier(vars.data.rightpts{imgnum}(:,vars.col.x)));
                out_left = find(isoutlier(vars.data.leftpts{imgnum}(:,vars.col.x)));

                close_left = zeros(1,length(out_left));
                close_right = zeros(1,length(out_right));

                for i_left = 1:length(out_left)
                    good_col = setdiff(1:length(vars.data.leftpts{imgnum}),out_left);
                    [~,idx_left] = min(abs(good_col-out_left(i_left)));
                    close_left(i_left) = good_col(idx_left);
                end

                for i_right = 1:length(out_right)
                    good_col = setdiff(1:length(vars.data.rightpts{imgnum}),out_right);
                    [~,idx_right] = min(abs(good_col-out_right(i_right)));
                    close_right(i_right) = good_col(idx_right);
```

```
                end


plot3(vars.data.rightpts{imgnum}(out_right,vars.col.x),vars.data.rightpts{imgnum}(out_right,vars.
col.y),vars.data.rightpts{imgnum}(out_right,vars.col.v),'kx','MarkerSize',6)

plot3(vars.data.leftpts{imgnum}(out_left,vars.col.x),vars.data.leftpts{imgnum}(out_left,vars.col.
y),vars.data.leftpts{imgnum}(out_left,vars.col.v),'kx','MarkerSize',6)
            elseif isfield(vars,'data') && isfield(vars.data,'u_fit') && plotstrain == vars.col.u

plot3(vars.data.leftpts{imgnum}(:,vars.col.x),vars.data.leftpts{imgnum}(:,vars.col.y),vars.data.l
eftpts{imgnum}(:,vars.col.u),'r','LineWidth',2);

plot3(vars.data.rightpts{imgnum}(:,vars.col.x),vars.data.rightpts{imgnum}(:,vars.col.y),vars.data
.rightpts{imgnum}(:,vars.col.u),'r','LineWidth',2);

                surfu = plot(vars.data.u_fit{imgnum});
                surfu.EdgeColor = 'none';
                surfu.FaceColor = '#FFA500';
                alpha 0.75;
            end

            view(17,45);
            colorbar('off')
            xlim([min(x) max(x)])
            ylim([min(y) max(y)])
            zlim([min(z) max(z)])
            xlabel(position_label(1))
            ylabel(position_label(2))
            zlabel(vars.DIC.colheaders(plotstrain))
            k = strfind(vars.DIC.filepath{imgnum},'\');
            m = strfind(vars.DIC.filepath{imgnum},'.');
            title(vars.DIC.filepath{imgnum}(k(end-1):m(end)-1),'Interpreter','none')
            zlim([min(Z,[],'all') max(Z,[],'all')])
            rotate3d on
            axis tight; hold off


        ax2 = subplot(1,2,2);
            cla(ax2)
            hold on
            ylim([-inf inf])

            %yyaxis left
            cla
            %Finding individual linear sections of displacement plots
                if handles.fitcheck.Value == 1

                    grad_plot = gradient(a(:,plotstrain))./gradient(a(:,dim));

                    if str2num(handles.infledit.String) > 0


                        %pts =
```

```
findchangepts(grad_plot(:,1),'MinDistance',8,'MaxNumChanges',str2num(handles.infledit.String));
                        pts =
findchangepts(a(:,plotstrain),'Statistic','linear','MaxNumChanges',str2num(handles.infledit.Strin
g));

                        if isempty(pts) == 1 || size(pts,1) < str2num(handles.infledit.String)
                            r = [1;length(a(:,dim))];
                            pts = [];
                            %width = 0;
                        else
                            r = [1;pts;length(a(:,dim))];
                            %width = vars.unicol{1}(pts(2))-vars.unicol{1}(pts(1));
                        end
                    else
                        pts = [];
                        r = [1 length(a(:,dim))];
                    end

                    ymin = min(a(:,plotstrain));
                    ymax = max(a(:,plotstrain));



plot(a(:,dim_col),a(:,plotstrain),'.',a(slice_badpts,dim_col),a(slice_badpts,plotstrain),'rs')
                    plot(a(pts,dim_col),a(pts,plotstrain),'rx','MarkerSize',12)
                    ylim([ymin-(ymax-ymin)*.1 max(a(:,plotstrain))+(ymax-ymin)*.1])




                    for i = 1:length(pts)+1
                        [lin_fit,gof(i),~] =
fit(a(r(i):r(i+1),dim_col),a(r(i):r(i+1),plotstrain),'poly1');
                        coeff(i,:) = coeffvalues(lin_fit);
                        x_txt = a(r(i),dim_col);
                        y_txt = mean(a(r(i):r(i+1),plotstrain))+(ymax-ymin)*.1;

text(x_txt,y_txt,sprintf('d/d%s=%1.4f',pos_in(dim),coeff(i,1)),'Color','red')
                        plot(lin_fit,'r--')
                    end




                    legend off
                else
                    pts = [];

plot(a(:,dim_col),a(:,plotstrain),'.',a(slice_badpts,dim_col),a(slice_badpts,plotstrain),'rs','Ma
rkerSize',4)
                end

zss = {'U [\mum]','V[\mum]'};
%X dir slice Data
    dim = 1;
```

```
    dim_col = vars.poscol(dim);
    mid_pos = (max(vars.unicol{2})-min(vars.unicol{2}))/2;
    ind_mid = vars.DIC.data(:,vars.poscol(2))==mid_pos;
    data_mid = vars.DIC.data(ind_mid,:);
    xl_mid = data_mid(:,8);
    yl_mid = data_mid(:,9);

    ind_top = vars.DIC.data(:,vars.poscol(2))==vars.unicol{2}(1);
    data_top = vars.DIC.data(ind_top,:);
    xl_top = data_top(:,8);
    yl_top = data_top(:,9);

    ind_bot = vars.DIC.data(:,vars.poscol(2))==vars.unicol{2}(1);
    data_bot = vars.DIC.data(ind_bot,:);
    xl_bot = data_bot(:,8);
    yl_bot = data_bot(:,9);

%Y dir slice Data
    dim = 2;
    dim_col = vars.poscol(dim);
    yslc_pos = (max(vars.unicol{1})-min(vars.unicol{1}))/2;
    ind = vars.DIC.data(:,vars.poscol(1))==yslc_pos;
    data_yslc = vars.DIC.data(ind,:);
    xl = data_yslc(:,8);
    yl = data_yslc(:,9);
    ax = [];
    ylabel(vars.DIC.colheaders(plotstrain))
    xlabel(position_label(dim))
    hold off
    end
```

Other Functions

```
    function check_parpool
        poolobj = gcp('nocreate');
        if isempty(poolobj)
            parpool;
        end
    end
```

GUI Callbacks etc

```
    function strain_btn(src,event) %update when data column changed
        update_plots
    end

    function pos_btn(src,event) %update when plot direction changed to y
        if strcmp(handles.bg{1}.SelectedObject.String,handles.r1{1}.String)
            vars.plot_dim = 2;
        elseif strcmp(handles.bg{1}.SelectedObject.String,handles.r1{2}.String)
            vars.plot_dim = 1;
        end
```

```
        handles.sldr{2}.Max = length(vars.unicol{vars.plot_dim});
        handles.edit{2}.String = int2str(round((max(vars.unicol{vars.plot_dim})-
min(vars.unicol{vars.plot_dim}))/2));


        [~,ind] = min(abs(vars.unicol{vars.plot_dim}-str2num(handles.edit{2}.String)));
        handles.sldr{2}.Value = ind;

        range = handles.sldr{2}.Max-handles.sldr{2}.Min;
        handles.sldr{2}.SliderStep = [1/range 10/range];
        handles.text{4}.String = sprintf('/%d',max(vars.unicol{vars.plot_dim}));


        update_plots
    end

    function ImgEdit(src,event) %Enter Image number to update slider/plots


        string_contains_numeric = @(S) ~isnan(str2double(S));

        if string_contains_numeric(handles.edit{1}.String) == 0
            disp('Only enter numbers')
        elseif str2num(handles.edit{1}.String) > handles.sldr{1}.Max
            disp('Input is higher than number of images')
        elseif str2num(handles.edit{1}.String) < 1
            disp('Please enter a positive integer')
        else
            vars.DIC.data = load_DIC(vars.DIC.filepath,str2num(handles.edit{1}.String));
            handles.sldr{1}.Value = str2num(handles.edit{1}.String);
            update_plots
        end
    end

    function ImgSlide(src,event) %Image slider updates edit field/plots
        vars.DIC.data = load_DIC(vars.DIC.filepath,int32(handles.sldr{1}.Value));
        handles.edit{1}.String = int2str(handles.sldr{1}.Value);
        update_plots
    end

    function PosEdit(src,event) %Enter Position value and update slider
        string_contains_numeric = @(S) ~isnan(str2double(S));



        if string_contains_numeric(handles.edit{2}.String) == 0
            disp('Only enter numbers')
            handles.edit{2}.String =
int2str(vars.unicol{vars.plot_dim}(round(handles.sldr{2}.Value)));
        else
            [~,ind] = min(abs(vars.unicol{vars.plot_dim}-str2num(handles.edit{2}.String)));
            handles.sldr{2}.Value = ind;
            handles.edit{2}.String =
int2str(vars.unicol{vars.plot_dim}(round(handles.sldr{2}.Value)));
```

```
        update_plots
    end

    uicontrol(handles.edit{2})
end

function PosSlide(src,event) %Position Slider updates edit field
    ind = round(handles.sldr{2}.Value);
    handles.edit{2}.String = int2str(vars.unicol{vars.plot_dim}(ind));
    update_plots
end

function FitCheck(src,event)
    if handles.fitcheck.Value == 1
        set(handles.infledit,'Enable','on')
        update_plots
    else
        set(handles.infledit,'Enable','off')
        update_plots
    end
end

function InflEdit(src,event)
    string_contains_numeric = @(S) ~isnan(str2double(S));
    if string_contains_numeric(handles.infledit.String) == 0
        disp('Only enter numbers')
        handles.infledit.String = '0';
    else
        int = [0,1,2,3,4,5];
        [~,new] = min(abs(int-str2num(handles.infledit.String)));
        handles.infledit.String = int2str(int(new));
        update_plots
    end

end

function [choice,idx] = choosedialog(message,options)

    d = dialog('Position',[300 300 250 150],'Name','Select One');
    txt = uicontrol('Parent',d,...
           'Style','text',...
           'Position',[20 80 210 40],...
           'String',message);

    popup = uicontrol('Parent',d,...
           'Style','popup',...
           'Position',[75 70 100 25],...
           'String',options,...
           'Callback',@popup_callback);

    btn = uicontrol('Parent',d,...
           'Position',[89 20 70 25],...
           'String','Close',...
           'Callback','delete(gcf)');
```

```
        choice = options(1);
        idx = 1;

        % Wait for d to close before running to completion
        uiwait(d);
           function popup_callback(popup,event)
              idx = popup.Value;
              popup_items = popup.String;
              choice = char(popup_items(idx,:));
           end
    end

    function resize_fcn(src,event)
        files_panel_pos = handles.window.Position;
        main_pos = handles.window.Position;
        plot_panel_pos = [main_pos(3)-handles.panel_w,main_pos(4)-handles.file_h-handles.plot_h-
10,handles.panel_w,handles.plot_h];
        file_panel_pos = [plot_panel_pos(1),main_pos(4)-handles.file_h-
5,handles.panel_w,handles.file_h];
        handles.plotopt_panel.Position = plot_panel_pos;
        handles.files_panel.Position =file_panel_pos;
        handles.tabgp.Position = [5 4 main_pos(3)-handles.panel_w-2 main_pos(4)];
    end

end
```

Unested functions so they can be used with parfor

```
    function [exx,eyy,exy] = calc_strains(dudx,dvdx,dudy,dvdy,method) %input d()/dx must already
be in correct coordinate system

        if strcmp(method,'Lagrange')
            exx = dudx+(dudx.^2+dvdx.^2)./2;
            eyy = dvdy+(dudy.^2+dvdy.^2)./2;
            exy = (dudy+dvdx+dudx.*dudy+dvdx.*dvdy)./2;
        elseif strcmp(method,'Euler')
            exx = dudx-(dudx.^2+dvdx.^2)./2;
            eyy = dvdy-(dudy.^2+dvdy.^2)./2;
            exy = (dudy+dvdx-dudx.*dudy-dvdx.*dvdy)./2;
        elseif any(strcmp(method,{'True','Engineering'}))
            exx = dudx;
            eyy = dvdy;
            exy = (dudy+dvdx)./2;
        end

    end


    function [a,left_bound,right_bound,slice_badpts] = CleanDIC(data,ind,dim,column,sig)

        %find intracked pts
        sigma = data(:,sig);
```

```
        log_badpts = sigma(:,1)==-1;

        a = [];
        a = data(ind,:);
        pos = 3;
        %a(:,pos) = data(ind,column);
        b = data(ind,:);

        %finding indices of bad pts and places where multiple pts are next
        %to each other
        slice_badpts = log_badpts(ind);
        ind_badpts = find(slice_badpts==1);
        slice_goodpts = ~slice_badpts;
        log_dif = diff(slice_badpts);
        ind_dif = find(log_dif==0);
        ind_dif(slice_badpts(ind_dif)==0) =[];


        %find bounds of bad pts to interpolate
        left_bound = [];
        right_bound = [];
        i = length(ind_dif);
        while i > 0
            if ind_dif(i) == 1 && isempty(find(ind_dif==ind_dif(i)+1)) %its the first index and
is end of pair
                left_bound(end+1,1) = [ind_dif(i)]; %first is left
                right_bound(end+1,1) = [ind_dif(i)+1]; %next is right
            elseif ind_dif(i) == 1 %iits the first index
                left_bound(end+1,1) = [ind_dif(i)]; %first of pair
            elseif isempty(find(ind_dif==ind_dif(i)-1)) && isempty(find(ind_dif==ind_dif(i)+1))
%preceding & following index isnt there (pair of bad pts)
                left_bound(end+1,1) = [ind_dif(i)]; %make first of pair
                right_bound(end+1,1) = [ind_dif(i)+1];
            elseif isempty(find(ind_dif==ind_dif(i)-1)) %preceding index isnt there
                left_bound(end+1,1) = [ind_dif(i)]; %make first of pair
            elseif isempty(find(ind_dif==ind_dif(i)+1)) %following index isnt there
                right_bound(end+1,1) = [ind_dif(i)+1]; %make last of pair
            end
            i = i-1;
        end

        if length(left_bound)~=length(right_bound)
            disp('Uneven number of bounds for untracked points')
        end

        %any lone bad pts that were missed are assigned bounds of its index
        unbounded = setdiff(ind_badpts,[ind_dif;ind_dif+1]);
        i = length(unbounded);
        while i > 0
            left_bound(end+1,1) = [unbounded(i)];
            right_bound(end+1,1) = [unbounded(i)];
            i = i-1;
        end
```

```
        left_bound = sort(left_bound);
        right_bound = sort(right_bound);

        %Interpolation between the bounds
        i = length(left_bound);
        while i > 0

            if left_bound(i) == 1 && right_bound(i)+1 <= length(a(:,column)) %has no pt to the
left
                a(left_bound(i):right_bound(i),column) = a(right_bound(i)+1,column);
            elseif right_bound(i) == length(a) && left_bound(i)-1 >= 1%has no point to the right
                a(left_bound(i):right_bound(i),column) = a(left_bound(i)-1,column);
            elseif left_bound(i) == 1 && right_bound(i) == length(a)%all points are bad

            else
                m = (a(right_bound(i)+1,column)-a(left_bound(i)-
1,column))/(a(right_bound(i)+1,dim)-a(left_bound(i)-1,dim));
                inter_fun = @(X) m*(X-a(left_bound(i)-1,dim))+a(left_bound(i)-1,column);
                a(left_bound(i):right_bound(i),column) =
inter_fun(a([left_bound(i):right_bound(i)],dim));
            end

            i=i-1;
        end
    end
```

Published with MATLAB® R2019a

Vita

Matthew O. Vaughn was born in Winston-Salem, North Carolina on February 15th, 1994, to parents David Vaughn and Anne Vaughn-Alvarez. Matthew graduated from Mesquite High School in Gilbert, Arizona in May 2012 before going on to study Mechanical Engineering at Arizona State University in Tempe, Arizona. He earned a Bachelor of Science in Engineering degree in Mechanical Engineering with a minor in Materials Science and Engineering in May 2016. Afterwards he joined the Mechanical Engineering department at Johns Hopkins University in August 2016 for his doctoral studies under the advisement of Professor Kevin Hemker. In May 2018, Matthew earned his Master of Science in Engineering in Mechanical Engineering while continuing on to fulfill the requirements for a Doctor of Philosophy in Mechanical Engineering in September of 2021.